الجمهورية الجزائرية الديمقراطية الشعبية
The People's Democratic Republic of Algeria
وزارة التعليم العالي و البحث العلمي
Ministry of Higher Education and Scientific Research
جامعة الشهيد حمة لخضر –الوادي
University of Echahid Hamma Lakhdar –EL OUED

Faculty of Exact Sciences — **كلية العلوم الدقيقة**

Department of Physics — **قسم الفيزياء**

Ref : …… — **المرجع: ……**

Thesis presented for the purpose of obtaining the degree of Doctorate

Specialty: Rayanemment and material

SUBJECT OF THE THESIS:

Elaboration and optimization of Iron Oxide thin films deposited via spray pyrolysis. Applications in water treatment

Presented by :

Dhaouia BEKKAR

The Member of Jury :

Mr : Azzeddine BEGGAS	**MCA**	**University of El-Oued**	**President**
Mr : Boubaker BEN HAOUA	**Professor**	**University of El-Oued**	**Reporter**
Mr : Said MEHELLOU	**MCA**	**University of El-Oued**	**Examiner**
Mr : Okba BELAHSSEN	**Professor**	**University of Biskra**	**Examiner**
Mr : Med Lotfi BENKHIDER	**Professor**	**University of Tebessa**	**Examiner**
Mr : Abdelouahed CHALA	**Professor**	**University of Biskra**	**Examiner**

23/02/2021

ACKNOWLEDGEMENT

At first I am grateful to
Allah
To blessing me much more than I deserve.

secondly, I would like to express my sincere gratitude to my advisor Prof. Boubaker BEN HAOUA for the continuous support of my Ph.D study and related research, for his patience, motivation, and immense knowledge. His guidance helped me in all the time of research and writing of this thesis. I could not have imagined having a better advisor and mentor for my Ph.D study.

Besides my advisor, I would like to thank the rest of my thesis committee: Prof. _____, Prof. _____, and Dr. _____, for their insightful comments and encouragement, but also for the hard question which stimulated me to widen my research from various perspectives.

My sincere thanks also goes to Dr. Othman BEN HAOUA, Dr. Achour RAHAL, and Dr. Yousef MEFTAH, who provided me an opportunity to join their team as intern, and who gave access to the laboratory and research facilities. Without they precious support it would not be possible to conduct this research.

Last but not the least, I would like to thank my whole family:
my parents,
my husband,
BEKKAR Family,
DJEBLOUN Family,
for supporting me spiritually throughout writing this thesis.

Bekkar Dhaouia

TABLE OF CONTENTS

LIST OF FIGURES

LIST OF TABLES

ABBREVIATIONS

T_C	Curie temperature
T_m	Melting temperature
Ferro	Ferromagnetism
Para	Paramagnetism
IONPs	Iron oxide nanoparticles
T_M	Morin temperature
T_N	Néel temperature
CB	Conduction Band
SPMN	Spray pyrolysis with moving nozzle
VB	Valence Band
NUV	Near Ultraviolet
VIS	Visible
NIR	Near Infrared
PVD	Physical vapor deposition
PLD	Pulsed laser deposition
CVD	Chemical vapor deposition
CBD	Chemical Bath Deposition
XRD	X-Ray Diffraction
JCPDS	Joint Committee Power Diffraction Standards
FTIR	Fourier Transform Infra-Red
SEM	Scanning Electron Microscope
RT	Room temperature
FWHM	Full width at half-maximum

GENERAL INTRODUCTION

I.Introduction

Iron is the fourth most abundant element in the crust of earth [1]. It exhibits as Fe (II) and Fe (III) in a variety of minerals including different types of iron oxides. The iron oxides are in fact oxides, hydroxides or oxihydroxides. All iron oxides and hydroxides are consisting of iron atom (Fe), oxygen atom (O) and hydrogen atom H or hydroxide OH group. They differ in coordination, in the valence of iron atom and, moreover, in the structure of crystal [2-3]. The more important ones are: Goethite (α-FeOOH), Ferrihydrite ($Fe_5HO_8.4H_2O$), Akaganeite (β-FeOOH), Hematite (α-Fe_2O_3) Lepidocrocite (γ-FeOOH), Maghemite (γ-Fe_2O_3), Feroxyhyte (δ'-FeOOH), Magnetite (Fe_3O_4); most of these compounds are thermodynamically stable in natural systems (e.g. goethite, hematite, and magnetite) while others can be designated as intermediates only such as (ferrihydrite, maghemite) [1, 4-6].

The iron oxides have been developed in the form of nanopowders and thin films in order to employ them in wide variety areas of science and technology applications including medical use[7-9], environmental chemistry study[10-12], and soil treatment[13-15]. Also , industrial uses as pigment[16] and coating[17, 18]are taking part in those applications. Iron oxides nanomaterials synthesizing can be made through several methods, which can be generally classified as physical, chemical and biological manner[12]. To avoid the problems linked to the physical methods which suffered from the inability to control the size of particles in the nanometer range, spray pyrolysis is one of the efficient chemical methods utilized for such purpose, yet classical spray needs more than 1hour to elaborate one sample having as dimensions (7.5x2.5x0.13cm^3); In attempt to avoid this, spray with moving nozzle (SPMN) is used to avoid not only the spent time but also the heat drop of substrate during all the time of the samples elaboration. In order to improve themagnetic properties of hematite, various dopants have been used such as Ti[19], Al [20], Co [21], Cr [22]… etc. Among these dopants, cobalt with electronic configuration of [Ar] $3d^74s^2$ having one electron more than iron, has gained much attention. Cobalt atom gives one d and two s electrons to oxygen and keeps six electrons on its own atom. When Co is substituted for Fe with spin down electron, the spin down d band gets totally filled with one remaining spin up d-electron, This results in increasing in net magnetization in cobalt doped iron oxide [23].

There are some reliable reports in the literature that show encouraging results about the activity of different drugs and antimicrobialformulation in the form of NPs [24-26]. The biological activity of specific materials differs when the size of the constituting particles

reduces to nanoscale dimension. An effective way to estimate the efficiency of NPs is to monitor the response bacteria exposed to these particles. Some antimicrobial gadgets arereally toxic; thus why there is a big interest in finding ways to create new types of safe biocidal materials. Recently it has been confirmed that extremely reactive metal oxide nanoparticles show excellent evidence biocidal action against Gram-positive and Gram-negative bacteria [27].

Wastewater discharged by some industries under uncontrolled and unsuitable conditions is leading to significant environmental concern. Dyes are one of the major constituents in wastewater. Industrial dyes are stable, toxic and also consideredpotentially carcinogenic. Their release into the environment can lead to serious environmental and health problems. Hence,it is important to treat dye wastewater before it gets discharged in outer environment [28], That is why the main goal of this thesis will be to use iron oxide nanoparticles to treat the wast water via photocatalytic test.

II . Organization of the Thesis

The layout of the four chapters is as follows:

Chapter 1: This chapter providesa bibliographic study on iron oxide nanoparticles. It is divided into tow parts.

- The first concerns the properties of iron oxides. We will present bibliographical elements concerning structural, magnetic, electrical and optical properties of these oxides which make them interesting for different fields of application.
- The second part of the chapter presents the specific properties of nanoparticles and the application fields of iron oxide nanoparticles.

Chapter 2: This chapter contains the experimental details of the deposition of hematite thin films, includes a description of the deposition procedures, the techniques used to characterize hematite thin films.

Chapter 3: This chapter introduces a broad discussion of the experimental results obtained by deposition of 0-1.5wt % Cobalt doped hematite iron oxide (α-Fe_2O_3) thin films via spray pyrolysis method with moving nozzle.As an application in the areas of water treatment, The photocatalytic activitiesof the samples will be studied.

Chapter 4: In this chapter a study of growth of 0-20 wt % Cobalt doped hematite iron oxide (α-Fe_2O_3) thin films by spray pyrolysis is presented. The crystallographic and Optical

properties will be examined. An antibacterial assay will be discussed by disk diffusion assay using: both Gram-negative andpositive bacteria.

Finally, the thesis will be ended with a general conclusion and abstruct.

References

[1] J.L. Jambor, J.E. Dutrizac, Chem. Revi. 98 (1998): 2549.

[2] Y. Meftah, D. Bekker, B. Benhaoua, A. Rahal, A. Benhaoua, A. Hamzaoui, Digest. J.Biomater.Nano. 13(2018): 465.

[3] R.M. Cornell, U. Schwertmann, John Wiley & Sons, (2003).

[4] R. Cornel, U. Shwertmann, VCH Editions, Weinhein, Germany, (1991).

[5] V. Uwamariya, IHE Delft Institute for Water Education, (2013).

[6] H. Wigger, Springer, (2017).

[7] R.V. Kumar, Y. Diamant, A. Gedanken, Chem. of. Mater. 12 (2000): 2301.

[8] R. Schrebler, K. Bello, F. Vera, P. Cury, E. Muñoz, R. del Río, H.G. Meier, R. Córdova, E.A. Dalchiele, Electrochem. and. Solid. State Lett. 9 (2006): C110.

[9] G. Binitha, M. Soumya, A.A. Madhavan, P. Praveen, A. Balakrishnan, K. Subramanian, M. Reddy, S.V. Nair, A.S. Nair, N. Sivakumar, J. of. Mater. Chem. A. 1 (2013): 11698.

[10] K. Woo, J. Hong, S. Choi, H.-W. Lee, J.-P. Ahn, C.S. Kim, S.W. Lee, Chem. of. Mater. 16 (2004): 2814.

[11] A. Al-Hobaib, K.M. AL-Sheetan, L. El Mir, Mater. Sci. in. Semicond. Proces. 42 (2016):107.

[12] A. Ali, M.Z. Hira Zafar, I. ulHaq, A.R. Phull, J.S. Ali, A. Hussain, Nanotech. Sci. and. App. 9 (2016): 49.

[13] D. Yokoyama, K. Namiki, H. Fukasawa, J. Miyazaki, K. Nomura, Y. Yamada, J. of. Radioan.l and. Nucl. Chem. 272 (2007): 631.

[14] S. Laurent, D. Forge, M. Port, A. Roch, C. Robic, L. Vander Elst, R.N. Muller, Chem. Revi. 108 (2008): 2064.

[15] A.M. Jubb, H.C. Allen, ACS App. Mater. &. Interfa. 2 (2010): 2804.

[16] G. Zelmanov, R. Semiat, Water Resear. 42 (2008): 492.

[17] R. Todorovska, S. Groudeva-Zotova, D. Todorovsky, Mater. Lett. 56 (2002): 770.

[18] S. Kulkarni, C. Lokhande, Mater. Chem. and. phys. 82 (2003):151.

[19] X. Wang, K. Maeda, A. Thomas, K. Takanabe, G. Xin, J.M. Carlsson, K. Domen, M. Antonietti, Nature Mater. 8 (2009): 76.

[20] D.B. Shinde, J. Debgupta, A. Kushwaha, M. Aslam, V.K. Pillai, J. of. The. Americ. Chem. Soci. 133 (2011): 4168.

[21] M. Pelaez, N.T. Nolan, S.C. Pillai, M.K. Seery, P. Falaras, A.G. Kontos, P.S. Dunlop, J.W. Hamilton, J.A. Byrne, K. O'shea, App. Catalys. B: Environ. 125 (2012): 331.

[22] E. Yilmaz, C. Yogi, K. Yamanaka, T. Ohta, H.R. Byon, Nano. Lett, 13 (2013): 4679.

[23] A. Akbar, S. Riaz, R. Ashraf, S. Naseem, IEEE Transac. onMagn. 50 (2014): 1.

[24] F. Forestier, P. Gerrier, C. Chaumanrd, A.-M. Quero, P. Couvreur, C. Labarre, Journal of Antimicrobial Chemotherapy, 30 (1992) 173-179.

[25] M. Fresta, G. Puglisi, G. Giammona, G. Cavallaro, N. Micali, P.M. Furneri, J. of. Pharm. Sci. 84 (1995): 895.

[26] V.P. Shah, K.K. Midha, J.W. Findlay, H.M. Hill, J.D. Hulse, I.J. McGilveray, G. McKay, K.J. Miller, R.N. Patnaik, M.L. Powell, Pharm. Resear. 17 (2000): 1551.

[27] P.K. Stoimenov, R.L. Klinger, G.L. Marchin, K.J. Klabunde, Langmuir, 18 (2002): 6679.

[28] Bhosale, Sanjana S., et al. Journal of MaterialsScience:Materials in Electronics 30.5 (2019): 4590-4598.

CHAPTER I :

BIBLIOGRAPHIC STUDY

This chapter presents a bibliographic study on iron oxide nanoparticles. It is divided into two parts.

The first one concerns the properties of iron oxides. In which bibliographical elements concerning structural, magnetic, electrical and optical properties of these oxides will be presented, which make such oxides interesting for different fields of application. The second part of the chapter presents the specific properties of nanoparticles and the application fields of iron oxide nanoparticles.

I. 1. Iron oxides

I. 1. 1. General Information on iron oxides

Iron oxides are widespread in the environment and widely used by human race in a variety of applications (Fig. I. 1). Both this everywhere presence in nature and utilization as tools has been known for centuries and are still legal today. Iron oxides are present in all sort of liquid, solid, and gaseous environments. Depending on the type of use, several sources of iron oxides exist. Applications range from steel production to medicine and fine art [1].

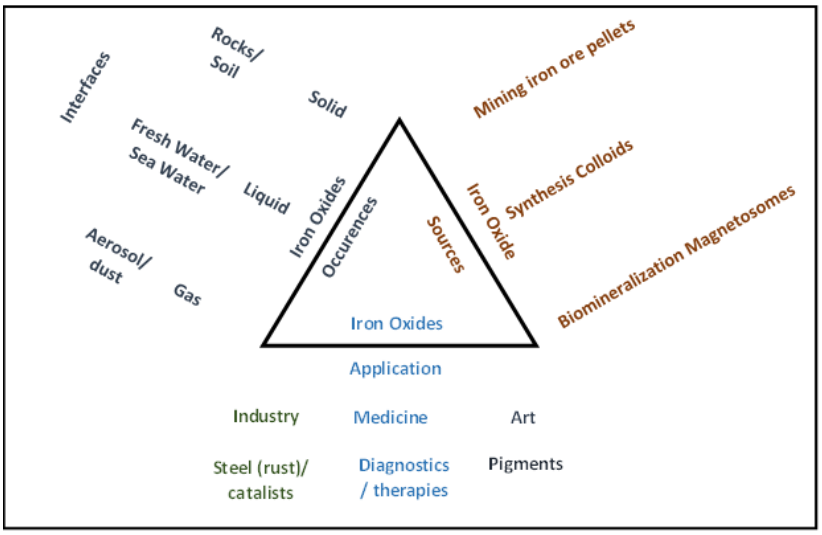

Fig. I. 1 Scheme of the iron oxide occurrences, sources, and applications [1].

There are sixteen iron oxides and hydroxides known to date. The more important ones are listed in Table I. 1. All those specimens consist of Fe, O and/or OH. They differ in composition, in Fe valence and in crystal structure.

Table I. 1 Different known iron oxides [1].

Type ofIron compouns	Ironoxides	Ironoxyhydroxides	Ironhydroxides
Fe(II) compounds	Wüstite: FeO		Whiterust: $Fe(OH)_2$
Fe(II)-Fe(III) compounds	Magnetite: Fe_3O_4	Green rusts– Fougèrite: $[Fe^{2+}_4Fe^{3+}_2(OH)_{12}][CO_3]\cdot 3H_2O$	
Fe(III) compounds	Hematite: α-Fe_2O_3 Maghemite: γ-Fe_2O_3 β-Fe_2O_3 δ-Fe_2O_3 ε-Fe_2O_3	Goethite: α-FeOOH Akaganéite: β-FeOOH Lepidocrocite γ-FeOOH Feroxyhyte: δ-FeOOH Ferrihydrite: $5Fe_2O_3\cdot 9H_2O$ Schwertmannite; $Fe_8O_8(OH)_6(SO_4)\cdot nH_2O$	Bernalite: $Fe(OH)_3$

The first iron oxide discovered in the soil is hematite, which is very stable thermodynamically under atmospheric conditions and considered as final form of many transformations of other iron oxides types. Many different processes can also synthesize hematite; the most used ones are:

- The thermal decomposition of an iron hydroxide (FeOOH) or an iron salt at a temperature between 500 and 600°C,
- Forced hydrolysis of a solution of an iron salt III such as Fe $(NO_3)_3$, Fe $(ClO_4)_3$, or $FeCl_3$ in an acidic medium (pH 1-2) or at a temperature above 100 ° C.

Magnetite is also present in the soil. It is not thermodynamically stable under atmosphere conditions; it has the most important magnetism among iron oxides. It can be synthesized by:

- Partial oxidation of a solution of iron II with a solution of potassium nitrate (KNO_3) in an alkaline medium at 90°C.
- Precipitation of two solutions of iron salt II and III with an iron/iron III ratio of 0.5 or 10 [2].

Maghémite is also in attendance in the top soil. Yet, it is metastable. It can be elaborated by:

- An annealing treatment of lepidocrocite (γ-FeOOH) or magnetite in a heater at 250°C for two hours,

- Oxidation of 2 iron chloride solutions ($FeCl_3$ and $FeCl_2$) under a flow of air at a temperature of 20°C.

The phase transformation between the three iron oxides (hematite, magnetite and maghemite) is possible under certain conditions:

- Magnetite can be oxidized to maghemite, in air at 200 to 500°C depending on the reaction:

$$2Fe_3O_4 + ½\ O_2 \rightarrow 3\gamma\text{-}Fe_2O_3 \qquad \text{(I-1)}$$

- Maghemiteis transformed into hematite by heating in air at 370-600°C. This transformation temperature depends on the method of synthesis of maghemite and the impurities presence, the hematite can be converted into magnetite at 350-600°C under a reducing atmosphere (H_2, CO, organic compound) depending on the reaction [3]:

$$3\alpha\text{-}Fe_2O_3 + H_2 \rightarrow 2Fe_3O_4 + H_2O \qquad \text{(I-2)}$$

I. 1. 2 Physicochemical properties

The physico-chemical properties of the three iron oxides (hematite, magnetite and maghemite) in the massive state are summarized in Table I. 2.

Table I. 2: Physico-chemical properties of the most frequent iron oxides [4].

Iron oxide	Color	molaire Masse (g.mol-1)	Temperature Of fusion (°C)	volumic Masse (kg.m-3)
Hematite	red to Brown	160	1350	5260
Magnetite	black	232	1583-1597	5180
Maghemite	brown	160	-	4870

I. 1. 3 Structural properties

The crystalline structure of hematite, for its part, is of the rhombohedral type. This structure consists of oxygen ions occupying a hexagonal arrangement (ABAB) with Fe^{3+} ions occupying octahedral sites (Fig. I. 2 a). The lattice parameters *a* and *c* of the hematite are (a = 5.034 Å and c = 13.75 Å). Magnetite and maghemite have a spinel structure. The structure of magnetite is composed of a cubic compact assembly with centered faces (ABC) of O^{2-} ions

delimiting octahedral and tetrahedral crystallographic sites in which the various cations necessary for the neutrality of the mesh take place (Fig. I. 2b). Fe^{3+} ions are distributed haphazardly between the tetrahedral and octahedral sites and Fe^{2+} ions reside in only the octahedral sites. Maghemite has a spinel structure similar to that of magnetite but differs in the presence of scattered vacancies in the cationic sub-lattice of octahedral sites (Fig. I. 2c). Lattice parameters *a* of the magnetite and maghemite are (*a* = 8.396Å) and *a* = 8.347Å, repctively [4].

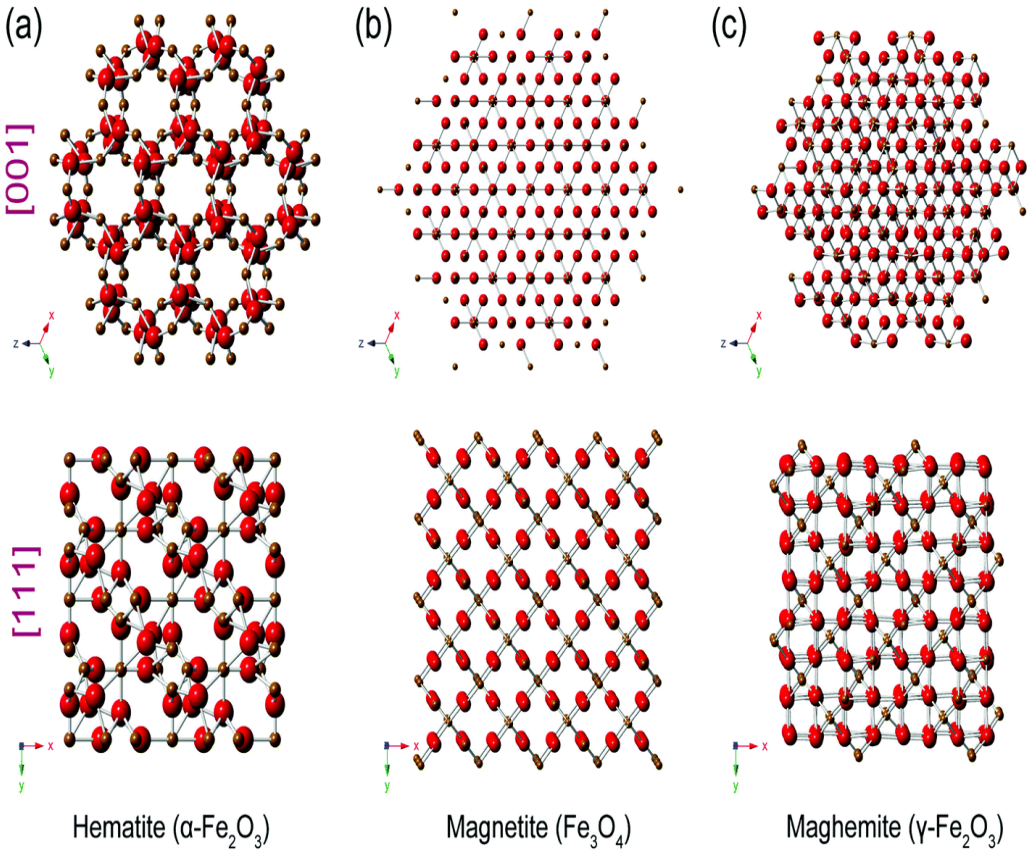

(c)

Fig. I. 2: Crystalline structures of magnetite (a), maghemite (b) and hematite (c) [5].

I. 1. 4 Magnetic properties

I. 1. 4. 1 General Magnetism

Magnetism is a physical phenomenon in which attractive or repulsive forces occur between two materials. On the scale of the atom, magnetism results from the movement of electrons. Indeed, electric charge movement is a source of magnetic field and it can be related with a magnetic moment [6].

Two sources are the origin of the magnetic moment:

- The movement of electrons around the nucleus called the orbital moment,
- The intrinsic motion of the electron around itself called the moment of spin.

An external magnetic field application has the effect of orienting the magnetic moments in a given direction. in respect to the arrangement of these moments, in both absence and presence of a magnetic field, magnetic materials are differed in five categories according to their magnetism type:

- Diamagnetism, which characterizes materials that contain only non-magnetic atoms. The origin of this phenomenon comes from a deformation of the orbital motion of the electrons. As applying an outer magnetic field, the material acquires a permanent moment of direction opposite to the field one. Copper, mercury, lead, silver and gold are diamagnetic materials.
- Paramagnetism, which characterizes materials with permanent magnetic moments. A paramagnetic material exhibits magnetization only in the presence of an outer magnetic field. The magnetic moments are aligned with the direction of the field. On the other hand, in the absence of the field, the orientation of these moments is distributed randomly in the material. The latter compensate each other in such a way that the global magnetization vanishes. Aluminum, platinum and manganese are paramagnetic materials.
- Ferromagnetism, which characterizes materials whose magnetic moments of neighboring atoms are arranged in parallel. The materials then exhibit spontaneous magnetization due to this alignment. Ferromagnetic materials have the ability to magnetize very strongly under the effect of an outer magnetic field and can keep the magnetization even in its absence. At a temperature of 0 K, the ferromagnetic material has a spontaneous magnetization called saturation magnetization. This magnetic behavior disappears above a critical temperature (Curie temperature). Thus, the magnetic moments are disordered and the paramagnetic behavior predominates. Iron, cobalt and nickel are ferromagnetic materials.
- Antiferromagnetism, which characterizes materials whose magnetic moments are arranged antiparallel. These magnetic moments are divided into two equal and opposite sub-lattice, so that in non-presence of a magnetic field the total magnetization is zero. The anti Ferro magnetism disappears above a critical temperature (Néel temperature). Above this temperature the paramagnetic behavior predominates. The oxides of

manganese and nickel, lepidocrocite (γ-FeOOH) and akaganeite (β-FeOOH), goethite (α-FeOOH)are antiferromagnetic materials.

- Ferrimagnetism, which characterizes materials whose magnetic moments of two sub-lattice have different amplitudes on the one hand and are opposite on the other. A ferrimagnetic material then has a spontaneous magnetization, as in ferromagnetic materials, due to incomplete compensation of magnetic moments. The ferrimagnetic behavior disappears above the Curie temperature. Ferrites have a ferrimagnetic behavior [7].

I. 1. 4. 2 Magnetism of iron oxides

The exclusive physical properties of magnetic nanoparticles (NPs) have originated lots of studies for the attentive understanding of issues. Magnetic NPs are practical in many applications in data storage field, catalysis, or biomedicine. In biomedicine field, iron oxide nanoparticles are favoured because of their higher biocompatibility in comparison with other magnetic materials. A key matter for iron oxide nanoparticles employing in biomedical utilisation is to be mono crystalline and monodisperse. Definitely, magnetic properties at the nanoscale depend on the particle size, so that size polydispersity steadily limits the nonmaterial act. Though, iron oxide NPs grain boundaries are known to induce magnetic aggravation, which interpreted into degradation of their saturation in magnetic behaviour. Magnetite is the magnetic mineral responsible for the strongest magnetizations. It is ferrimagnetic at 300K and has a Curie temperature of 850K. The maghemite has the same ferrimagnetic crystalline lattice as magnetite. Its Curie temperature is between 820 K and 986K. Hematite has low ferromagnetism at room temperature. It is paramagnetic at temperatures over its Curie temperature (956 K) [8].

I. 1. 5 Electrical and optical properties of iron oxides

The materials have two energy bands:

The valence band VB, which corresponds to a band of energy completely filled with valence electrons that do not participate in the conduction of electricity,

- The conduction band CB, which is an empty band and defined as the first energy level above the valence band where the excited electrons access.

The energy average separating VB and CB is called bandgap energy.

Electrical conductivity is the ability of a material to trnsfer an electron from VB to CB, thus allowing the passage of electrical current.

There are two classes of materials depending on their load transfer capacity at 0 K: conductors and insulators. The conductors allow the passage of electric current. In their case, the two bands of energies overlap. Insulators do not allow the passage of electric current. The energy of their band gap is of the order 3.5 to 6 eV [9].

Another classification distinguishes insulators that allow the passage of electric current as soon as the temperature increases and therefore behave like conductors; they are the semiconductors. The difference between a semiconductor and an insulator is due to the width of the band gap; it is lower for the semiconductors than that of the insulators [10].

The optical properties of a semiconductor, in the visible, ultraviolet or infrared range, are strongly related to the energy of the band gap. To optically excite a semiconductor, it is subjected to light radiation with a photon energy bigger than the energy of its band gap, which induces a phenomenon of absorption of the incident photon. Note that the wavelength is inversely proportional to the energy; Thus, the corresponding wavelength absorption limit is the inverse of the energy limit.

Hematite, maghemite and magnetite are semiconductors. They have a bandgap energy of 2.2, 2.03 and 0.1 eV respectively. Hematite and maghemite absorb in the visible range. Magnetite absorbs in the infrared range [3].

I. 2 Iron oxide nanoparticles

I. 2. 1 General information on nanoparticles

A nanoparticle is a particle of size in the range (1-100 nm). At the nanoscale, the materials have characteristics differ from those of the same materials in the massive state such as melting temperature, optical properties, and magnetic properties. Thus, the color of a nanoparticle metal may be different from that of the same solid metal.

At the macroscopic scale, the surface atoms are negligible in number when compared to all the atoms that make up the particles. Consequently, they play a negligible role on the material properties. At the nanoscale, the proportion of the atoms of a particle which is on its surface increases (for example for an iron cube of 1 cm of side, the atoms percentage on the

surface is about 5-10% and for a cube of 10 nm in side, the atoms percentage on the surface is 10%). This causes a modification in the properties involving the interface interactions between the material and its environment such as the surface tension and the chemical reactivity of the particles. The increase in the proportion of atoms also influences the equilibrium shape of a crystal. Indeed, under thermodynamic equilibrium conditions, the shape of a crystal is unique [11].

In point of view, particles magnetic properties are also influenced by the nanocrystalline state, like Curie and Néeltemperatures whichdecrease significantly at the nanoscale. In addition, the magnetization process changes at the nanoscale below a critical size (Rc) of the particle. Indeed, a ferromagnetic material consisting of several magnetic domains in the massive state has only one domain at the nanoscale. A domain is a area in which the magnetic moments are aligned in one direction. As a result, nanoparticles smaller than Rc become superparamagnetic. This phenomenon occurs from a given temperature called blocking temperature, TB, above which the particle behaves as if it were not ferromagnetic [12].

Nanomaterials have specific optical and electrical properties. For example, the decrease in the number of atoms in a nanometric semiconductor induces a shift in the absorption threshold towards the upper energies, thus reflecting an increase in the band gap. Electrical conductivity can decrease or increase with the size of nanoparticles depending on the type of material[11]. Because of their miniscule size, nanomaterials show diverse biological, chemical, and physical characteristics when compared to the microscale, and macroscale counterparts (>100 nm) [13-17].The nanomaterials have a bigger surface area to volume ratio and thus a great density of surface reaction sites per unit mass. in addition, surface free energy is observed to be larger than for those of micro- or macroscale material. Nanomaterials, consequently, exhibit a higher reactivity for surface-mediated processes. on the other hand, as the size of particle approaches the electron mean-free path and wavelength scales(<30nm), quantum size effects become evident and fundamental physical characteristics are notably changed again. These effects can offset the increased reactivity as established by Sharma *et al.* [18], with many additional complete studies of properties specific to nanomaterials readily found in literature.

Also, the magnetic, electrical and optical nanoparticles properties are influenced by their size, morphology, degree of crystallinity and chemical composition. However a judicious manage of these parameters is very difficult. Therefore, the properties of nanoparticles of the same material may differ according to the methods of synthesis [19].

Nanoparticles present a great debate about their toxicological risks. Indeed, they can have adverse effects on the health and environment. This concern stems from the increasing use of nanoparticles in a variety of applications such as electronics, textiles, food, cosmetics and sun protection [20].

I. 2. 2 Applications of iron oxide nanoparticles IONPs

The various properties of iron oxide nanoparticles (magnetic, electrical, optical and reactivity) give rise to a wide range of application areas such as biomedical, water treatment, catalysis, gas sensors, lithium-ion accumulators ion, decoration and cosmetics.

I. 2. 2. 1 Medical applications

IONPs opened up a large range of attractive promise in biomedicine. This was a direct consequence of their nanometric features, which related to their physical properties at the nanometer range (particularly their magnetic properties). It is significant to emphasize that nanosystems are adequately small to allow interactions with receptor molecules while displaying a size large sufficient to carry an imaging or therapeutic payload, at the same time by passing renal clearance [21, 22]. By exceeding renal clearance step, nanosystems circulate longer, which may support their uptake in leaky vasculature regions such as tumors [23]. Because of the nanometer size range, also magnetic nanosystems present a high ratio of surface area to volume. This implies a great crossing point accessible for ligand decoration or for combining drugs/probes [21, 24]. Regularly, the physical properties of magnetic nanosystems are impacted by the nanometric size. Indeed, their magnetic properties are quite discrete in comparison to the ones from their atoms and macroscopic substance counterparts, which is a straight consequence of the actions of electrons in nanoscale confinement. In particular, once IONP size is beneath a critical value, particles exhibit superparamagnetic (SPM) properties [25]. In this situation, their magnetic moment absolutely fluctuates in reply to thermal energy. as a result, in the presence of a magnetic field, nanoparticles reveal a large magnetic moment, at the same time as the rapid moment reversals result in a zero time-averaged net moment in the nonattendance of external field [26]. This property renders SPM nanoparticles well-matched for biomedical applications reduce the risk of collective formation in the absence of permanent forces between neighboring NPs, [27].

SPM IONPs show attractive assets as they are able to

(i) Institute a locally perturbing dipolar field in the attendance of a magnetic field;

(ii) Be manipulated by an outer magnetic field gradient when IONPs experience a magnetic force leading to magnetophoretic mobility;

(iii) Engender thermal energy when is under effect of an alternating magnetic field (AMF).

From all these exceptional properties, important biomedical applications of IONPs such as contrast enhancement magnetic resonance imaging (MRI), and drug as well as cell targeting and magnetic hyperthermia, may be obtained [1].

I. 2. 2 Antibacterial activity of iron oxide nanoparticles IONPs

Bacterial infections are most important challenges for the medical domain and have become a grave menace to human health and lives. NPs use is a shows potential therapeutic approach for overcoming the rising appearance of multidrug-resistant bacteria. $IONP_s$ is one of numerous MO that have been reported to demonstrate obvious antibacterial activity allowing competent annihilation of various bacterial strains. This fact has involved major attention of , agricultural, health care, and environmental industries which are searching for novel and improved agents to control or avoid bacterial infections. Many studies have been carried out to explain the mechanisms and efficacy of antibacterial action of these nanoparticles, yet the existent literature is still unfinished and argumentative. It was established, though, that when applied at well-defined concentrations, crystal structure, and sizes, these nanoparticles are extremely successful inhibitors against a diferent kinde of bacteria. even though the precise antibacterial mechanism is still under discuss, such characteristic mechanisms have been planned, which comprise reactive oxygen species (ROS) formation, metal-ion discharge, particle internalization into bacteria causing direct mechanical damage of bacterial cell membrane (Fig. I.3). overall, MONs may exhibit bacteriostatic or bactericidal activit. In state of bactericidal activity, no bacterial colonies can be showed upon re-plating studied bacteria onto nanoparticle-free agar [28]. In case of bacteriostatic activity, bacteria stop to reproduce or grow but it do not die. If examined bacterial cells are extracted from the solution which hold nanoparticles, they re-start to grow. This can be simply tested by plating these cells onto new NP-free agar. A particular type of metal oxides NP may exhibit both bacteriostatic or bactericidal effect depending on the experimental conditions, nanoparticle concentration and bacterial strain, as shown for ZnO[29] or TiO_2 [30].

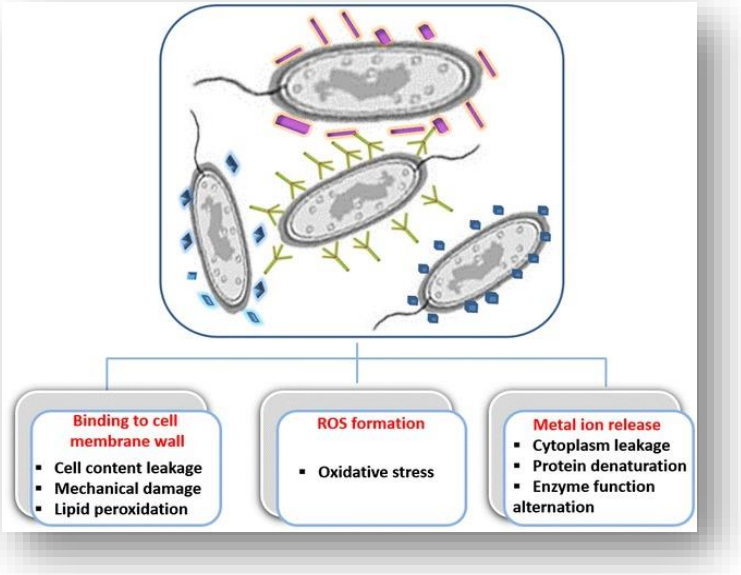

Fig. I. 3: Interaction of MONPs with bacteria. Molecular mechanisms of antibacterial effects [28].

IONPs bactericidal effect may referred to their slighter size. Lee et al. [31] elicidated that zero-valent iron nanoparticles causes an inactivation of E. coli, which could be from the diffusion of the small size of iron nano particles (10 -80 nm) into E. coli membranes, this lead to an oxidative stress and induce trouble in the cell membrane (Fig. I. 4).

Suggested method: the antibiotics and antibacterial drugs evolve oxidative stress by producing (ROS), this latter can induce damage to DNA of bacteria [32]. This bactericidal property has been clarified by Park et al. [33] from silver metals.

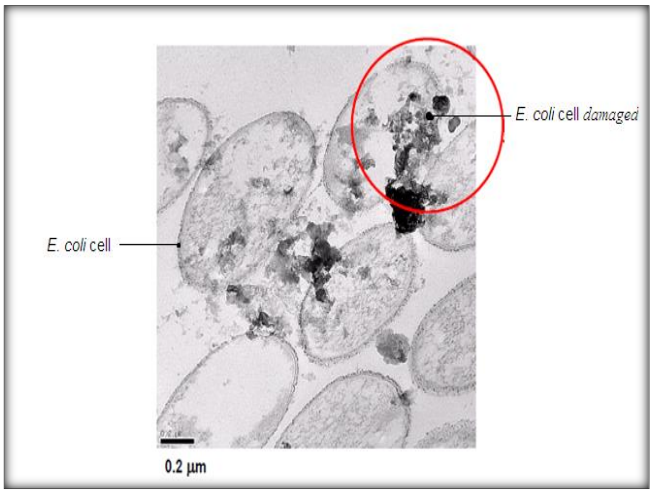

Fig.I.4. Treated E. coli cells with nano-Fe^0 [31].

When assessing dose reply and antibacterial process of IONPs, numerous factors should be investigated. Some of these containing NP synthesis, mechanism of action, zeta-potential, growth media stability, surface textures, particle shape, and the band gap energy levels, for instance oxygen vacancies on the IONPs surface could induce cellular oxidative stress. It is worth noting that IONPs are effective antibacterial agents, this data can be defined by divergence across studies in the amount of cell death/inhibition, bacterial types used, primary number of cells in contact with NP, and methods of NPs preparation and their suspensions. Frequent testing is necessary to evaluate the efficacy of IONP antibacterial toxicity dealing with a standard toxicity assessment. Supplementary studies should be achieved for well understanding IONPs mechanism against bacterial to carry better alternatives for antibiotics and disinfectants in biomedical applications [33].

2. 2. 3 IONPs for Water Treatment:

Water contamination (WC) is considered as a major international dilemma caused by domestic, industrial, and environmental influences. The United Nations guesses that300–500 million tons of heavy solvents, metals, and other waste are dispersed into the world's water supplies every year as a damaging by-product of industrial activity. WC can also be naturally derived. For instance, arsenic contamination is a grave issue in countries due to the weathering of rocks that naturally contain arsenic. In addition, while global populations continue to rise, the human effect on our water goods is expected to intensify with potentially greater possibility of pollution. During the past decade, nanotechnology has been progressively more investigated like a potential substitution for traditional treatment methods and reactive agents in order to bring clean water with a few costs even as at the same time meeting progressively more rigorous water quality standards [34].

Frequently, organic pollutants are present in groundwater, drinking water, and domestic and industrial wastewaters. In an attempt to fight the problem of water pollution, rapid and important progresses in wastewater treatment have been made, including for instance adsorption/separation processing, bioremediation, and photocatalytic oxidation [35-36]. But, their applications have been limited by many causes, such as energy requirements processing efficiency, operational method, and economic benefit.

Assortment of the best material and method for wastewater treatment is a very complex mission, which should take in account a number of factors: efficiency as well as the cost for the

quality standards to be met is needed [36-37]. Consequently, wastewater treatment technologies needs the following four conditions:

(1) Treatment litheness and final efficiency.

(2) Recycle of treatment agents.

(3) Environmental safety and kindliness.

(4) Low cost.

Magnetism is a exclusive physical property which helps in water cleansing by manipulating the physical properties of contaminants in water. Adsorption procedure gathered to magnetic separation has therefore been employed widely in water treatment and environmental cleaning [38-39]. Iron oxide NMs show potential for industrial scale wastewater treatment, because of their low cost, high capacity of adsorption, easy separation and performed stability. The ability of IONMs to remove contaminants has been demonstrated at laboratory and field tests. Recent applications of IONMs in contaminated water treatment can be separated into two groups:

- 1 - Technologies which use IONMs as a type of nanosorbent or immobilization carrier for removal effectiveness enhancement.
- 2- Those which use IONMs as photocatalysts to break down or to convert contaminants into a less toxic form.

However, it is worth noting that many technologies may utilize both processes [40].

I. 2. 2. 4 Iron oxide NPs as nanosorbents for organic contaminants

As known, for separation process, adsorption has been largely applied to take away chemical contaminants from water. It has many advantages in point view of cost, simplicity of process operation, and non sensitivity to toxic pollutants [41-42]. Therefore, low cost and an effective adsorbent with elevated adsorption capability for organic pollutants removal is enviable. IONMs are currently being investigated for organic contaminant adsorption.

Organic contaminants adsorption happened via surface exchange reactions until the surface functional sites are completely engaged, and after that contaminants are able to diffuse into adsorbent for advanced interactions with functional [43]. Taking in account this mechanism, the enlargement of NPs or NMs for organic contaminant removal requires a surface

modification expansion. NPs or NMs modification and chemical treatment are necessary to enhance the target adsorption potential. Many experiments have been done to examine the removal efficiency of organic pollutants by using iron oxide nonmaterial for organic pollutants [44]. One illustration in this area is the use of biosynthesized nano structured hematite for catalytic degradation of organic pollutants: methyl orange, methyl red, eosin yellowish and methylene blue (MB). MB pollutant recommends the possible relevance in the treatment of industrial wastewater [45].

Conclusion

In this chapter, general information about iron oxides and their properties in different sides have been illustrated, iron oxides consist of Fe, O and/or OH, they differ in composition, in Fe valence and in crystal structure. This study interests in the most stable phase which is Hematite, it considered as final form of many transformations of other iron oxides types, The crystalline structure of hematite, for its part, is of the rhombohedral type. Hematite has low ferromagnetism at room temperature. It is paramagnetic at temperatures over its Curie temperature. Hematite nanoparticles have a variety of applications such as electronics, textiles, food, cosmetics, sun protection, and also in the area of wastewater treatment and antibacterial test.

References

[1] Faivre, Damien. Iron Oxides: From Nature To Applications. John Wiley & Sons, 2016.

[2] U. Schwertmann, R. M. Cornell, Iron Oxides In The Laboratory, Second Edition, WILEY-VCH,2000.

[3] Cornell, Rochelle M., And Udo Schwertmann. The Iron Oxides: Structure, Properties, Reactions, Occurrences And Uses. John Wiley & Sons, 2003.

[4] Teja, Amyn S., And Pei-Yoongkoh Progress In Crystal Growth And Characterization Of Materials 55.1-2 (2009): 22-45

[5] Wu, W., Jiang, C. Z., & Roy, V. A. Nanoscale, 8(47), (2016). 19421-19474.

[6] Du Trémolet De Lacheisserie, E. Les Ulis (France): EDP Sciences, 2000.

[7] Jiles, D. C., And J. B. Thoelke. IEEE Transactions On Magnetics 27.6 (1991): 5352-5354.

[8] Espinosa, A., et al. Journal of nanoparticle research 15.4 (2013): 1-13.

[9] Gerl, Maurice, And Jean-Paul Issi. Physique Des Matériaux. Vol. 8. PPUR Presses Polytechniques, 1997.

[10] Neamen, D. "Semiconductor Physics And Devices (Pp. 474–483)." 2003.

[11] Luo, Haiwen, Et Al. Actamaterialia 59.10 (2011): 4002-4014.

[12] Hasany, S. F., Et Al. Nanosci. Nanotechnol 2.6 (2012): 148-158.

[13] Lövestam, Göran, Et Al. Joint Research Centre (JRC) Reference Reports 80 (2010): 00-41.

[14] Crane, R. A., And T. B. Scott. Journal Of Hazardous Materials 211 (2012): 112-125.

[15] Huber, Dale L. Small 1.5 (2005): 482-501.

[16] Jortner, Joshua, And C. N. R. Rao. Pure And Applied Chemistry 74.9 (2002): 1491-1506.

[17] Nurmi, James T., Et Al. Environmental Science & Technology 39.5 (2005): 1221-1230.

[18]. Sharma, Rakesh Kumar, Parvesh Sharma, And Amarnath Maitra. Journal Of Colloid And Interface Science 265.1 (2003): 134-140.

[19] Gubin, Sergei P., Et Al. Russian Chemical Reviews 74.6 (2005): 489.

[20] Bundschuh, Mirco, Et Al. Environmental Sciences Europe 30.1 (2018): 1-17.

[21] Kim, Betty YS, James T. Rutka, And Warren CW Chan. New England Journal Of Medicine 363.25 (2010): 2434-2443.

[22] Lewis, Daniel R., Et Al. Wiley Interdisciplinary Reviews: Nanomedicine And Nanobiotechnology 3.4 (2011): 400-420.

[23] Torchilin, Vladimir. Advanced Drug Delivery Reviews 63.3 (2011): 131-135.

[24] Liu, Zonghua, Et Al. Advanced Drug Delivery Reviews 60.15 (2008): 1650-1662

[25] Bean, C. And Livingston, J. Superparamagnetism. J. Appl. Phys., 30, (1959) S120–S129.

[26] .Pankhurst, Quentin A., Et Al. Journal Of Physics D: Applied Physics 36.13 (2003): R167.

[27] Lu, An - Hui, E. Emsp14l Salabas, And Ferdischüth. Angewandtechemie International Edition 46.8 (2007): 1222-1244.

[28] STANKIC, Slavica, SUMAN, Sneha, HAQUE, Francia, et al. Journal of nano-biotechnology 14.1 (2016): 1-20.

[29] Padmavathy N, Vijayaraghavan R. Science and technology of advanced materials 9.3 (2008): 035004.

[30] Li J, Liu X, Qiao Y, Zhu H, Li J, Cuia T, Dinga C. RSC Adv. (2013); 3:11214–11225

[31] Lee, Changha, Et Al. Environmental Science & Technology 42.13 (2008): 4927-4933.

[32] Sies, H. Expphysiol 82 (1997): 291-295.

[33] Park, Hee-Jin, Et Al. Water Research43.4 (2009): 1027-1032.

[34] Palaniappan, Meena, Et Al. Clearing The Waters: A Focus On Water Quality Solutions, 2010.

[35] Chin, Suk Fun, Suh Cem Pang, And Freda Emmanuel Idely Dom. Materials Letters 65.17-18 (2011): 2673-2675.

[36] Huang, Dong-Gen, Et Al. Journal Of Photochemistry And Photobiology A: Chemistry 184.3 (2006): 282-288.

[37] Oller, Isabel, S. Malato, And Jab Sánchez-Pérez. Science Of The Total Environment 409.20 (2011): 4141-4166.

[38] Ambashta, Ritu D., And Mika Sillanpää. Journal Of Hazardous Materials 180.1-3 (2010): 38-49.

[39] Mahdavian, Ali Reza, And Monir Al-Sadat Mirrahimi. Chemical Engineering Journal 159.1-3 (2010): 264-271.

[40] Girginova, Penka I., Et Al. Journal Of Colloid And Interface Science 345.2 (2010): 234-240.

[41] Zeng, Fang, Et Al. Nanotechnology 18.5 (2007): 055605.

[42] Hameed, B. H., And A. A. Ahmad. Journal Of Hazardous Materials 164.2-3 (2009): 870-875.

[43] Ferguson, Megan A., Michael R. Hoffmann, And Janet G. Hering. Environmental Science & Technology 39.6 (2005): 1880-1886.

[44] Zhang, Yunxia, Et Al. Journal Of Materials Chemistry 21.11 (2011): 3664-3671.

[45] .Rufus, Alex, N. Sreeju, And Daizy Philip. Journal Of Physics And Chemistry Of Solids 124 (2019): 221-234.

CHAPTER II:

METHODS OF SYNTHESIS AND CHARACTERIZATION TECHNIQUES

II. 1 Introduction

As it has been discussed in the chapter one, the study of iron oxide is motivated because of its intrinsic physicochemical properties but also due to its low-cost and non-toxicity when compared with other materials.

This chapter includes deposition details of the of hematite thin films, a description of deposition procedures, the techniques used to characterize hematite thin films.

II. 2. Chapter Objectives:

The purpose s of this chapter is:

1. determination of thin film deposition techniques.
2. identifying the experimental details correspond to Spray pyrolysis deposition process.
3. Selection of the diverse characterization methods of hematite thin films.

II. 3. Thin film Deposition Technique

Iron oxides nanomaterials synthesizing can be made through several methods, which can be normally categorized as biological, physical, and chemical manner. Fig.II.1and table. II.1 give a full representation of those methods

1. Physical methods: these are processes which use gas or solid phase and high energy treatment, they embrace molecular beam epitaxy, laser ablation, physical vapor deposition (PVD), , and sputtering [1].In physical methods, size of particles could not be controlled in the range of nanometer [2].

2. Chemical methods: these process involving solutions and temperature, they are well-organized, easy, and tractable, in which the composition, shape, and even the size of the NPs can be supervised [3]. The chemical methods include both solution and gas-phase deposition techniques (Fig. II.2). The gas-phase process contains chemical vapor deposition (CVD) [4, 5] and atomic layer epitaxy (ALE) [6], whilst spray pyrolysis [7], sol-gel [8], spin- [9] and dip-coating [10] mechanisms utilize precursor solutions. IOs can be produced through the co precipitation of Fe^{2+} and Fe^{3+} by the adding a base [11]. The shape, size, and composition of INPs prepared via chemical methods affected by Fe^{2+} and Fe^{3+}ratio, the type of salt used, ionic strength, and pH [12].

3. Biological methods. ever since a lot of MNPs are generally useful to daily life areas, friendly mechanisms of NPs ssynthesis have a great development without using toxic chemicals. solvents are more considerable during the preparation of NPs in both physical and chemical processes, when toxic elements are used in primary solutions this limits their potential employ in biomedical and other bio-based utilizations. So, a non-toxic and safe way of synthesizing MNPs is wanted in order to let them to be applied in a large area of industries. This could possibly be attained by using biological methods [13].

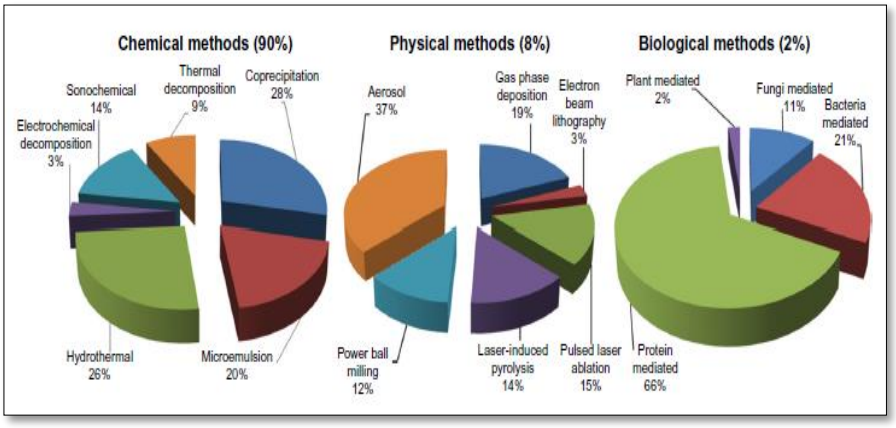

Fig. II.1 synthesis of SPIONs by three diverse way [14].

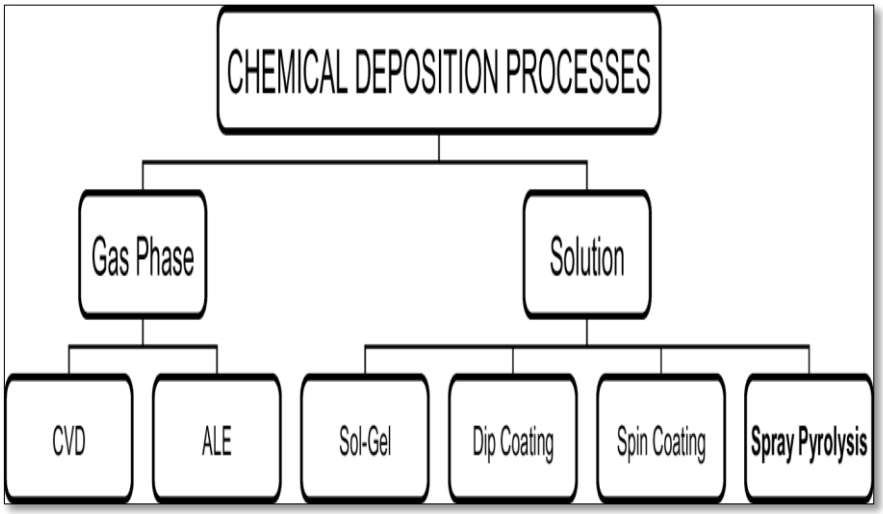

Fig. II.2 Chemical thin film deposition methods [1].

Table II. 1 Comparison of NP synthesis techniques with three parameters: product morphology, advantages, and disadvantages [14]:

Techniques		Product morphology	Advantages	Disadvantages
Physical	Deposition of gas phase	Spheres and irregular spheres	Easy to execute	Problematic in controlling the size of particle
	Electron beam lithography	Spheres and rods	Well-controlled interparticle spacing	Requires expensive and highly complex machines
Chemical	Sol–gel method	Spheres, irregular spheres, porous and nonporous spheres, or spindles	Aspect ratio, precisely controlled in size, and internal structure	High permeability, weak bonding, low wear resistance
	Oxidation	Irregular elongated and small spheres	Narrow size distribution and uniform size	Ferrite colloids of small size
	Chemical coprecipitation	Spheres	Simple and effective	Inappropriate for the synthesis of high untainted, precise stoichiometric phase
	Hydrothermal	Elongated, compact irregular spheres, and numerous shapes	Particle size and shapes are easily controllable	High pressure and reaction temperature
	Flow injection	Small rods, irregular spheres, sheets, or rhombic shapes	Homogeneity with high mixing with a accurate control of the procedure and good reproducibility	Under a laminar flow regime in a capillary reactor, it requires continuous or segmented mixing of reagents
	Electrochemical	Spherical NPs, nanorods, hexagonal nanocrystals, and facets	Controllable particle size	Inability to reproduce
	Aerosol/vapor phase	Mesoporous single crystals and small particles, octahedral cages	Large-scale products	Requires very high temperatures
	Sonochemical decomposition	Bipyramids, spheres, or truncated rods	Size distribution in narrow particle	Still, mechanism is not well understood
	Supercritical fluid method	Mesoporous single crystals, elongated irregular nanotubes	No organic solvents involved and efficient control of the particle size	Requires high temperatures and critical pressure
	Using nanoreactors	Spheres, hollow and spherical NPs	Likelihood to specifically control the size of NPs	Complicated conditions
Biological	Microbial incubation	Small platelets, spherical or rod-like spheres, irregular spheres	Good reproducibility and scalability, high yield, and low cost	Slow and laborious

II. 3. 1 Synthesis Pathways

Preparation of IOs in aqueous systems require two process: nucleation and crystal growth, they will be presented briefly below as a background to the synthesis methods described in this chapter.

II.3 .1. 1 Nucleation

Homogeneous nucleation happens involuntarily in bulk solution when the supersaturation goes beyond a specific critical value. The necessary condition for precipitation

to take place is the creation of embryonic and stable clusters of molecules or ions, the so-called nuclei, in solution. These developing nuclei form as the consequence of collisions of ions or molecules in the bulk solution prior to nucleation. The embryos are frequently failing and restructuring The stability of an embryo vary upon an equilibrium being realized between the free energy needed for the creation of a novel interface, the interfacial or surface energy, $\Delta G_{surface}$and the energy released by the bulk bonds construction, ΔG_{bulk}. The free energy of nucleation, ΔG, is the sum of these two energies. just when the embryo goes beyond a specific significant size, does ΔG_{bulk} predominate. This leads to a growing of the nucleus by a reduce of free energy. The smallest embryo that can in fact maintain to grow to a crystal becomes smaller named the critical nucleus, the lower the interfacial free energy.

ΔG_N is governed by essential parameters such as the supersaturation of the solution, the interfacial energy of the nucleus, and ΔG_{suface}. because the rate of nucleation, J_N, is connected to ΔG, these parameters also affect J_N. The rate of nucleation is slow until a specific supersaturation is attained, after which it increased quickly.

When a solid be able to exhibit more than one phass with diverse solubilities (e.g. as goethite and ferrihydrite), the more soluble phase is often the primary precipitate, even though it may be probable that the inverse must happen (the less soluble phase form firstly) because, the supersaturation in this phase, is higher. However, if the interfacial energy of the specific nucleus of the more soluble phase is lower than that of the less soluble phase, the more one may precipitate first, this is due to that the rate of nucleation related to interfacial energy also to the degree of supersaturation. In other hand, the primary precipitate may, however, consequently alter into the less soluble phase due to its higher solubility. This behavior, which leads to instability in the primary formed polymorph, is related to as the Ostwald Law of Stages: it happens quite frequently in the IO system.

Heterogeneous nucleation happens when the attendance of a solid phase decreases ΔG, and thus procure to an augmentation in J_N. The substrate might be minute particles of an alien crystals of the phase which is crystallized.

Heterogeneous nucleation may happen at less supersaturation than is necessary for homogeneous nucleation. The aptitude of a strange solid as a substrate is generally a issue of the correspondence degree between atomic distances and structure type, rather than the chemical likeness of the two solids. With a good connection between the substrate and structures of the crystal (<20 % difference) the difference in the interfacial free energy between

the substrate and a given crystal face is inferior than that between the solution and same crystal face, hence nucleation is simplify [15].

II. 3. 1. 2. Crystal Growth

Even though a definite degree of supersaturation is required for crystal growth, it is more less than that needed for nucleation. Crystal growth includes many steps such as diffusion and adsorption procedures at the crystal surface, and diffusion of the growth units to the surface itself. The total rate of growth is defined by the tardiest of those steps. The habit of the crystal is controlled by the growth rates of the diverse faces. Those later which grow bit by bit tend to persist, while fast growing faces are removed. the growth rates of different faces may be altered by the strange species which are adsorbed on the surface of the growing crystal and thus cause a vary in crystal habit. This is an ordinary phenomenon in the IO system [16].

II. 3. 1. 3. Production of Monodispersed Particles

The extensive range of particle sizes of IO samples indicates that nucleation and crystal growth occurred at the same time over the bulk of the reaction. Preparation of oxides with slight range of particle sizes and also with diverse shapes (so-called monodispersed products) have a great interest in recent years, this attention has been catalyzed by the fact that optical, electronic, magnetic, and catalytic properties can differ clearly with particles hape and also size. Monodispersed iron oxides constitute perfect systems for original investigations into these properties. They are also frequently utilized for examining dissolution and adsorption processes.

The methods by which monodisperse particles shape are not completely understood while the availability of large number of papers, particularly on monodispersed hematite with a variety of crystal shapes, has been presented by, for instance, Sugimoto and coworkers and by Matijevic and coworkers. in the beginning, it was presumed that the essential requisites for preparation of monodisperse particles are taking apart of nucleation and crystal growth and a continuous providing of growth units, i. e. interactive, low-molecular weight ionic species. The providing of nucleation and growth can be attained by organizing the reaction conditions so that there is slow generation of growth units pending the specific supersaturation for nucleation is surpassed at which point the supersaturation is minified by a rupture of nucleation. later, the

nuclei take up the growth units. Their rate of creation must be adequately slow, so that the nuclei remove them totally i. e. growth units concentration never attain a elevated level for additional nuclei creation. Slow creation of growth units can be realized with pleasure by the supervised providing of a solid precursor dissolution or soluble iron complex, for instance 2-line ferrihydrite [16].

The used Methods for monodispersed production of IOs consist of compelled hydrolysis (i. e. hydrolysis at high temperatures) of acidic Fe^{III} solutions under clear situations, the sol-gel method, seeding throughout compelled hydrolysis and using solution transformation from both a soluble or a solid precursor. The seeding method was used by Penners (1985) to compelled hydrolysis of Fe^{III} solutionsto create monodispersed hematite crystals with sizes in the range (0.15-0.56 pm). further interest has been intended for hematite synthesis, even though, identical spheres of magnetite were created by partial oxidation of $Fe(OH)_2$ at high pH, also acicular goethite has been synthesized by hydrolysis of Fe^{III} solutions [17].

II. 3. 1. 4. Production of Nanoparticles

Synthetic IOs size is frequently in the micron or submicron range. particular techniques are often needed for NPs synthesis, which are not required for the larger crystals. The two essential necessities for a monodisperse system must be get together and in addition, coagulation and/or contact re-crystallization of the main particles must be precluded.

If precipitation is happened a pH depart from the point of zero charge (PZC), coagulation can be forbidden by revulsion of the electrical double layers of the particles. Precipitation of maghemite nanoparticles, for instance, is carried out at pH 2 [18]. on the other hand, a repulsive force, (relating electrostatic or steric obstacle) can be established by defensive agents adsorption on the particles surface; such as, monodispersed IO was formed by iron pentacarbonyl oxidation with H_2O_2 in ethanol. The alcohol assisted the stabilization of particles next to coagulation [19]. Other workers have utilized gel systems or supports or vesicles to make sure the separation of the particles. The supports can offer a template or even a framework for growth in addition to avoiding coagulation/ agglomeration. Well strewed maghemite or hematite nanoparticles have been synthesized in silica xerogels [20-21-22]; such particles have been utilized to examine magnetic phenomena.

The IO is typically subsumed in the support and inseparable from it. Such elements are presented inorganic/organic compounds They are favorable for studies of elastic and magnetic

properties. A connected synthesis includes magnetic paper preparation by in situ precipitation of magnetite and/or maghemite ensued by entrance of the inorganic particles into the cellulose fibers lumen; excess of IO is washed [16].

II. 3. 2. Main ways of Synthesis

Approximately all the IOs and hydroxides can be synthesized by many preparations process. The way followed often affects the product properties, especially sample surface, degree of crystallinity, crystal morphology, area and water content. The most important preparation methods are explained below.

II. 3. 2. 1. Hydrolysis of Acidic Solutions of Fe^{III}salts

When pH <1, Fe^{3+} subsists as the violet, hexa-aquo ion, $[Fe(H_2O)_6]^{3+}$. Hydrolysis requires gradually protons elimination from the sixwater molecules that envelop the central iron cation to form both mono- and binuclear species. These latter then react further to create species of elevated nuclearity [23-25]. The latter precipitate finally as a less or more crystalline product, the nature of which relies the conditions and rate of reaction. exemplars of polymerization and hydrolysis reactions are:

$$Fe^{3+} + H_2O \rightarrow FeOH^{2+} + H^+$$
$$2\,Fe^{3+} + 2H_2O \rightarrow Fe_2(OH)_2^{4+} + 2H^+$$
$$FeOH^{2+} + H_2O \rightarrow FeOOH + 2H^+$$
$$2FeOH^{2+} + H_2O \rightarrow Fe_2O_3 + 4H^+$$

Times of precipitation can vary from seconds to years. The two major mechanisms utilized to stimulate hydrolysis in the laboratory are, I) solution heating and 2) addition of base. because hydrolysis eliminates protons, the system PH decreases during the early steps of hydrolysis. When hydrolysisis stimulated by elevating the temperature, the pH might decrease to a little value to restrain further hydrolysis. This pH slump is significant since unfinished hydrolysis minimise the product yield.

Ferrihydrite, goethite, akaganeite and Hematite, may be procured by hydrolysis of Fe^{III} solutions (Fig. II-3). Which product forms is affected by various factors as well as solution pH, rate of hydrolysis, [Fe^{III}], temperature, and the characteristic anions existing in the system [16].

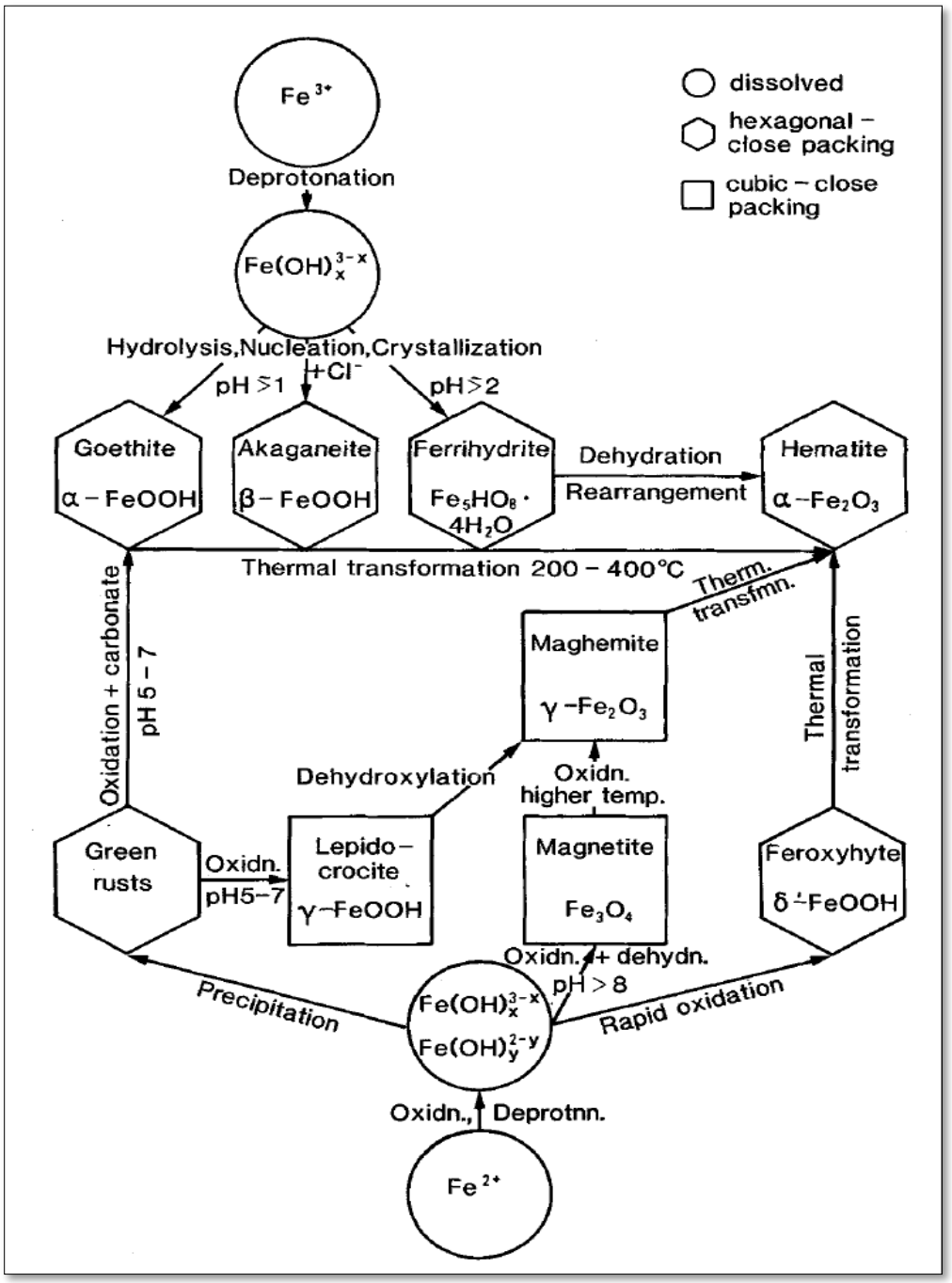

Fig II. 3 Schematic presentation of frequent formation and transformation pathways of common iron oxides together with the approximate formation conditions [16]

II. 3. 2. 2. Oxidative Hydrolysis of Fe^{II} Salts

This is a very multitalented method able of generate magnetite, lepidocrocite, goethite, feroxyhyte and ferrihydrite. Those product forms are affected by the reaction parameters. Delicate manage of pH, temperature, suspension concentration, rate of oxidation, and concentration of foreign pecies is required to guarantee that a clear product is procured [26].

The reaction can be approved when the pH is in the domain (pH: 6-14). In the range (pH: 6-7) lepidocrocite and goethite produced: a clear product of both can be procured by regulating the concentration of carbonate, and the rate of oxidation in the system [27]. In the case when pH >8 magnetite is produced and when (pH=14), clear goethite is obtained. The oxidation/hydrolysis reaction eliminates protons, in order that, if no extra base is added and as the transformation continues, the pH goes down to about 3 and the transformation rate decrease to nearly zero, thus leads to incomplete oxidation:

$$4\,Fe^{2+} + 6\,H_2O + O_2 \rightarrow 4\,FeOOH + 8\,H^+$$

Consequently, to get an elevated yield of logically product with well crystallite, the pH have to be steady by frequent adding of alkali to the system. This is mainly befittingly attained by utilizing an automatic burette and the technique of pH-stat titration. The reaction is finished when no more addition of alkali is nessacery.. The oxidation/hydrolysis of Fe^{II} systems have a specific aspect is that the crystalline product can be procured in a few hours at room temperature [16].

II. 3. 3. Spray pyrolysis technique

Spray pyrolysis is a procedure wherein a thin film is synthesized by the spray of a solution on a heated substrate, where the ingredients interact to produce a chemical compound. [28].usual spray pyrolysis apparatus combines of a precursor solution, atomizer, substrate heater, and temperature manager. The usually used atomizers in spray pyrolysis technique are listed below:

- A**ir blast** (the liquid precursor is subjected to air flow) [29];
- **Ultrasonic** (short wavelengths necessary for fine atomization are produce by ultrasonic frequencies) [30];

- **Electrostatic** (the liquid solution is subjected to an elevate electric field) [31].

The process of chemical spray can be splitted into three steps corresponding to the nature of reaction: In the first step, the solution droplets deposited on the heated substrate when the solvent components evaporate and a dry state reactions occur. The second step signify an event in which the evaporation of the solvent happens earlier than the drops be on the heated substrate and the dry solid impacts on the surface by decomposition. In the last step, there are procedures where the solvent vaporizes when the droplets come up to the substrate with the resulting heterogeneous reaction of the composition of the main solution. The most significant factors to be managed in all of these operations are the solution content and concentration, rate of carrier gas stream, nozzle-to-substrate distance, and substrate temperature. Through those variables, the temperature of the substrate has been presumed as the mainly essential factor in synthesizing thin film via spray pyrolysis mechanism; this is referred to crystallization, decomposition, droplets drying, and grain growth which are affected directly by this parameter [32].

II.3.4. Process sequence during deposition by Spray Pyrolysis

The spray pyrolysis deposition process can be generally simplified by scheme shown in Fig. II. 4; where three processing steps are presented.

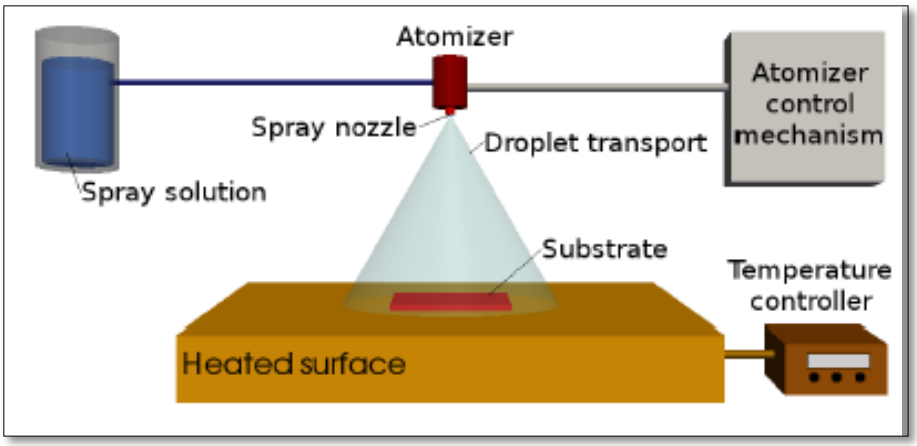

Fig.II-4. Schematic diagram representing the Spray pyrolysis technique [33]

II. 3. 4. 1. Precursor Atomization

The first step in the spray pyrolysis deposition technique is the atomization procedure. The main idea is to produce droplets by spraying a solution, those droplets which have some

initial velocity, will be sent towards the substrate surface. One atomizer differs from others in resulting rate of atomization, droplet size, and the primary velocity of the droplets. It has been revealed that the produced droplet size is not connected to any fluid characteristics of the precursor solution and affects exclusively on the charge in fluid density level ρ_e as shown in literature [33].

$$r^2 = \left(\frac{-\alpha'}{\beta'}\right)\frac{3\epsilon_0}{q\rho_e}\ , \qquad \text{(II.1)}$$

where r is the droplet radius,ϵ_0 is the permittivity, q is the elementary charge, and $\frac{-\alpha'}{\beta'}$ is a constant (~1.0×10^{-17}J). By assuming the droplet has a spherical shape, its mass depends on its density:

$$m = \frac{4\pi}{3}\rho_q r^3\ , \qquad \text{(II.2)}$$

whereρ_q is the density of droplet. The initial abandoning speed of the droplet is a significant factor as it defines the rate of reaching the substrate surface by droplets, the rate of droplet heating, and the transportation period of the droplet. Due to its ease of production, an air draft or pressure atomizer utilizes elevated speed air to facilitate the generation of aerosol from a precursor solution. Rising the pressure of air brings a direct reduce in the produced mean droplet diameter. while, rising the pressure of the liquid brings a direct augment in the mean droplet diameter [34]. Perednis confirmed that all of the sprayed droplets from an air draft atomizer are restricted inside a 70^o spray cone angle, even as half are inside a cramped angle (12^o) [35]. In addition, it was indicated that the flow rate has a very small effect on the spray characteristics, which can be typically neglected for presenting [34].

II. 3. 4. 2. Aerosol Transport of Droplets

After the droplet departs the atomizer, it moves throughout the ambient by a primary velocity defined by the atomizer. In the aerosol state, the droplets are moved with the mean of as lots of droplets as possible accessing the surface. As the droplets travel throughout the ambient, they practice chemical and physical variations illustrated in Fig. II. 5.

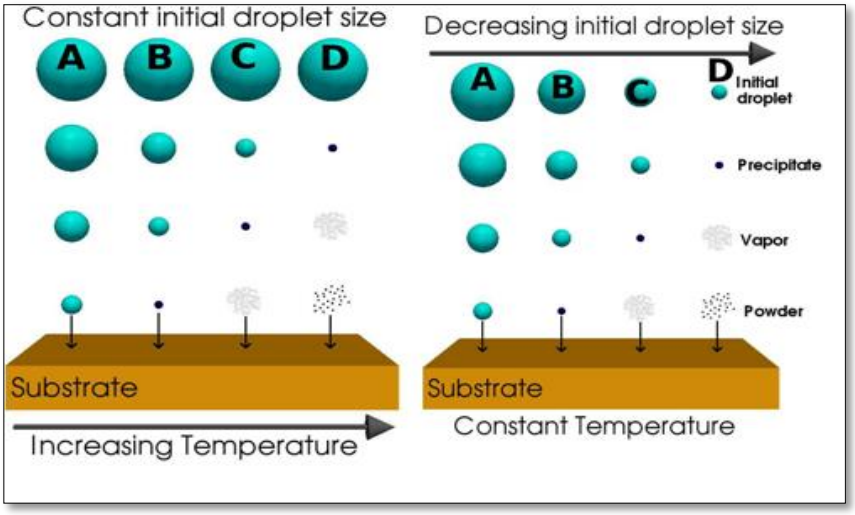

Fig. II. 5. Droplets in Spray pyrolysis mechanism modifying as they are moved from the atomizing nozzle to the substrate. Alike the temperature or the initial droplet size are changed, there are four potential pathways which the droplet can take as it moves in the direction of the substrate (A-D) [34].

Since the droplet pass through the ambient, four forces which are: thermophoretic, gravitational, Stokes and electrical force acting on it at the same time, explaining its path. As shown in **Fig. II. 5**, the droplets practice evaporation through their air travel, which influences the effect of the forces on their flight. a number of experimental consequences from literature [36] show the ability of solid particles formation, as the temperature of reactor is low, as the flow rate of the carrier gas (N2) is low, and as the concentration of precursor solution is high.

1) Gravitational force: It is the force that drafting the droplet down. Its value relies on the mass of the moving droplet, as given by equation (II.2). The gravitational force is too small For small droplets to let it to reach the surface before it is completely evaporated. For the larger droplets, the gravitational force follows the droplet transportation.

2) Electrical force: It is valid to spray pyrolysis systems, which comprise an extra electrical source prevailing the droplet's flight. as an air blast atomizer is utilized, the elevated velocity of air is the reason of aerosol and atomization generation. Ultrasonic atomizers are driven by electricity, whereby an electric generator is vibrated at ultrasonic frequencies through a titanium nozzle. Elevating the frequency leads to smaller droplet sizes. At the liquid-gas interface, electric spray deposition (ESD) atomizers require a strong electric field to produce charged droplets. so, air blast atomizers do not have further input from an electrical force, also the droplet flight is driven by the initial speed and the gravitational force, even as for spray pyrolysis deposition utilizing ultrasonic and ESD atomizers,the electrical force is the most important factor which takes the droplets downwards. The electrical force acting on a droplet

is frequently a number of orders of magnitude higher than the gravitational force [37]and is given by:

$$F_e = q_d E \qquad \text{(II.3)}$$

where E is the strength of the produced electric field, and q_d is the droplet charge. $q_d$relies on the sequential change of the droplet, it is given by:

$$q_d = \sqrt{\gamma \epsilon_0 r^3}.\frac{t}{t+t_0} \quad , t_0 = \left(\frac{4}{b\vec{V}.\vec{E}}\right), \qquad \text{(II.4)}$$

where γ is the surface tension of the liquid-gas, ϵ_0 is the electrical permittivity, and b represents the ionic mobility [38].

3) Stokes force: It is the dragging faced by the droplet as a result of the air resistance in the ambient. The force is originated by the friction between the air molecules and droplet. The Stokes force is a parameter of the particle's size and speed. Consequently, large droplets moving with an elevated speed will practice the major retarding force.

4) Thermophoretic force: It is a retarding force, triggering a decrease in droplets velocity as they come near the heated substrate. It is obvious that the air temperature augments sharply as a result of the effect of forced convection cooling of the air flow when come near the heated substrate. Since the thermophoretic force relies on the thermal gradient in the transport environment, it can be deduced that it will not be able to act on the movement of the droplet, as it is higher than several (~5-7 mm) apart from the substrate. Though, in the range of this elevated thermal gradient, the thermophoretic force predominated, it is the case for (PSD) systems, where the chief driving force is gravity; but, for ESD systems, the electrical force is frequently stronger than the thermophoretic force [35].

II.3.4.3. Precursor Decomposition

As the precursor, moves through the heated ambient, it passes through a variety of changes, which are showed in **Fig. II. 5**. Evaporation, precipitate formation, and vaporization all happened relying on ambient temperature and droplet size. The droplet might react with the substrate surface. Though all processes happen during deposition, process C, the CVD-like deposition is preferred to yield film with high dense quality [32].

Since the processing environment purposes a previous evaporation of droplets to reaching the surrounding area of substrate, a precipitate will happen early. When the precipitate

achieved in the immediate surrounding area of the substrate, it is changed into a vapor state, and it experiences a heterogeneous reaction during the subsequent steps:

1) Reactant molecules spread to the surface;
2) Adsorption of few of molecules at the surface;
3) Chemical reaction and surface diffusion, combining the reactant into the lattice;
4) Diffusion and desorption of the produced molecules from the surface;

This is a standard CVD reaction, which induces a high sticking probability, and high quality film deposition.

In step D in **Fig. II. 5**, when small primary droplets are created, or the temperature is sufficiently high, the droplet rapidly forms a precipitate. As the precipitate comes near to the substrate, it is vaporized and a chemical reaction then happens in the vapor phase. This homogeneous reaction leads to molecules condensation into crystallites forming a powder precipitate. This latter falls to the substrate surface but without a deposition reaction [33].

II. 3. 5 Important Parameters

The properties of the spray deposited films are defined basically by the growth conditions throughout their deposition. A lot of factors can influence the growth mechanism and adapt the films structure. In general some steps are necessary i the thin film deposition procedures: decomposition, nucleation and coalescence supervened by diverse growth procedures, as particular cases of crystal growth (columnar, polycrystalline, epitaxial). Accordingly following are the factors affecting the above processes:

II. 3. 5. 1. Core Temperature

The core temperature i. e. the reaction temperature should be optimum so that the sprayed solution aerosols could undergo decomposition process. If the core temperature is less than an optimum value (for optimum air pressure - or optimum nozzle-substrate distance) the sprayed aerosols will directly arrives at substrate, without proper decomposition. In such as case, no reaction will be observed and rather than solid-vapor phase merely semi-solid deposits will arrive at the substrates and due to lack of thermal energy at the substrate surface, non-adherent film will form. On the other hand, if the core temperature is higher than its optimum value (for optimum air pressure-or optimum nozzle-substrate distance), the oxidation reaction

occurs totally in the gas phase and inhomogeneous oxide particles or clusters are deposited on substrates without adherence. Thus the core temperature is recommended to set at the decomposition temperature of the relevant precursor salt.

II. 3. 5. 2. Atomizing Air Pressure

If air pressure atomizing the spraying solution is higher than optimum value (at the optimum core temperature); the atomized aerosols will be of very minute sized. In this case, thermal energy experienced by aerosols will be much larger in order that much earlier decomposition will result into (very thin) powered film on the substrates. Whereas if the air pressure is smaller than its optimum value, aerosol size will be much larger so that the solvent can vaporized, but the precursor is not completely decomposed in their way. This will result into the powder deposits.

II. 3. 5. 3. Nozzle to Substrate Distance

This parameter has the similar effects resembling the atomizing air pressure. In fact both these parameters are mutually dependent. The decreasing nozzle-substrate distance will introduce the nozzle tip to the increasingly hot ambient which can result into the blockage of the nozzle. Conversely increasing nozzle-substrate distance will increase the aerosol traverse path. This will cause the aerosols to experience thermal energy further and either powdered films or no deposition will result. Therefore, it is suggested that the nozzle-substrate distance and atomizing air pressure should be optimized mutually.

II. 3. 5. 4. Substrate Temperature

Similar to the conventional route, the substrate temperature in the spray pyrolysis is the foremost parameters which have the profound influence on the film properties. As the intent behind the development of advanced spray technique is to prepare the films atlower temperature than that required in conventional spray pyrolysis method, there are deliberately enforced limitations over the substrate temperature. Therefore, the role of substrate temperature in the present case is not to undertake decomposition reaction but merely limited to the nucleation and coalescence, followed by different growth processes. As a result, this important parameter will

certainly affect structural, morphological, optoelectronic properties. Furthermore, insufficient substrate temperature results into the amorphous films; while the increasing substrate temperature will increase the film crystallinity. In case of the insufficient substrate temperatures, low average kinetic energy will adversely affect the distribution of the deposits and consequently the agglomeration of the grains may tend to form large clusters [39].

II. 3. 6. Spray pyrolysis method with moving nozzle (SPMN)

As indicated previously, physical methods cannot be able to manage precisely the size of synthesized particles in the nanometer range; such as, classical spray squanders a long time prepare a sample (i.e miscarry more than 1hour to elaborate one sample). To avoid this loss time, a moving nozzle have been induced to maintain the heat of substrate through the elaborating duration as described in Fig. II. 6.

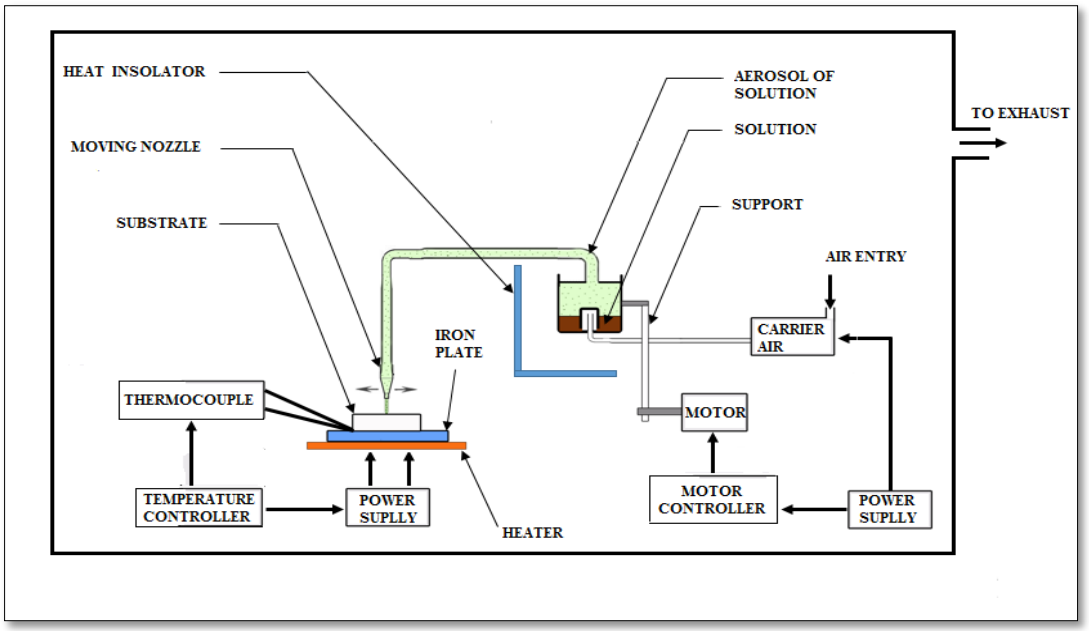

Fig. II-6. Spray pyrolysis technique with moving nozzle (SPMN)

II. 3. 7. Growth process details

II. 3. 7. 1. Substrate Preparation

The substrate is the first main support for the substrate growth, In this work glass substrates (Ref 217102: having 7.5x2.5x0.13cm^3 as dimensions) have been used. The substrates were thoroughly cleaned, to avoid thin film contamination, then rinsed with distilled water for

several times and subsequently dried at room temperature. Before each deposition, the substrates were putted at 500°C- the value required for the deposition- and left to settle for 30 min in order to keep consistency between depositions. After deposition, the substrate was cooled in the gas environment at which it was deposited in.

II. 3. 7. 2. Preparation of precursor solution

To get the primer solution with concentration of 0.5M of Fe^{+3}, 1.622g of iron chloride ($FeCl_3$) was dissolved in 20mL of distilled water and ethanol mixture in volume ratio 1:1 and stirred vigorously until complete dissolution (red brownish solution). Doping with cobalt were obtained by adding different quantities of cobalt chloride $CoCl_2$ to primer solutions to get a wide range of doping concentration, all process were carried out in good conditions of hygiene to avoid any impurities entering the solutions.

II. 3. 7. 3. Films deposition:

After preparing the substrates and the solutions, it is time for precipitation. The obtained blends were sprayed onto 500°C heated glass substrates, the deposition time was 3min with 5ml/min as the rate of spray, nozzle to substrate distance is fixed to be 5cm. The prepared slides were annealed for two hours at 550°C.

II. 4. Thin film Characterization Techniques

The growth process, characterizations, and specifications of thin films can be well comprehensible by a selection of investigative methods. earlier than utilizing the prepared films in such application, one has to analyze film characteristics to attain select performance of the prepared films. The whole description of every material combines of structural elucidation, micro-structural analysis, synthetic and surface characterization, which have strong relation with materials properties. In the present work, the structural, morphological, optical analysis was bring out using X-ray diffraction, scanning electron microscope (SEM), and optical spectroscopy.

II. 4. 1. X-Ray Scattering Techniques

The essential notions behind the interactions and scattering of radiation by material relate into the diffraction theory, are given by two equations which are used in this context of work:

Geometrical diffraction shows that the scattering angles referred to diffracted intensity maxima (i.e addition of two maximum) can be illustrated by the Bragg equation [40]:

$$2dsin\theta = n\lambda \qquad \text{(II.5)}$$

where d, θ and λ are the inter planer spacing, the diffraction angle, and the wavelength of X-ray, respectively. Whereas n is the order of diffraction. Fig. II. 7 shows the geometrical conditions of Bragg diffraction from a set of spaced d_{hkl} $\{hkl\}$ planes, with X-rays incident at a Bragg angle θ being diffracted through an angle 2θ . The path difference between the X-rays reflected from successive planes must be equivalent to an integer number of wavelengths n for constructive interference to occur [39], n is taken equal to 1 in this work.

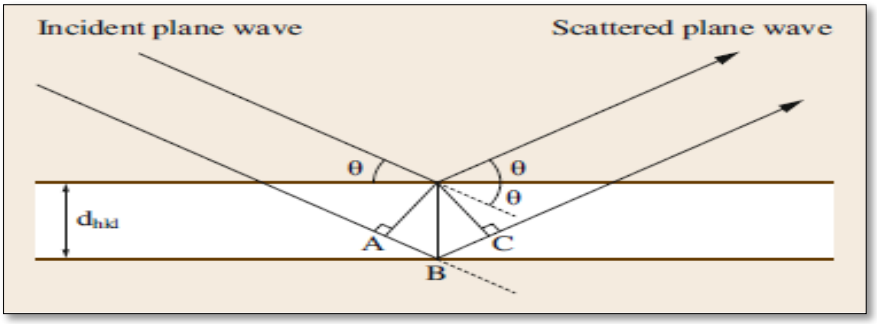

Fig. II-7 Illustration of Bragg diffraction. For constructive interference, nλ=AB+BC =2d sinθ [39]

According to Bragg's law, for the specific d value, the constructive interference of X-rays appears only at determined 2θ value (i. e Bragg's angle). For all other angles, they are considered as destructive interference and intensity of diffracted beam will not be detected in experimental conditions.

In the case of thin films, each particle of the product is a semispherical tiny crystal, or assemblage of smaller crystals, randomly oriented with respect to incident X-ray beam. It means that thin films can be considered as single crystal or powder. It is worth noting that a typical epitaxial or oriented film does not exhibit all corresponding reflections, for example , a c-axis oriented film in ZnO for instance will exhibit only (*hkl*) for which h and k indices are nil and l

differs from zero. However, these hidden peaks can be detected by small angle X-ray diffraction technique [39].

II. 4. 1. 1. Identification of Phases

Phase identification of thin films is one of the important uses of XRD, it is done by comparison of the measured d spacing in the X-ray diffraction pattern and, with known standards ones in the JCPDS Powder Diffraction Files (Joint Committee on Powder Diffraction Standards) and the reflections can be indexed with Miller indices.

II. 4. 1. 2. Grain size determination:

Scherrer's formula [41], leads to estimate the grain size D as follow:

$$\boldsymbol{D = \frac{0.9\lambda}{\beta cos\theta}} \qquad \text{(II.6)}$$

where λ, θ, and β are the X-ray wavelength (1.54056 A°), the Bragg diffraction angle of the XRD peak (in degree), and the full width at half maximum in radian (FWHM) of the most intensive diffraction peak, respectively. It is advised to take in consideration all peaks and gives the average of D.

Deducing the lattice constants a and c of the iron oxide crystal lattice is made via The XRD spectra as the relation illustrates [42]:

$$\boldsymbol{\frac{1}{{d_{hkl}}^2} = \frac{4}{3a^2}(h^2 + k^2 + hk) + \frac{l^2}{c^2}} \qquad \text{(II .7)}$$

where 'd_{hkl}' and (*hkl*) are the inter-planer spacing and Miller indices, respectively.

II. 4. 2. Scanning electron microscope (SEM)

Interaction of electrons with elements is well comprehend and has been widely used for investigating of the materials. By focusing electrons on sub-micron sized areas or features can give us the ability to analyze the surface and contents of the matter: as an electron strikies the atom, diversity of interaction products are developed [43]. Fig. II. 8 shows the sections from which different signals are detected.

Instead of light waves which are used in conventional microscopes, scanning electron microscope utilizes electrons to observe the morphology of a sample at higher intensification,

with greater resolution and focus depth, also gives information on the microstructure of the sample via backscattered, secondary, and transmitted electrons, hence the element from which they are coming gives information about the chemical, identification and composition of the sample as shown in Fig. II. 8.

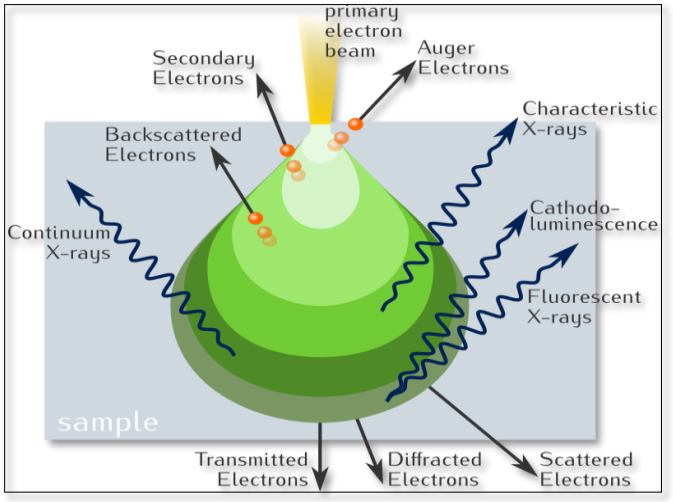

Fig.II-8: Illustration of several signals generated by the electron beam–specimen interaction in the SEM and the regions from which the signals can be detected .

Getting SEM images is to registered current induced by the upcoming of the three sorts of electrons. The three signals which provide the greatest amount of information in SEM are the secondary, backscattered, and X-rays electrons. In this study, only morphological.images of the surface and composition of the product will be taken in consideration via:

Atoms occupying the top surface are responsible for emitting secondary electrons then a readily interpretable image of the surface can be produced. The contrast in the image is defined by the sample morphology. A high resolution image can be obtained due to the small diameter of the primary electron beam.

Energy Dispersive X-ray Spectroscopy or EDS provide rapid qualitative and quantitative analysis of elemental composition with 1-2 microns a sampling depth via interaction of the primary beam with atoms in the sample [39].

II. 4. 3 Optical Absorption Studies

Incident photon on any material might be transmitted, absorbed, or reflected. The absorbed radiation in a material is due to inner shell electrons, valence band electrons, free carriers as holes and electrons, and electrons bounded to contained impurity centers or defects.

Essentially there are two forms of optical transitions that can happen at the basic edge of the crystalline semiconductor, direct and indirect. The two types involve the interaction of a photon with an electron in the VB, which is climbed across the essential gap in the CB. However, indirect transition also requires simultaneous interaction with lattice vibration. The direct inter band transition involves a vertical transition of electrons from VB to CB such that there is no change in the momentum of the electrons, and energy is conserved as shown in Fig.II. 9 (a), hence a wave vector **k** for electron remains unchanged in E-k space. For direct transition, the optical transition is denoted by a vertical upward arrow. the absorption coefficient α for simple parabolic bands is given by the relation [39].:

$$\alpha = \frac{\alpha_0 (h\nu - E_g)^n}{h\nu} \qquad \text{(II .8)}$$

where, *Eg*, and *hv* are the separation between bottom of the CB and top of the VB (band gap) , the photon energy; whereas α_0 is a constant depending upon the transition probability for direct transition and *n* is constant and equals to 1/2 or 3/2 depending on whether transition is permitted or non.

For permitted direct transitions *n* =1/2 and for permitted indirect transition *n* = 2. Thus if the plot of $(\alpha h\nu)^2$ against *hv* is linear then the transition is direct permitted. The band gap energy Eg is defined by extrapolating the linear portion of the curve to the energy axis as α=0.

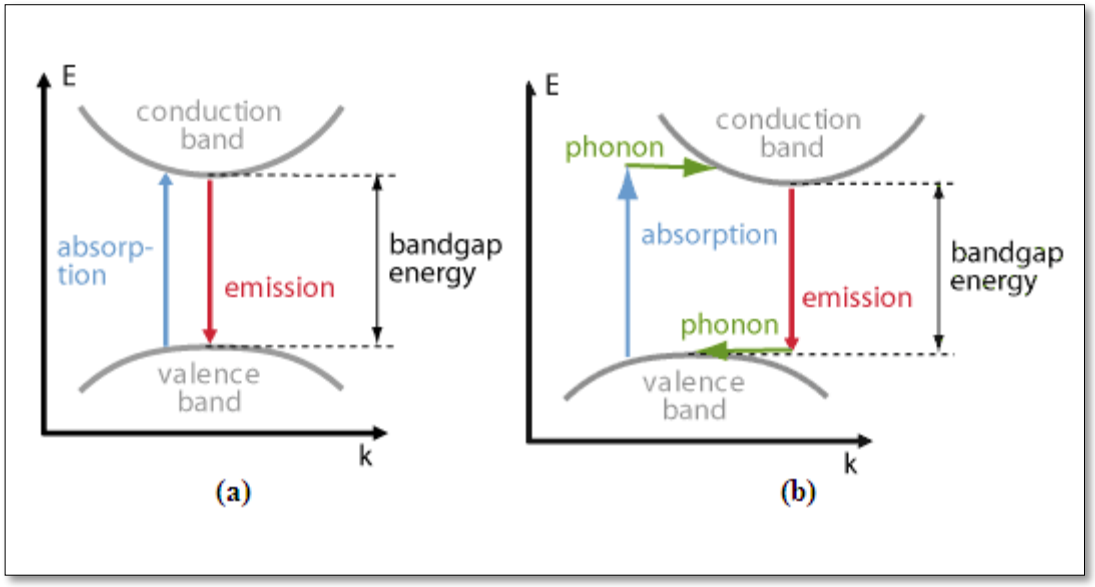

Fig. II-9: (a) Direct and (b) Indirect interband band transition.

When indirect transition takes place between different k-states, the momentum must be conserved; the only way is through the emission or absorption of a phonon. So absorption coefficient α becomes,

$$\alpha = \frac{\alpha_0(h\nu - E_g)^2}{h\nu} \quad ; \; Eg = Eg' \pm Ep \qquad \text{(II .9)}$$

where, Eg', Ep are the indirect band gap energy and the phonon energy. For permitted transition $n = 2$ and for forbidden transition $n = 3$. The band gap energy is deduced by extrapolating the linear portion of the plot $(\alpha h\nu)^n$ versus $h\nu$ to the energy axis at $\alpha = 0$ [44].

II. 4. 3. 1. UV-Vis spectroscopy:

Transmittance is the fraction of light that passes through the sample. This can be calculated using the equation [45]:

$$T = \frac{I}{I_0} \qquad \text{(II .10)}$$

where *Io* and *I* are the light intensities before and after the beam of light passes through the cuvette. Transmittance is related to absorption (A) by the expression:

$$A = -log(T) = -log(\frac{I}{I_0}) \qquad \text{(II .11)}$$

Absorbance usually depends on the absorbed. amount of photons. Fig. II. 10 illustrates transmittance of light through a sample.

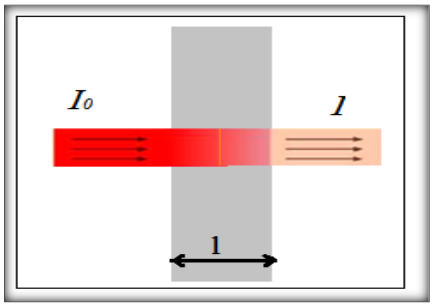

Fig. II. 10: Transmittance of light through a sample.

Intensity of light passing through a sample (I) is measured using UV/Vis spectrophotometer and compared to the intensity of light before it passes through the sample (I_0). Those values expressed in absorbance (A) or transmittance (T) [45]. The spectrophotometer is consists of monochromator type with a tungsten source for producing visible and near inrared radiation (Fig.II.11). Divided primary beam into two ones via

wavelength selector; one is directed to the sample while the other passes through a blank control (substrate). The split beams travel equal path lengths to reach detectors then a digital meter compares the intensity of the two beams and calculates a transmittance for the film with respect to the substrate. as the comparison between the sample and reference beams is made, the value of transmittance is determined by the apparatus [46].

In this study, used UV-Vis spectrophotometer is UV–VIS spectrophotometer Shimadzu, Model 1800, which allowed getting an optical transmittance spectrum of hematite thin film in the wavelength range from 300 to 900 nm. Use of this data can lead to calculate: **absorption coefficient, band gap and Urbach energies.**

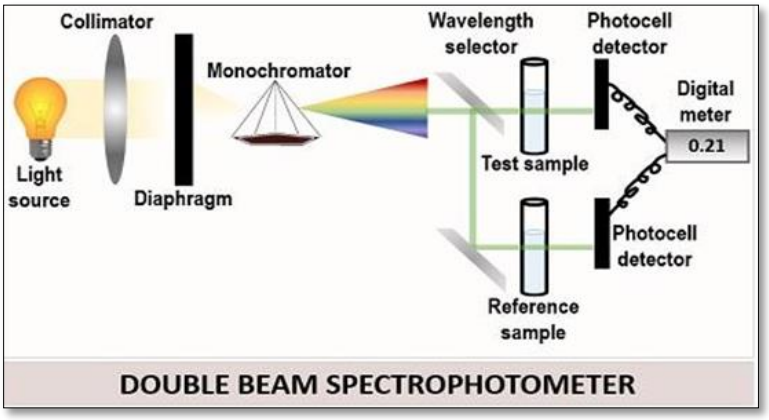

Fig. II. 11: Simplified schematic diagram of double beam spectrometer

II. 4. 3. 2.The absorption coefficient (Abs.Coe):

The Abs.Coe α of hematite thin films was deduced with the help of transmittance measurements. The films' Abs.Coe was estimatedd using the following expression [47]:

$$T = e^{-\alpha d} \qquad \text{(II. 12)}$$

$$\alpha = -\frac{1}{d} ln(T) \qquad \text{(II. 13)}$$

where T is the normalized transmittance and d is the film thickness.

II. 4. 3. 3. Band gap energy:

The band gap optical energy E_g of α-Fe_2O_3 thin films was estimated using the Tauc's relationship as follows [48]:

$$\alpha h\nu = A(h\nu - E_g)^{n} \qquad \text{(II. 14)}$$

where α, *hν*, and E_g are the absorption Coe, the photon, and gap energies, respectively. *A* is a constant and *n* is taken 2 based on the consideration that α-Fe_2O_3 has an indirect band gap [49].

II. 4. 3. 4. Urbach energy:

The optical absorption spectra of semiconducting materials have an significant role since they offer the fundamental information about its composition and their E_g. In general optical absorption spectra of the semiconductor can be split into 3 most important regions:

- Weak absorption region, that occurs from impurities and defects;
- Absorption edge region, that occurs because of disorder of the system and structural perturbation;
- Strong absorption region, that estimates the E_g.. Along the Abs. Coe α curve and near the optical band edge there is an exponential part called Urbach tail, Which express the disorder in the structure and localized states which extended E_g. [50-52]. In the low energy range of photon, Urbach empirical rule depending on the absorption coefficient α and photon energy $h\nu$ is known as, the following equation [53]:

$$\boldsymbol{\alpha = \alpha_0 e^{h\nu/E_u}} \qquad \text{(II .15)}$$

where α_0 and E_u are constant and the energy tail which sometimes is called Urbach energy. E_u is weakly dependent upon temperature, the localized states and disordered or low crystalline materials [54]. Taking the logarithm of the two terms of equation (II. 15) which leads to a straight line equation as follows:

$$\boldsymbol{ln\,\alpha = ln\,\alpha_0 + (h\nu/E_u)} \qquad \text{(II .16)}$$

E_u can be obtained from the slope of the straight line of plotting ln (α) as function of incident (hν).

II. 4. 4 Fourier transforms infra‑red (FTIR) spectroscopy

The IR can be split into three spectral subregions; the near, the mid, and the far extending in the ranges: (800 to 2500 nm (NIR)), (2500 to 15000 nm (MIR)), and (15,000 to 100,000 nm (FIR)) respectively. The most ordinary kind of IR instrument is the Fourier transform infrared (FTIR) spectrometer owing to its high signal-to-noise ratio, easy to use, and relatively low cost.

FTIR spectroscopy is an analytical attitude used in laboratories to investigate the structure of elaborated products.. IR photons energy is not sufficient to cause transition of the

valence electrons; however, the rotational and vibration motions are excited in molecules by IR radiation. Vibration energy bonds absorb the infrared light at precise frequencies linked to functional groups present in the main product. A characteristic absorption bands is formed, the intensity and position of these absorption bands give a fingerprint of molecular structure of the product making FTIR a highly useful and adjustable spectroscopic technique.

Fig. II. 12 illustrates the standard process of an FTIR. As shown, the FTIR is like a Michelson interferometer with the only one variation that one of the mirrors is mobile and is well managed by a motor, this make the time delay between the reflected beams off the two mirrors variable. The specimen is situated in front of the detector where the interferogram is recorded. The interferogram data are not useful as it is; though its Fourier Transform tells information about the spectral response of the specimen [55].

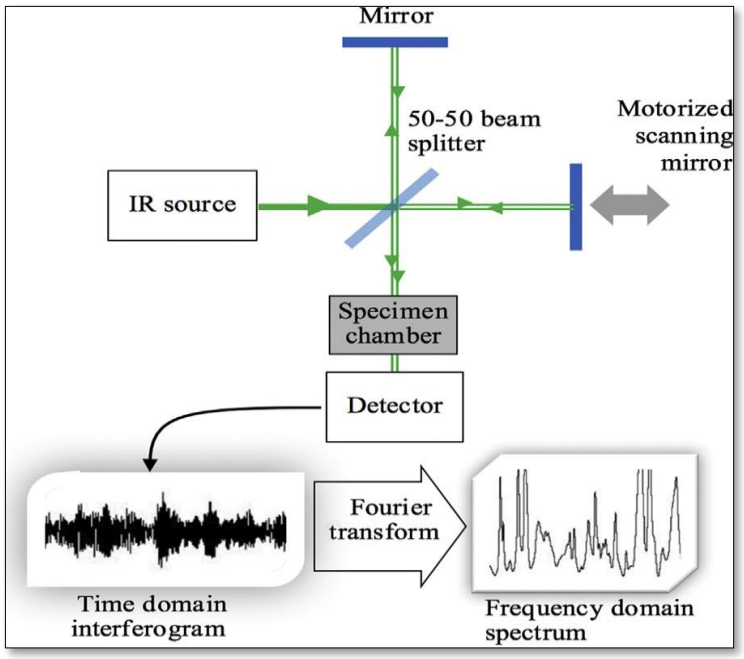

Fig. II. 12 The basic configuration of the FTIR spectrometer [55].

Conclusion

Iron oxides nanomaterials synthesizing can be made through several methods, which can be normally categorized as biological, physical, and chemical manner, in physical methods, size of particles could not be controlled in the range of nanometer; for this reason, Spray pyrolysis with moving nozzle which is a chemical process is the main used method for synthesizing our thin films to maintain the heat of substrate through the elaborating duration. The properties of the spray deposited films are defined basically by the growth conditions

throughout their deposition. A lot of factors can influence the growth mechanism and adapt the films structure such as Core Temperature, Atomizing Air Pressure, Nozzle to Substrate Distance, and Substrate Temperature. characterization tools such as XRD, UV-Vis, SEM, and FTIR have been discussed for investigating the structural, optical analysis, morphological with the help of them.

References

[1] Perednis, Dainius, and Ludwig J. Gauckler. Journal of electroceramics 14 (2005): 103-111.

[2] Cuenya BR. Thin Solid Films.;518 (2010): 3127–3150.

[3] Wu, Wei, Quanguo He, and Changzhong Jiang. Nanoscale research letters 3 (2008): 397-415.

[4] W.A. Bryant, J. Mater. Sci., 12 (1977) 1285.

[5] R.N. Ghoshtagore, J. Electrochem. Soc, 125 (1978):110.

[6] T. Suntola, Thin Solid Films, 216 (1992): 84.

[7] R.R. Chamberlin and J.S. Skarman, J. Electrochem. Soc, 113 (1966): 86.

[8] C.J. Brinker, A.J. Hurd, G.C. Frye, K.J. Ward, and C.S. Ashley,J. Non-Cryst. Solids, 121 (1990): 294.

[9] Chen, C. C., M. M. Nasrallah, and H. U. Anderson. Journal of the Electrochemical Society, 140 (1993): 3555-3560.

[10] C.J. Brinker, G.C. Frye, A.J. Hurd, and C.S. Ashley, Thin Solid Films, 201 (1991): 97.

[11] . Wu S, Sun A, Zhai F, et al. Mat Lett.;65 (2011):1882–1884.

[12] Laurent S, Forge D, Port M, et al. Chem Rev;108 (2008): 2064–2110.

[13] Çalışkan, Gülizar, et al. International Conference on Medical and Biological Engineering. Springer, Cham, 2019.

[14] Ali, Attarad, et al. Nanotechnology, science and applications 9 (2016): 49.

[15] Thanh, Nguyen TK. CRC press, 2012.

[16] Schwertmann, Udo, and Rochelle M. Cornell. John Wiley & Sons, 2008.

[17] Sugimoto, Tadao, and EgonMatijević. Journal of Colloid and Interface Science 74 (1980): 227-243.

[18] Tronc, E., et al. Hyperfine Interactions 95 (1995): 129-148.

[19] Joekes, Inés, et al. Journal of Colloid and Interface Science 84 (1981): 278-280.

[20] Morris, Richard V., et al. Journal of Geophysical Research: Solid Earth 94 (1989): 2760-2778.

[21] Chanéac, C., E. Tronc, and J. P. Jolivet. Nanostructured Materials 6.5 (1995): 715-718.

[22] Ennas, Guido, et al. Chemistry of Materials 10 (1998): 495-502.

[23] Johnston, James H., and David G. Lewis. Springer, Boston, MA, 1986. 565-583.

[24] Bottero, Jean Yves, et al. Langmuir 10 (1994): 316-319.

[25] Schwertmann, Udo, Josef Friedl, and Helge Stanjek. Journal of colloid and interface science 209 (1999): 215-223.

[26] Feitknecht, W. " Z. Elektrochem 63 (1959): 34-43.

[27] Blgham, J. M., et al. GeochimicaetCosmochimicaActa 54 (1990): 2743-2758.

[28] Mooney, John B., and Shirley B. Radding. Annual review of materials science 12 (1982): 81-101.

[29] A.R. Balkenende, A. Bogaerts, J.J. Scholtz, R.R.M. Tijburg, and H.X. Willems, Philips Journal of Research, 50 (1996): 365.

[30] S.P.S. Arya and H.E. Hintermann, Thin Solid Films, 193 (1990): 841.

[31]C.H. Chen, E.M.Kelder, P.J.J.M. van der Put, and J. Schoonman, J. Mater. Chem., 6 (1996): 765.

[32]Malik, Oleksandr, Francisco Javier De La Hidalga-Wade, and Raquel Ramírez Amador. Pyrolysis (2017): 197

[33]Kelly, A. J. Aerosol Science and Technology 12 (1990): 526-537.

[34]Filipovic, Lado, et al. Proceedings of the world congress on engineering. Vol.2, 2013.

[35]Perednis, Dainius. Diss. ETH Zurich, 2003.

[36] Lenggoro, I. Wuled, et al. Journal of Materials Research 15 (2000): 733-743.

[37] Perednis, D., and L. J. Gauckler. Solid state ionics 166 (2004): 229-239.

[38] Siefert, W. Thin solid films 120 (1984): 275-282.

[39] P.S. Shewale, Synthesis of Zno Thin Films by Advanced Spray Pyrolysis Technique and their Use in Gas Sensor. (2012).

[40]P. N. Gibson, Thin Films: Characterization by X-Rays, Article review, MaterialsScience and Materials Engineering, (2016).

[41] A. Guinier, X-ray Diffraction , Freeman, San Francisco, (1963).

[42]Glazer, Anthony Michael. A Journey Into Reciprocal Space: A Crystallographer's Perspective. Morgan & Claypool Publishers, (2017).

[43] Zhou, Weilie, and Zhong Lin Wang, eds. Springer science & business media, (2007).

[44]Micheletti, F. B., & Mark, P. Applied Physics Letters, 10 (1967): 136-138.

[45]F. M. Sanda, M. E. Victor, T. A. Monica, C. Alina, University of Oradea Romania, (2012).

[46]Fiddes, A. J. C. Deposition of zinc oxide by spray pyrolysis (1993).

[49]M. M. Almotari, Fabrication and Characterisation of Zinc Oxide Thin Films Singly Doped With Trace amounts of Rare Earth Materials, (2013).

[47]Hafdallah, A., Yanineb, F., Aida, M. S., &Attaf, N. Journal of Alloys and Compounds, 509 (2011): 7267-7270.

[48] J. Tauc, R. Grigorovici, A. Vancu, physica status solidi (b), 15 (1966): 627-637.

[49] J. Desai, H. Pathan, S.-K. Min, K.-D. Jung, O.-S. Joo, Applied surface science, 252 (2006): 2251-2258.

[50]Melsheimer, J., & Ziegler, D. Thin Solid Films, 129 (1985): 35-47.

[51]Ikhmayies, S. J., & Ahmad-Bitar, R. N. Journal of Materials Research and Technology, 2 (2013): 221-227.

[52]Aly, K. A., AbdElnaeim, A. M., Uosif, M. A. M., & Abdel-Rahim, O. Physica B: Condensed Matter, 406 (2011): 4227-4232.

[53] Urbach, F. Physical Review, 92 (1953): 1324.

[54] Hassanien, A. S., and Alaa A. Akl. Superlattices and Microstructures 89 (2016): 153-169.

[55] Omidi, Meisam, et al.. Wood head Publishing, (2017): 97-115.

CHAPTER III:

PHOTOCATALYTIC DEGRADATION OF METHYLENE BLUE DYE BY COBALT DOPED HEMATITE THIN FILMS UNDER UV AND SUNLIGHT IRRADIATION

III.1. Preview on Photocatalysis

Early in 1901, Giacomo Ciamician was one of the first chemist who conducted experiments to study if light alone would allow chemical reactions [1], He did experiments with blue and red lights and establish that a chemical effect happened only in blue light. He was vigilant to exclude the likelihood that these reactions were not powered by thermal heating powered by light. Ten years after, the keyword photo-catalysis emerged in scientific literatures [2] Scientists took account that ZnO causes Prussian blue bleaching beneath illumination photocatalysis. Subsequent experiments of using ZnO as a photocatalyst have inspired for other reactions such as the reduction of silver ion under illumination in 1924 [3]. Although photosensitive reactions had been long discovered prior to these efforts, those procedures did not engage a light-sensitive catalyst [4]. Afterward, it was reported that TiO_2 and Nb_2O_5 drive photocatalytic reduction of Ag^+ in nitrate of silver ($AgNO_3$) to Ag and Au^{3+} in $AuCl_3$ to Au in 1932 [5]. After that, $TiO_2$was investigated as a photo sensitizer to remove the color dyes in the attendance of O_2 [6]. Yet, interests in photo catalysis remained a fad because of the absence of matter-of-fact applications. Early on 1970s, such situations changed for two reasons. First, the "oil crisis" encouraged scientists to seek alternative energy provisions to fossil fuels second, the concerns over environmental impacts by important industrial operations goaded researchers to look for renewable energy sources. Quite a lot of papers were published during this average time. In 1968, scientists from the Bell Lab primary reported O_2 evolution on TiO_2 [7]. In 1972, photo-assisted H_2O oxidation with H_2 production using TiO_2 electrodes within UV light illumination was reported [8]. Photocatalytic water splitting only under light yielding H_2 and O_2 under argon in 2:1 stoichiometric ratio was reported in 1977 [9]. Through the same time of studies, Decomposition of CN^- and SO_3^{2-} by TiO_2, ZnO, and CdS under light were by Frank and Bard [10]. Later in 1979, Fujishima et al. [11] reported studies on photocatalytic CO_2 reduction using various non organic semiconductors as photocatalysts. Photocatalysis applications made significant research attention in the 1980's to similar reactions using TiO_2 nanoparticles as the main agent in photocatalysts [12]. Since then, augmenting the photocatalytic efficiencies, looking for new photocatalysts, and expanding the extent of the reactions, examinations have been focused on understanding the basic principles. For instance, photo make super-hydrophilicity cause was revealed on TiO_2 in 1997 [13]. Result to this, TiO_2 with self-cleaning and anti-fogging functionalities has been used to constructed materials [14].

Higher photocatalytic activities than of TiO_2 have been studied to increase new photocatalysts, under UV lights [15] For higher efficiencies, under visible light photo catalysts have been practiced in parallel [16]. In the meantime, further learning about the governing principles of photocatalysis was gradually taken by researchers.

III. 2. Broad definition of Photocatalysis

Photocatalysis word is composed of Photo and catalysis. The prefix photo means light and Catalysis is the process in which a matter participates in altering the rate of a chemical transformation of the reactants without being altered itself. The photocatalyst is a strange method which can be used for a purposes variety like degradation of different organic pollutants in wastewater, hydrogen production, air purification, and antibacterial activity. Lately, the photocatalytic process is attaining more concentration from wastewater to obtain complete mineralization of the pollutant accomplished under offhand conditions of temperature and pressure. The notable features of these processes comprise undisposed of waste and cost-effectiveness while sunlight or near-UV light can be employed as a supply of illumination. Photocatalyst means photon assisted production of catalytically active species. In general, Photocatalysis is "a change in the rate of chemical reactions or their generation under the act of light within substances presence called photocatalyst that absorbs quanta of light and takes part in the chemical transformations of the reactants" [17].

III. 3. Photocatalytic mechanism

Photocatalysis, in terms of reactions and mechanisms, may be explained by four important steps:

•When energy of falling photons (hv) on the surface of a semiconductor is equivalent or more than the band gap energy of the latter; as a result of light irradiation, Electrons excitation from the valence band (VB) to the conduction band (CB) of the semiconductor happens letting holes in VB (i.e hv generates electron-hole (e^- and h^+) at the surface of semiconductor).

•Holes left in VB of the semiconductor can oxidize donor molecules and react with water molecules to engender hydroxyl radicals OH^- which have strong oxidizing power to degrade pollutants.

•The CB electrons react with O_2 as dissolved oxygen species to form superoxide ions $O_2^{\bullet-}$. These electrons induce Red Ox reactions as: $e^- + O_2 \rightarrow O_2^{\bullet-}$.

These (e^- and h^+) could undergo successive oxidation and reduction reactions with any species, which might be adsorbed on the surface of the semiconductor to provide the required products [18-19].

Fig. III. 1 shows photocatalytic reaction process, where O: chemicals in oxidative reactions, R: chemicals in reductive reactions, (I) Generation of e^- and h^+ after light absorption, (II) Excited charges separation, (III) e^- and h^+transfer to the surface of photocatalysts, (III′) e^- and h^+recombination, and (IV) Charges utilization on the surface for Red Ox reactions: (e^- + R $\rightarrow R^-$ and $.h^+ + O \rightarrow O^+$).

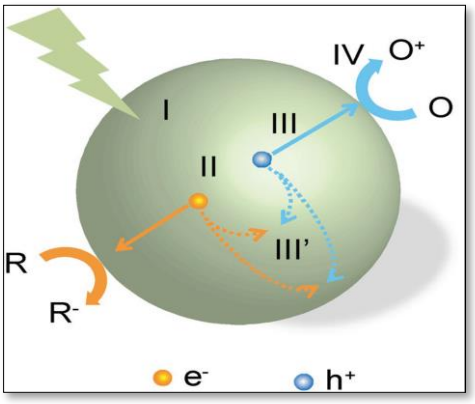

Fig.III.1: Steps in photocatalytic reaction process [20].

III. 3. 1. Description of Oxidation mechanism

Water contained in photocatalyst surface is mentioned as "absorbed water." Holes created in VB oxidize this absorbed water and make way for the formation of hydroxyl ($OH^{\bullet-}$) radicals as strong oxidative agent. Afterward, these hydroxyl radicals act in response with organic dyes matter. With oxygen presence when this process happens, radical chain reactions consume oxygen in some cases and create intermediate radicals in the organic compounds along with the oxygen molecules. As result to this, the organic matter finally decomposes eventually becoming carbon dioxide and water [18, 21] which leads to an oxidative decomposition [17]. Fig. III. 2 shows the complete oxidation processes.

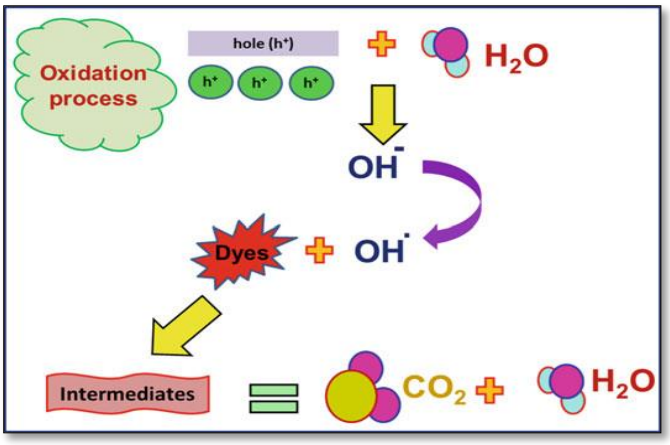

Fig. III. 2: Schematic representation of oxidation mechanism [17].

III. 3. 2. Description of Reduction mechanism

Fig. III. 3 represents the reduction process, the reduction of oxygen enclosed in the air takes place as a coupling reaction. Reduction of oxygen occurs as an alternative to hydrogen generation hence oxygen is a simply reducible substance. Electrons in CB react with melt oxygen types to form superoxide anions (O_2^-). The latter connect to the intermediate products in the oxidative reaction, producing peroxide or changing to hydrogen peroxide (H_2O_2) and subsequently to water. The reduction has tendency to happen more easily in organic matter than in water. So, organic matter with higher concentration tends to increase the number of positive holes which reduces the recombination of carriers and improves the photocatalytic activity [21, 22].

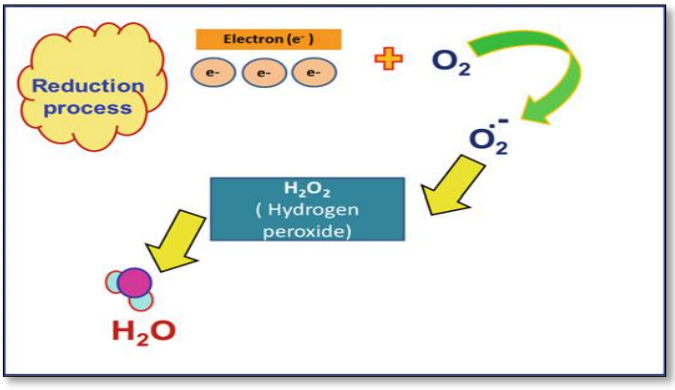

Fig.III.3: Schematic representation of reduction mechanism [17].

III. 4. Photocatalytic Oxidation of Organic dyes

Recently, about 12–20% of artificial dyes have been often used in textile industries to color products as cotton, woolen and polyamide fibers. The unprocessed dyes are frequently discharged into the environment due to incomplete use. A dramatic source of water pollution and troubling of aquatic life can be caused by discharge of those dyes in the environment. Most of these dyes are probably carcinogenic in human, whilst some others could slow down light penetration into streams affecting the photosynthetic process. So, dyes removal from water has received increasing thought. Organics decomposition of harmful dyes to human and the environment is inspired as purpose of photocatalysis. In consideration to make visible light photocatalysis, organic dyes can be a judicial selected for photocatalysts. As advantages, organic dyes have little toxicity; low price and can competently work in aqueous media. Several organic compounds that have effectively been decomposed into CO_2 and risk-free minerals by photocatalysis are phenols, halo phenols, alkanes, haloalkanes, cresols, aromatics, alcohols, polymers, dyes, herbicides, pesticides, bacteria, viruses, fungi, molds, cancer cells, highly resistant spores and surfactants. Approximately, decomposition of organic compounds has the same basic mechanisms with few variations exist in the photocatalyst characteristics that are grave to the reaction such as the number and force of surface acid sites and the Red Ox potentials of the photocatalyst relative to reaction of the organic and inorganic species to be removed.

Most photocatalysts can be made in powder or thin film formations. Although the preparation methods and lots of properties differ among the two formations, each of them is useful to decomposing organic degradants. Films have the advantage of avoiding catalyst filtering processes necessary after complete photocatalytic reaction, and are therefore beneficial in applications such as bacteria destruction and water purification [23]. Also, films have the possibility to be re-used after rinsing.

III.5 Band Edge Positions

In a semiconductor, the difference in energy between VB and CB is called the band gap. Band data positions are useful when creating and analyzing semiconductor photo catalysts because they indicate the photoreactions thermodynamic limitations that can be achieved by the free carriers. For instance, if the oxidation of an organic compound is desired, then VB edge of the semiconductor must be well positioned relative to the organic compound oxidation potential. On the other hand, if the reduction of O_2 molecule is required, then the CB edge of the semiconductor must be situated favorably relative to the O_2 molecule reduction potential. Fig. III. 4 shows the VB-CB band-edge positions of numerous dominant photo catalysts in relation to the H_2O oxidation and reduction potentials [17].

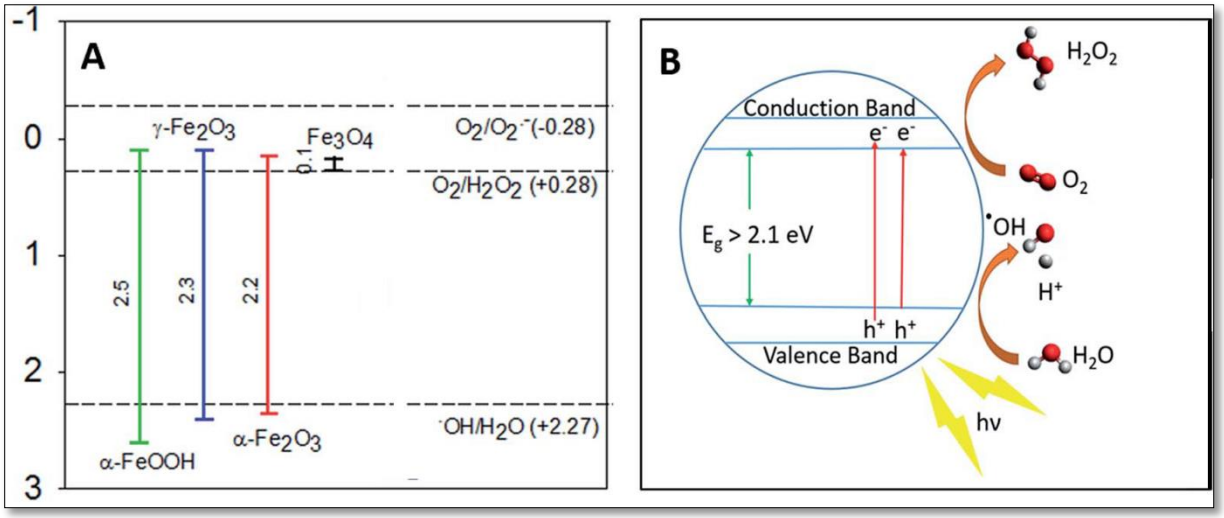

Fig. III. 4: Band-gaps and Red Ox potentials, compared with redox potentials of hydroxyl, peroxide and superoxide radicals, (the redox potentials described here are compiled from the work of Liu, Fujishima et al., and Sherman)

III.6. Influence of operational parameters

The presence of a appropriate photocatalyst can work in visible/solar light is the original step, the next one is to examine optimum prepared factors so as to take the research to an realization level. in fact, as a photocatalyst is utilized to treat an industrial effluent, specific factors must be optimally altered so as to attain high efficiency. a number of connected studies have been carried out and diverse review and research articles are offered in literature [24-28]. The apprized results propose that apart from the photocatalyst type utilized, photodegradation also corresponds on the type of substrate, light intensity , concentration, preparation method of the catalyst, its calcination temperature, amount and type of dopant(s), etc. An outstanding study on the different factors affecting the Photocatalysis behavior was indicated by Zhou et al[29].

III. 6 .1 Crystal Structure, Shape, Size, and Surface Area of Catalyst

Catalyst structure plays a key role in implementing higher activity of photocatalytic process. NMs with smaller size and large surface area can successfully show higher competence in the Photocatalytic process. Morphology also affects the final degradation

competence or efficiency, Saravanan et al. stated that ZnO samples with spherical shap which have large surface area show higher competence compared with rod-and spindle-shaped ones.[30]. When the size of the catalyst is reduced, an accumulation of atoms occurred on the surface of the catalyst, this increase the ratio of surface /volume, demonstrating the significance behavior of nano metric dimension instead of bulk products. This possession improves the transfer rates of active sites and interfacial charge carrier which leads to higher catalytic efficiency [31]. Also, it is well known that the redox reaction of photocatalytic process happen on the photocatalysts surface and then the surface properties mainly affect the efficiency of catalyst [18, 30].

III. 6. 2. Intensity of light

Light intensity affects the rate of formation of (e-/h+) pairs. An increase in the intensity leads to higher rate and of pairs then to photocatalysis rate. However, with amplify in light intensity beyond an optimum, the rate of photogeneration of e^- and h^+ becomes more than the rate of the subsequent Red Ox reactions. Photogeneration rate is then no longer the controlling step and hence it gradually becomes less reliant on the intensity of light. It has been found that at low intensities the rate of reaction is first order and at high intensities it becomes half order and ultimately becomes independent when extreme high irradiation is applied [32]. Such behavior may be ameliorated with doping trough several mechanisms as reported bellow.

III. 6. 3. Pollutant and its concentration

Rate of photodegradation depends on the varied chemical substituent groups attached to substrate composition. The primary concentration of the pollutant also plays a significant role in the main process. Efficiency of the photodegradation reduces as the primary concentration augments due to two main causes

- high concentration pollutant absorbs more light than the photocatalyst itself which tend to have an inhibitive effect on the degradation
- increasing in pollutant concentration augments the equilibrium, adsorption and hence competes with adsorption of OH^- on the same site [33].

III. 6. 4. Dopant

Doping with metal ion can adapt the properties of the surface area of the catalyst and hence can be utilized to improve its activity. selection of an appropriate catalyst with-chosen dopant augments the overall photoreactivity by enhancing the interfacial charge transfer process, inhibiting recombination of e^- and h^+.

Transition metals like Ni, Cr, Nb, Fe, Cu, Mn, Co, Ru, Mo, W, Pt and Au ameliorated the photoactivity in the visible range by introducing new energy levels between VB and CB. Noble metals such as Pt, Ag, Pd, and Au raise interfacial moving charge and procure delay in recombination of e^- and h^+ by acting as an e^- trap [33]. W.Vallejo et al. [34] synthesiz ZnO thin films with Cobalt and cupper doping, by the sol–gel process, and establish that the kinetic outcomes of photodegradation of methylene blue MB dye reached 62.6% for Co-ZnO: thin films and 42.5% for Cu-ZnO: versus 2.7% for the non doped ZnO. Chen, Wiqiang, et al. [35] showed that doped IONMs with Nickel and Cobalt (Ni-Fe_2O_3 and Co -Fe_2O_3) could be practical as adsorbent candidates for heavy metal ions elimination in actual ecological purification. It is worth noting that high methylene blue photodegradation is still needs investigations with others products such as Fe_2O_3 NPs under thin films states which avoids catalyst filtering processes.

III.7. Co doped Iron oxide thin films (Co-α-Fe_2O_3) for Photocatalytic degradation of methylene blue dye.

Iron oxide thin filmscan be a good photocatalyst absorbing visible light,α-Fe_2O_3 with band-gap of 2.2 eV is an interesting n-type semiconducting material and a suitable candidate for photodegradation under visible light condition[36]. The good performance of photocatalytic can be due to significant produce of e^- and h^+ pairs through illumination of the band-gap (Eq.III.1) [37].

$$Fe_2O_3 + h\nu \longrightarrow Fe_2O_3(e^-_{cb}, h^+_{vb}) \qquad \text{(III.1)}$$

The proposed photocatalytic procedure of MB dye by hematite (α-Fe_2O_3), under visible light is illustrated in Fig. III.5.

Under light, electrons in the VB transferred to the CB of the iron oxide, with a simultaneous creation of the same quantity of holes in the VB, which lead to electron–hole pair

generation. **Redox reactions** with organic pollutant (MB) happened as a result of the presences of produced carrier charges on the surface of catalyst. Direct oxidation of MB to reactive intermediates is occurred because of the elevated oxidative potential of hole (h^+) at VB.

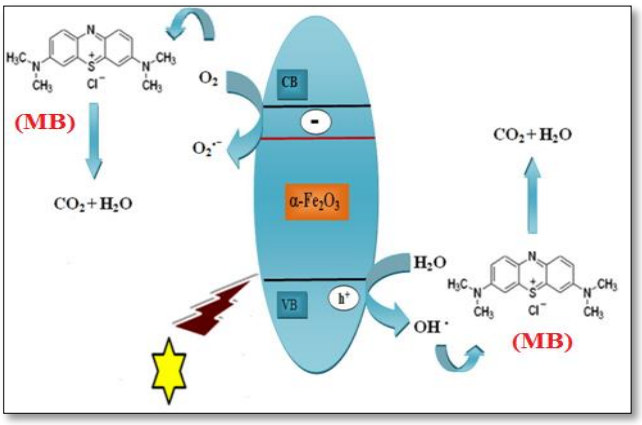

Fig.III.5: Schematic illustration of the photocatalytic mechanism of (MB) using α-Fe_2O_3thin films under visible light[38].

High reactive radicals of hydroxyl can be created by the water decomposition, dissolved oxygen molecules react with electrons forming superoxide radical anions, O_2^-, this giving rise to form hydroperoxyl radicals HO_2 on protonation and finally OH·radicals will be more efficient [38].

$$\alpha - Fe_2O_3 + h\nu \rightarrow \alpha - Fe_2O_3 + e^- + h^+$$

$$h^+ + MB \rightarrow MB^{\cdot+}$$

$$O_2 + e^- \rightarrow O_2^-$$

$$O_2^- + H_2O \rightarrow HO_2^{\cdot} + OH^{\cdot-}$$

$$HO_2^{\cdot} + H_2O \rightarrow OH^{\cdot} + H_2O_2$$

III.7.1. Experimental details

III.7.1.1.Thin films preparation

Cobalt doped iron oxide NPs were prepared using SPMN method (Fig.II.6).To get the primer solution with concentration of 0.5M of Fe^{+3}, 1.622g of iron chloride ($FeCl_3$) was

dissolved in 20mL of distilled water and ethanol mixture in volume ratio 1:1 and stirred vigorously until complete dissolution (red brownish solution).

Different dopant concentrations (0.25, 0.5, 1, and 1.5 wt %) were obtained by adding different quantities of cobalt chloride $CoCl_2$ (rose color as seen in Fig. III.7) to primer solutions with keep stirring for 30 min.

Fig. III.6: Cobalt chloride ($CoCl_2$).

To determine the required weight ratios of cobalt, the following relationship was established:

$$\frac{m_{Co}}{m_{Fe}} = wt\,\% \qquad \text{(III.2)}$$

The mass of cobalt chlorine ($CoCl_2$) can be found through the relationship:

$$\frac{m_{Co}}{M_{Co}} = \frac{m_{CoCl_2}}{M_{CoCl_2}} \qquad \text{(III.3)}$$

Table III.1 summarizes the different percentages of cobalt chlorinewight in respect to the following ratios (0, 0.25, 0.5, 1, 1.5)%.

Table III. 1**:** Summarizes the different percentages of cobalt doping weight at different ratios.

(Co/Fe)%	**0**	***0.25***	***0.5***	**1**	***1.5***
m ($CoCl_2$) (g)	**0**	**0.0055**	**0.01127**	**0.02254**	**0.03304**

The obtained blends were sprayed onto 500°C heated glass substrates (Ref 217102: having 7.5x2.5x0.13cm^3 as dimensions). The spray rate and time of deposition are 5ml/min and 3min respectively. The distance between nozzle and substrate is kept at 5cm. The prepared slides were annealed for two hours at 550°C.

III.7.1.2.Thin films characterization

The crystallographic structure of 0-1.5 wt. % Co-doped α-Fe_2O_3 thin films have been examined via a Philips X-ray diffractometer model PW-1710 operating with (λ = 1.5406 Å for Cu-Kα radiation). Optical properties such as transmittance and band gaps have been undergone through the optical transmittance spectrum using (UV–VIS spectrophotometer Shimadzu, Model 1800) working in 300-900nm wavelength range. Whereas FT-IR analysis was performed, in 400-4000cm^{-1}range, by use of Shimadzu IR-Infinity 1 apparatus. All the measurements were carried out at room temperature (rt).

III.7.1.3. Photocatalytic experiment

photodegradation by catalyst occurs when catalyst is illuminated with light of energy exceeds the band gap energy. In this study, Photocatalytic efficiency was defined by the degradation of MB dye using Ultra Violet and sun light as energy sources for electrons excitation from filled valence band to empty conduction band of cobalt doped iron oxide thin films. In presence of light The oxygen dissolves in water containing the photo-catalyst, and then decomposes the organic species to CO_2 and H_2O [39].

In order to prove the effect of photocatalysis, solution of (MB) dye were prepared at concentrations of 1 ppm, the samples of Co doped α-Fe_2O_3 were covered with a 18mm thick layer of MB solution (Fig.III.7).Before lighting, all films were placed in dark about 15 min to bring the films into equilibrium with the dissolved dye. For UV lighting,0.25-1.5 wt.% Co doped films were illuminated with a 300W oriel lamp which was placed at a distance of 20 cm from the sample. Whereas for sun lighting film, 1.5wt.% Co doped thin film was directly placed under sunlight. Change in dye concentration was determined by measuring the absorption spectrum of 1mL aliquots using a UV/vis spectrometer (Shimadzu, Model 1800).

The degradation percentage of MB solution was estimated using the following Eq:

$$\boldsymbol{\Omega = \frac{\delta_0 - \delta_t}{\delta_0} \times 100\%} \qquad \text{(III.4)}$$

whereΩ is the degradation percentage (%),$\delta_0$and δ_t are the initial absorbance and the absorbance at a chosen time interval of MB expressed in mg/L [40].

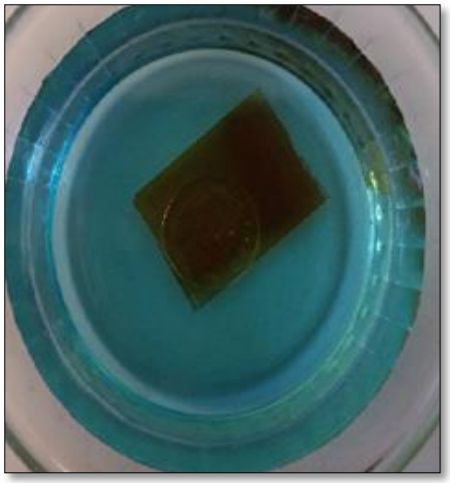

Fig.III.7: Thin films covered by MB solution.

III.7.2. Results and discussions

III.7.2.1 structural properties

The XRD patterns of 0-1.5wt. %Co-doped hematite thin films are presented in Fig.III.8. The observed peaks at 2θ: 24.23°, 33.24°, and 35.70°correspond to lattice plane of (012), (*104*), (*110*) respectively confirm α-Fe_2O_3 formation of rhombohedral crystal structure which much well with its (JCPDS No: 01.073-2234, with space group R-3c number 167).No additional reflections, at limit of detection, due to the related phases of cobalt oxides were observed [41]. This result suggeststhat the dopant (until 1.5 %) is well substituted in theα-Fe_2O_3 lattice, and the rhombohedral structure is not tailored by theaddition of Co^{2+} into the α-Fe_2O_3 matrix. Therefore, the dopants alter the crystallinity but not the crystal structure of α-Fe_2O_3. This result is compatible with literature [42]. It is worth noting that a slight change in peaks intensity which may be related to both (i) grain size due to network defects and (ii) oxygen vacancies, as reported by Lima et al. [43].

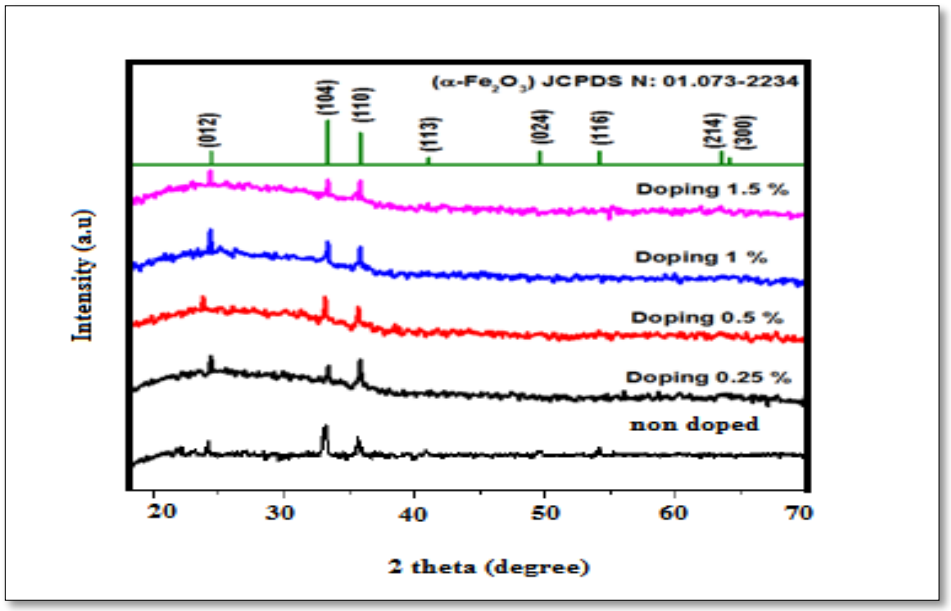

Fig.III.8: X-ray diffraction patterns of sprayed Co-doped hematite thin films.

The lattice constants (*a* and*c*) for the rhombohedral phase structure, are determined by the relations[44]:

$$2d_{hkl}\sin(\theta) = n\lambda \qquad \text{(III.5)}$$

and

$$\frac{1}{d_{hkl}{}^2} = \frac{4}{3a^2}(h^2 + k^2 + hk) + \frac{l^2}{c^2} \qquad \text{(III.6)}$$

where (*hkl*) and 'd_{hkl}' are Miller indices and the inter-planer distance, respectively. The lattice parameters '*a*' and 'c' are listed in Table III.2. It is worth noting that lattice parameters of the standard JCPDS data card, are (a_0 =b_0= 5.0325Å and c_0 = 13.7404Å). Fig.III.9shows lattice parameters up on doping concentration. The two lattices constant initially augment with respect to the doping, then decreases at higher doping concentration. This is in sharp contrast to the results reported in[45,46], which indicated that the lattice constant enhances linearly with the doping. It was informed that the difference might be due to a variety of parameters including deposition process and conditions, valence of Co ions, and position of Co atoms in the α-Fe_2O_3 lattice, and presence of secondary phases. The result of XRD mesurments may be understood as follows: as the ionic radius of Fe^{3+} and Co^{2+} are 0.58Å and 0.67Å respectively (Co ion is larger than iron) [47]; and when the Fe atoms are replaced by Co atoms, an interstitial sites may also be occupied by Cobalt as a result of the deformation of lattice structure [48].

The crystalline sizes of 0.25-1.5wt.% Co doped thin films, given in TableIII.2werecalculated from the three more intense peaks using Scherrer'sformula[49]:

$$D = \frac{0.9\,\lambda}{\beta cos\theta} \qquad \text{(III.7)}$$

where$D$, β, λ, and $\theta$are the crystallite size, the full width at half-maximum (FWHM) of the considered diffraction peak, the X-ray wavelength (1.5406 Å) and Bragg angle, respectively. Fig. III.10shows the average grain size variation. D decreases with doping from 48.54for non doped sample to 32.29nm for0.25 wt.% Co doping one, of course with slight fluctuation for the other values of doping. By increasing the dopant concentration to 0.5 wt.%, the average grainsize increases to 41.7nm. For dopant concentration of 1 wt. %, the average grain size becomes 46.28nm, and decrease to 38.81nm for 1.5 wt.%. Those values take place in photocatalytic activity hence the later is related to the sample's active surface

Table III. 2. The structural parameters of Cobalt doped α-Fe2O3at different doping concentration.

Cobalt Doping concentration	***(hkl)***	***2θ°***	***d_{hkl}*(Å)**	**Lattice parameters (Å)**	**Grain size: D (nm)**
non doped wt. %	***(012)***	**24.240**	**3.67329**	**a= 5.02896 c = 13.7259**	***48.54***
	(104)	**33.230**	**2.69537**		
	(110)	**35.709**	**2.51448**		
0.25	***(012)***	**24.146**	**3.68470**	**a=5.0361 c=13.7344**	**32.29**
	(104)	**33.1970**	**2.69789**		
	(110)	**35.644**	**2.51805**		
0.5	***(012)***	**23.552**	**3.77627**	**a= 5.039 c= 13.838**	**41.70**
	(104)	**32.949**	**2.71759**		
	(110)	**35.499**	**2.52800**		
1	***(012)***	**24.101**	**3.69148**	**a=5.0366 c= 13.7675**	**46.28**
	(104)	**33.145**	**2.70197**		
	(110)	**35.640**	**2.51832**		
1.5	***(012)***	**24.095**	**3.69238**	**a= 5.0361**	**38.81**
	(104)	**33.148**	**2.70173**		
	(110)	**35.647**	**2.51805**	**c= 13.7663**	

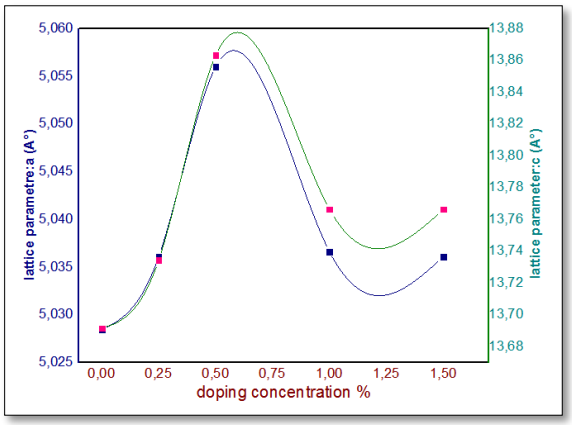

Fig. III.9. Latticeparameters (*a* and *c*) of Cobalt dopedα-Fe_2O_3 thin films upon doping concentrations: 0-1.5.wt%.

.

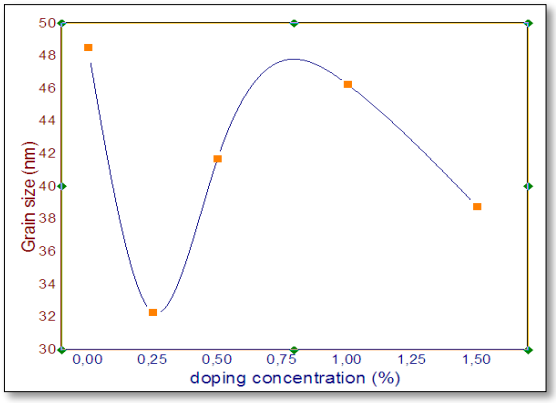

Fig. III.10: Average Grain sizeof Cobalt dopedα-Fe_2O_3 thin films as a function of dopingconcentrations: 0-1.5.wt%.

III.7.2.2 Optical properties

III.7.2.2.1 UV–Vis analysis

Fig.III.11 shows the transmittance spectra of Cobalt doped α-Fe_2O_3 upondoping concentration0.25-1.5wt.%. All samples have good transmittance of about 88% in the wavelengthgreater than 650nm.A high-quality band-band absorption in the UV region, which is used in estimation of gap energy values.

The band gaphas been deducedusing Tauc's relation[50] as follow:

$$\alpha h\nu = A(h\nu - E_g)n \qquad \text{(III.8)}$$

where α, *h ν,* and E_g are the absorption parameter, energy of photon, and gap energy, respectively. *A* is a constant and *n* is 2 related to the fact that α-Fe_2O_3 has an indirect gap [51, 52]. The optical absorption data was used to plot $(\alpha h\nu)^2$ vs *hν*, as shown in Fig.III.12, the straight line extrapolation leads to the band gap energy values of 0-1.5 wt .% Co doped samples.The gap energy of non doped sample was 2.07 eV, this value increases to be in the range 2.09-2.14 eV for the doped samples.

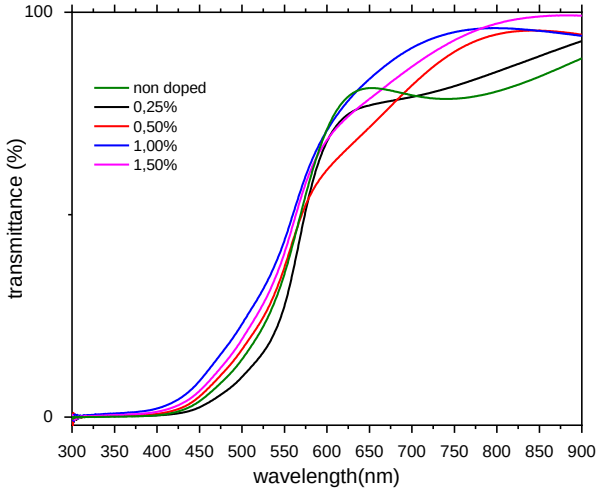

Fig.III.11: Transparency spectra of (0-1.5wt. %) Co-doped α-Fe_2O_3 thin films.

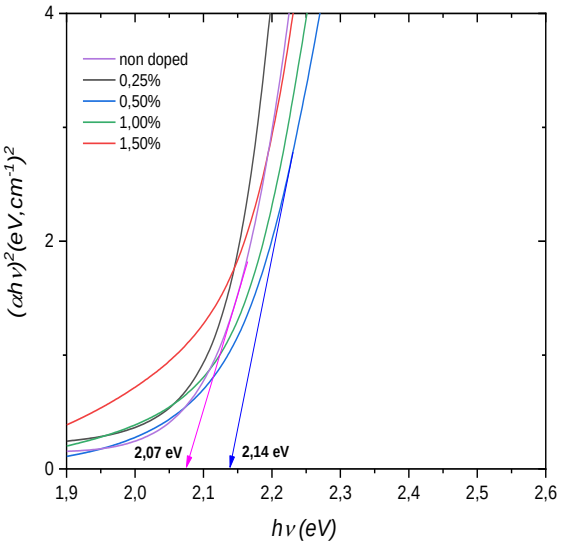

Fig.III.12 Estimated band gap (E_g) from Tauc's relation for 0-1.5%wt Co doped α-Fe_2O_3 thin films.

III.7.2.2.2 FTIR analysis

Fig. III. 13 shows the FTIR spectra of the Co-doped α-Fe_2O_3 thin films upon doping concentration. The peaks in the range 460-563cm^{-1} were attributed to the Fe-O and Co-O stretching mode [53]. Bending vibration of C-O-C functional group was showed in the region (1019‑1123 cm-1) [40]. The peak at 1630 cm−1 is assigned to the bending vibrations of the hydroxyl groups and/or water molecules [54]. The broad band centered around 3400 cm-1 may be referred to lattice water, OH bending vibration of the adsorbed water molecules and to stretching vibrations of the hydroxyl groups, it is clear from the FTIR spectra that the existence of doping Co enhances the hydroxyl combination on the surface of Fe_2O_3, the same result was found by literature [35]. Which is considered ashole (h^+)trapping site on the metal oxide surface, leading to hydroxyl radical which is most powerful oxidants for organic dyes.

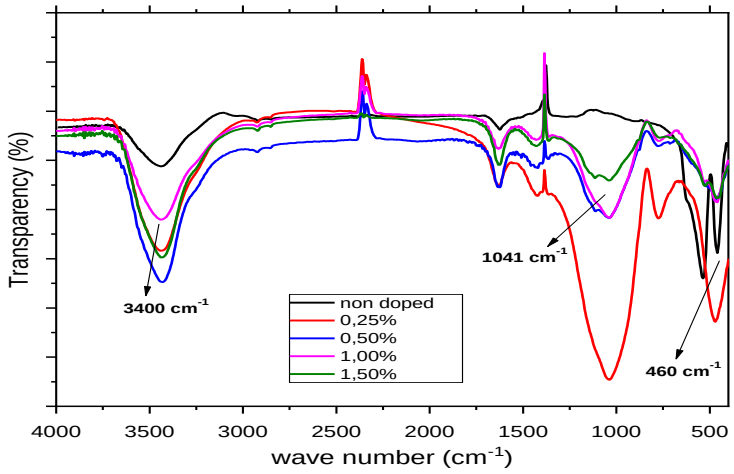

Fig. III. 13. FTIR spectrum of pure and Co-doped α-Fe_2O_3 thin films.

III.7.3 Photocatalytic activity of Co-doped α-Fe_2O_3 thin films

MB has one main band in the visible range with a maximum absorption at 664nm and a small shoulder at 610nm due to the dye dimer. also MB dye color is associated with its auxochrome groups (N-containing groups with one pair electrons on benzene ring) and chromophoric (N–S conjugated system on central aromatic heterocycle). The capability of cobalt doped hematite thin films (Co-α-Fe_2O_3) to degrade MB dye will be estimated throughout its use in photocatalytic under different conditions in this study. such as dark, UV and sunlight irradiation

III.7.3.1 Photodegradation of MB dye under dark condition

Under dark when no excitation of samples will be happened, there is a weak activity of the samples toward MB dye for instance 1.5 wt.% Co doped sample, just only percentage of 16% of MB degradation as shown in Fig. III. 15. This feeble activity may refer to only presence of OH functional group on the sample surface (see Fig. III. 13), as reported by the mechanism suggested by Houas et al. [55]

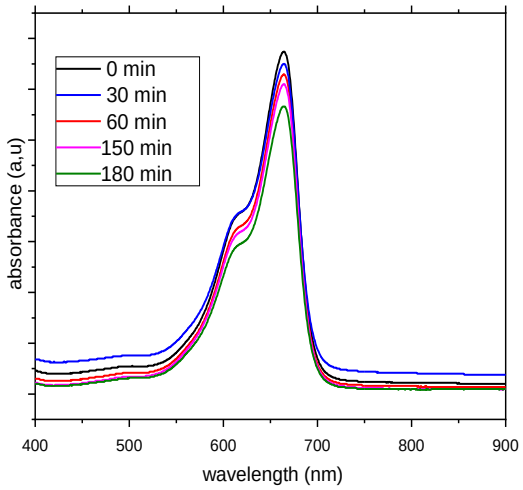

Fig. III. 15 Time-dependent absorption spectra for MB dye in the presence of 1.5% cobalt doped hematite thin films in dark.

III. 7. 3. 2 Photodegradation of MB dye under UV condition

The characteristic intensity of peak absorption decreased through time for UV source as it shown in Fig. III. 16 (a, b, and c). It is clear that all samples have evident Photocatalytic activities under UV light with limitation after certain period of time. It is worth noting that the non doped has weaker effect on MB degradation, but the one doped with 1.5 wt. % is the best until 120min, (spectrum of 120 min is superposes with the one of 150 and 180 min) as shown in Fig. III. 16 (d). It means saturation of MB degradation. Such saturation in photocatalytic process may be due to the UV intensity limitation since UV photon energy excites only the valence band electrons.

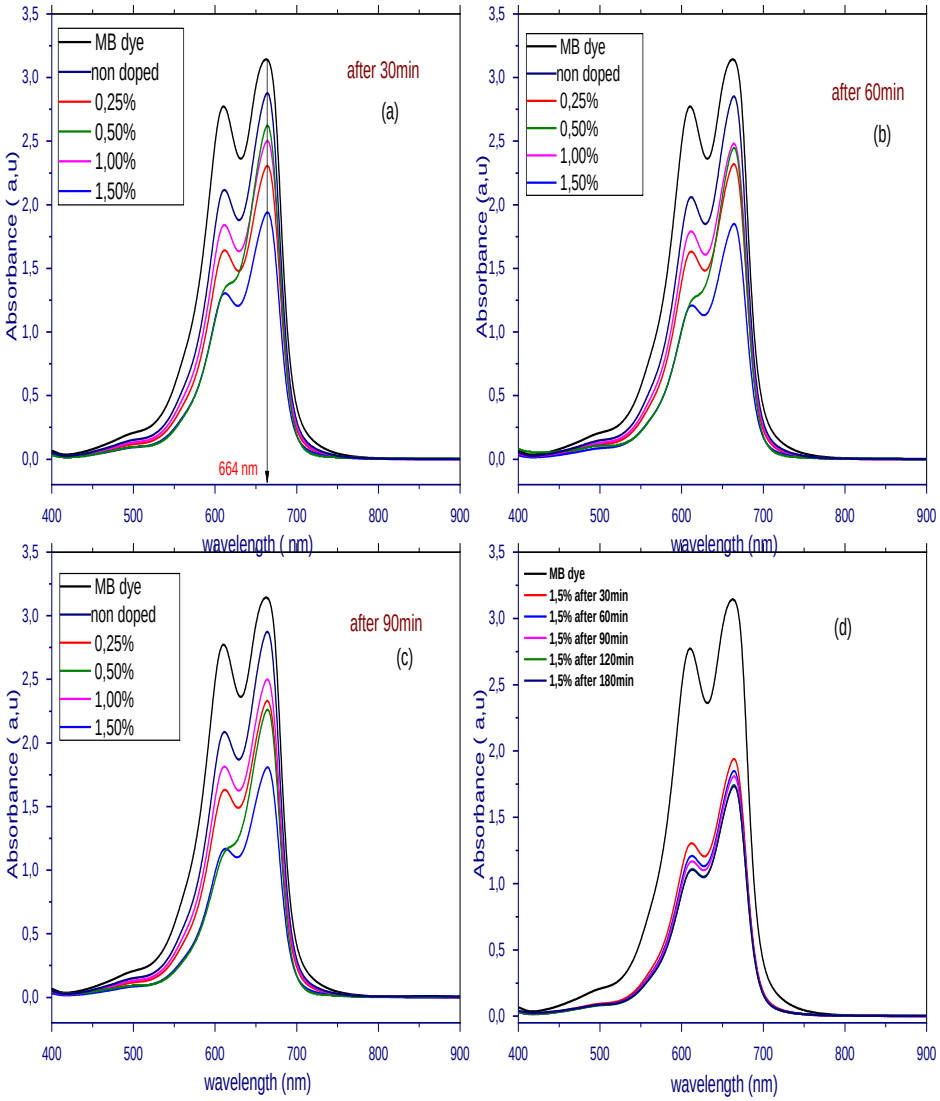

Fig.III.16 Time-dependent UV absorption spectra for MB dye in the presence of cobalt doped hematite thin films

Photodegradation percentages of MB dye for 0.25-1.5 wt. % cobalt doped hematite thin films under UV irradiation are indicated in Fig. III. 17. The results show that the doped film with 1.5 wt.% has the maximum degradation percentage which was 45% after 90 minute, whereas the other doped films reveal early saturation. This effect may be related to the presence of other phenomena, hence the active surface area of samples, dopant concentrations, and

hydroxyl group are not the same. For instance if one focuses on the results of 0.25 and 0.5 wt.% doped samples the comparison gives that 0.25 wt.% have smaller grain size which own it great active area. Even thought they have exhibited an equivalent OH radical as detected by FT-IR characterization (presence of hydroxyl group on their surfaces),the sample with 0.25 wt.% have a better Photocatalytic activity at the beginning (until 60 min of treatment process) owing to its active area, then 0.5 wt.% doped sample becomes the better one, which may refer to doping influence.

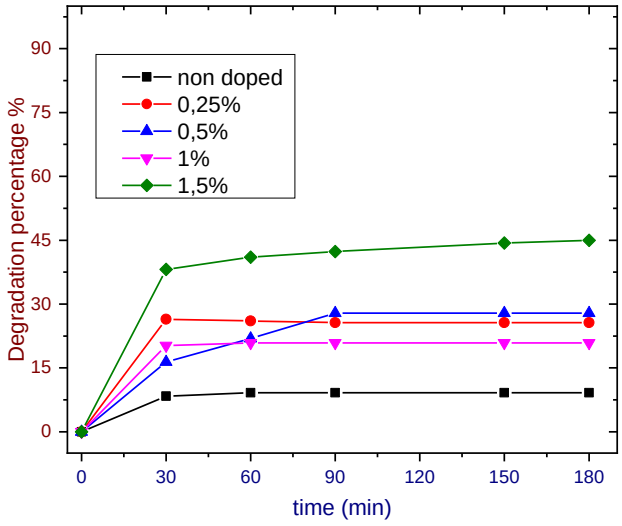

Fig.III.17 Degradation percentage of MB solution using cobalt doped hematite thin film under UV radiation.

III.7.3.3Photodegradation of MB dye under sun light condition

Under the sunlight, the process was different, the degradation of MB using 1.5% Co doped hematite thin film continue until the solution becomes transparent as shown in Fig.III.18.The degradation process as a function of time is shown in Fig.III.19.

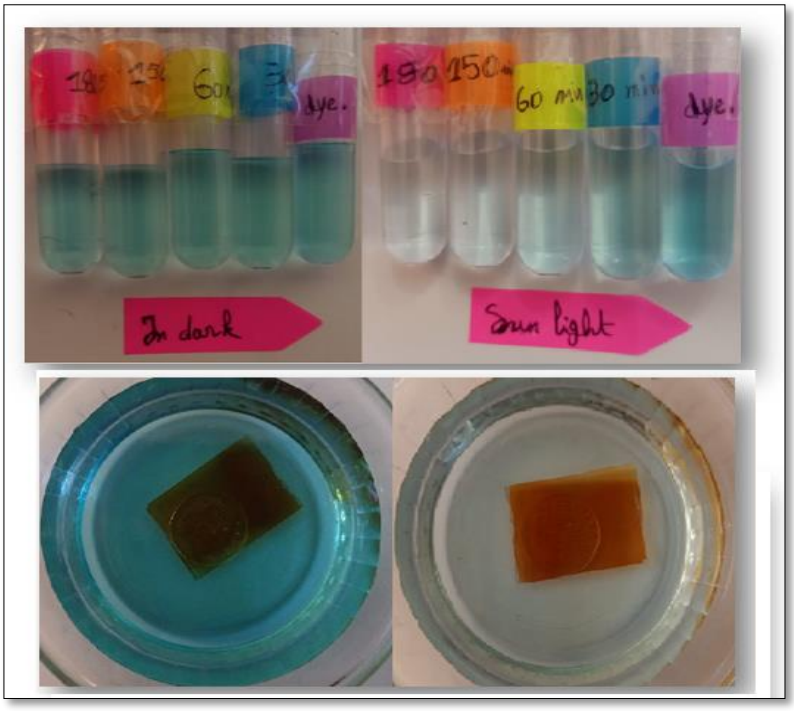

Fig. III. 18: Degradation process of 1.5% cobalt doped hematite thin film under sunlight radiation and dark after 180 minute.

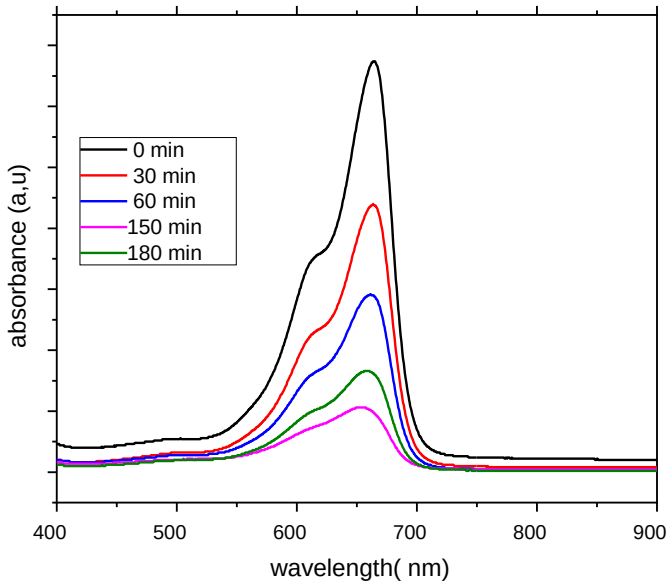

Fig. III. 19 Time-dependent absorption spectra for MB dye in the presence of 1.5% cobalt doped hematite thin films under sunlight radiation.

The degradation percentage under sunlight reaches 85.45% while it was 45% under UV and 16 % in dark. **Fig. III. 20**shows MB dye degradation percentage in dark, UV, and under sun light irradiation together.

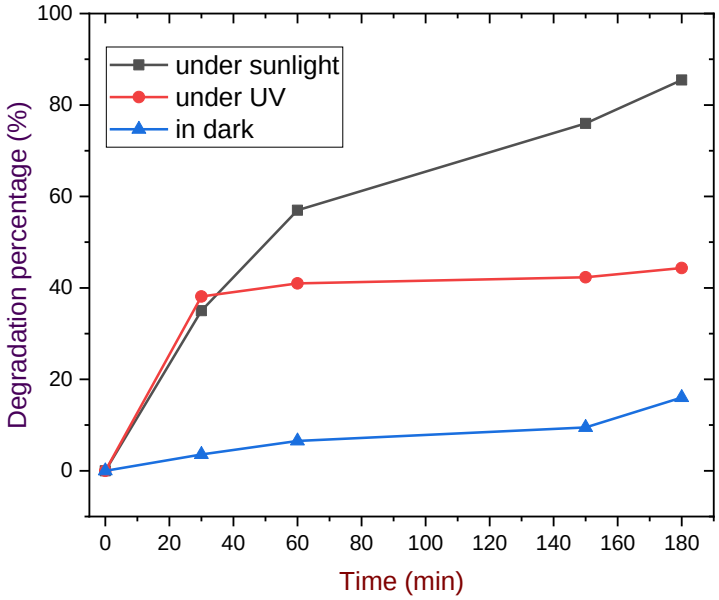

Fig. III. 20: Degradation percentage of MB solution using 0.5 % cobalt doped hematite thin film in dark and under sunlight radiation.

III. 7. 3. 4. Photocatalytic process of MB dye under sunlight:

The photocatalytic activity of 1.5 wt. % thin film under sunlight is better than UV illumination, this refer to a new parameter that ameliorates the photocatalytic activity, which is the wide range spectrum. Such spectrum is able to excite deep and shallow donors leading to an excess of electrons at the CB (e_{cb}^{-}) which in turn participate reduction of O_2 to O_2^{-}. The later is involved in the augmentation of superoxide radical anions as described in Fig. III. 3. Also those excited deep donors constitute electron trapping and avoid electron-hole pairs to recombine leading to an excess of holes in VB (h_{vb}^{+}) which means an excess in reduction of water molecules to OH.

The mainly frequent hole trapping site on the surface of iron oxide is **hydroxyl group,** which are presenting in the surface, the hydroxyl radical (OH•) is produced when a hole reacts with a surface hydroxyl group or an adsorbed water molecule. From Fig. III. 18, it is clear that a complete disappearance of the blue color of MB dye was happened, which is due to the reaction of OH• on the sites near the C–S+=C functional group and the central imino-group of the MB dye. The hydroxyl radicals is a high influential oxidants where they react non-selectively with nearly all organic substrates either via the elimination of H atom (•H) from C–H bonds or via the adding of double bonds and aromatic rings. The resulted carbon centered radical species (generated from the reaction with OH•) subsequently joins with O_2 at a diffusion-limited rate to creat alkyl peroxy radicals which are finally transformed into CO_2. For more details about postulated mechanisms, I advice the readers to see the appendix in the end of this thesis.

Conclusion

0-1.5wt. %Cobalt doped hematite iron oxide (α-Fe_2O_3) thin films were deposited on 500°C heated glass substrates via spray pyrolysis method with moving nozzle. The dopant concentration is stepped as 0, 0.25, 0.5, 1, and 1.5 wt. % Co/Fe. For all doped thin films, XRD analyses exhibit the presence of diffraction peaks corresponding to planes (*012*), (*104*), (*110*), confirming the formation of α-Fe_2O_3 phase. FTIR study confirms the existence of theα-Fe_2O_3. Doping of hematite iron oxide with Cobalt did not show any change in the crystal structure compared to the non doped one but it influence the grain size and enhances the hydroxyl combination on the surface of α-Fe_2O_3. The photocatalytic actions of the main thenthesized samples were examined derived from the MB degradation as a type composite, where the results indicated that Co doped hematite (α-Fe_2O_3) thin films have a better photocatalytic activity depend on several parameters including doping concentration, specific surface area, and OH contents on the surface structure.

The outcomes of this chapter are:

- The gap energy changes in the range (2.07-2.14 eV);
- 0.25 wt.% sample has the lowest grain size so largest Surface area and considerable amount of OH radical;
- 0.5 wt. % sample has moderate grain size and considerable amount of OH radical.

- 1 wt. % sample has big grain size so small surface area, and a few hydroxyl group on surface;
- The higher OH radical as detected byFT-IR characterizationis referred to 1.5 wt.% with high surface area.

It was concluded from this study that 1.5 wt.% has the best photocatalytic activity under UV light, this referred to the distinct three parameters: adequate doping concentration, high surface area, and higher OH radical. Under sunlight, the photocatalytic degradation of1.5 wt. % sample reaches 85.45% while it was 45% under UV and 16 % in dark., these can be originated from the ability of the spectrum to excite deep and shallow donors leading to an excess e_{cb}^{-}. Vacant trapping constitute a relay for electrons instead of recombining with holes leading to an excess of h_{vb}^{+}

References

[1] A. Albini, M. Fagnoni, ChemSusChem: Chemistry & Sustainability Energy & Materials, 1 (2008) 63-66.

[2] L. Bruner, J. Kozak, Zeitschrift Fur Elektrochemie Und Angewandte Physikalische Chemie, 17 (1911) 354-360.

[3] E. Baur, A. Perret, Helv Chim Acta, 7 (1924) 910-915.

[4] S.E. Braslavsky, M.B. Rubin, Photochemical & Photobiological Sciences, 10 (2011) 1515-1520.

[5] A. Fujishima, X. Zhang, D.A. Tryk, Surface science reports, 63 (2008) 515-582.

[6] C.F. Goodeve, J.A. Kitchener, Transactions of the Faraday Society, 34 (1938) 902-908.

[7] P. Boddy, Journal of The Electrochemical Society, 115 (1968) 199.

[8] A. Fujishima, K. Honda, nature, 238 (1972) 37-38.

[9] G. Schrauzer, T. Guth, Journal of the American Chemical Society, 99 (2002) 7189-7193.

[10] S.N. Frank, A.J. Bard, The journal of physical chemistry, 81 (1977) 1484-1488.

[11] T. Inoue, A. Fujishima, S. Konishi, K. Honda, Nature, 277 (1979) 637-638.

[12] G. Blondeel, A. Harriman, D. Williams, Solar energy materials, 9 (1983) 217-227.

[13] R. Wang, K. Hashimoto, A. Fujishima, M. Chikuni, E. Kojima, A. Kitamura, M. Shimohigoshi, T. Watanabe, Nature, 388 (1997) 431-432.

[14] N. Serpone, A. Emeline, S. Horikoshi, V. Kuznetsov, V. Ryabchuk, Photochemical & Photobiological Sciences, 11 (2012) 1121-1150.

[15] A. Kudo, K. Sayama, A. Tanaka, K. Asakura, K. Domen, K. Maruya, T. Onishi, Journal of catalysis, 120 (1989) 337-352.

[16] C. Kormann, D.W. Bahnemann, M.R. Hoffmann, Journal of Photochemistry and Photobiology A: Chemistry, 48 (1989) 161-169.

[17] R. Saravanan, F. Gracia, A. Stephen, Basic principles, mechanism, and challenges of photocatalysis, Nanocomposites for visible light-induced photocatalysis, Springer, 2017, pp. 19-40.

[18] M.M. Khan, S.F. Adil, A. Al-Mayouf, Elsevier, 2015.

[19] S. Rehman, R. Ullah, A. Butt, N. Gohar, Journal of hazardous materials, 170 (2009) 560-569.

[20] S. Zhu, D. Wang, Advanced Energy Materials, 7 (2017) 1700841.

[21] K. Rajeshwar, M. Osugi, W. Chanmanee, C. Chenthamarakshan, M.V.B. Zanoni, P. Kajitvichyanukul, R. Krishnan-Ayer, Journal of photochemistry and photobiology C: photochemistry reviews, 9 (2008) 171-192.

[22] K. Nakata, A. Fujishima, Journal of photochemistry and photobiology C: Photochemistry Reviews, 13 (2012) 169-189.

[23] A. Mills, S. Le Hunte, Journal of photochemistry and photobiology A: Chemistry, 108 (1997) 1-35.

[24] U.I. Gaya, A.H. Abdullah, Journal of photochemistry and photobiology C: Photochemistry reviews, 9 (2008) 1-12.

[25] S. Ahmed, M. Rasul, R. Brown, M. Hashib, Journal of environmental management, 92 (2011) 311-330.

[26] D. Spasiano, R. Marotta, S. Malato, P. Fernandez-Ibanez, I. Di Somma, Applied Catalysis B: Environmental, 170 (2015) 90-123.

[27] S. Ahmed, M. Rasul, W.N. Martens, R. Brown, M. Hashib, Desalination, 261 (2010) 3-18.

[28] V.C. Sarasidis, K.V. Plakas, S.I. Patsios, A.J. Karabelas, Chemical Engineering Journal, 239 (2014) 299-311.

[29] Y. Zhou, L. Shuai, X. Jiang, F. Jiao, J. Yu, Advanced Powder Technology, 26 (2015) 439-447.

[30] R. Saravanan, S. Karthikeyan, V. Gupta, G. Sekaran, V. Narayanan, A. Stephen, Materials Science and Engineering: C, 33 (2013) 91-98.

[31] G. Cernuto, N. Masciocchi, A. Cervellino, G.M. Colonna, A. Guagliardi, Journal of the American Chemical Society, 133 (2011) 3114-3119.

[32] D.M. Blake, J. Webb, C. Turchi, K. Magrini, Solar Energy Materials, 24 (1991) 584-593.

[33] L.V. Bora, R.K. Mewada, Renewable and Sustainable Energy Reviews, 76 (2017) 1393-1421.

[34] W. Vallejo, A. Cantillo, B. Salazar, C. Diaz-Uribe, W. Ramos, E. Romero, M. Hurtado, Catalysts, 10 (2020) 528.

[35] W. Chen, Z. Lu, B. Xiao, P. Gu, W. Yao, J. Xing, A.M. Asiri, K.A. Alamry, X. Wang, S. Wang, Journal of Cleaner Production, 211 (2019) 1250-1258.

[36] O. Akhavan, R. Azimirad, Applied Catalysis A: General, 369 (2009) 77-82.

[37] J. Bandara, U. Klehm, J. Kiwi, Applied Catalysis B: Environmental, 76 (2007) 73-81.

[38] A. Lassoued, M.S. Lassoued, B. Dkhil, S. Ammar, A. Gadri, Journal of Materials Science: Materials in Electronics, 29 (2018) 8142-8152.

[39] R. Sonawane, M. Dongare, Journal of Molecular Catalysis A: Chemical, 243 (2006) 68-76.

[40] N. Madubuonu, S.O. Aisida, A. Ali, I. Ahmad, T.-k. Zhao, S. Botha, M. Maaza, F.I. Ezema, Journal of Photochemistry and Photobiology B: Biology, 199 (2019) 111601.

[41] J.J. Freedsman, L.J. Kennedy, R.T. Kumar, G. Sekaran, J.J. Vijaya, Materials Research Bulletin, 45 (2010) 1481-1486.

[42] R. Satheesh, K. Vignesh, A. Suganthi, M. Rajarajan, Journal of environmental chemical engineering, 2 (2014) 1956-1968.

[43] M.K. Lima, D.M. Fernandes, M.F. Silva, M.L. Baesso, A.M. Neto, G.R. de Morais, C.V. Nakamura, A. de Oliveira Caleare, A.A.W. Hechenleitner, E.A.G. Pineda, Journal of sol-gel science and technology, 72 (2014) 301-309.

[44] A.M. Glazer, A Journey into Reciprocal Space: A Crystallographer's Perspective, Morgan & Claypool Publishers, 2017.

[45] K. Ueda, H. Tabata, T. Kawai, Applied Physics Letters, 79 (2001) 988-990.

[46] K.J. Kim, Y.R. Park, Applied Physics Letters, 81 (2002) 1420-1422.

[47] R.D. Shannon, Acta crystallographica section A: crystal physics, diffraction, theoretical and general crystallography, 32 (1976) 751-767.

[48] M. Tay, Y. Wu, G.C. Han, T.C. Chong, Y.K. Zheng, S.J. Wang, Y. Chen, X. Pan, Journal of applied physics, 100 (2006) 063910.

[49] B.D. Cullity, Elements of X-ray Diffraction, Addison-Wesley Publishing, 1956.

[50] J. Tauc, R. Grigorovici, A. Vancu, physica status solidi (b), 15 (1966) 627-637.

[51] S. Shinde, R. Bansode, C. Bhosale, K. Rajpure, Journal of Semiconductors, 32 (2011) 013001.

[52] A.A. Yadav, T. Deshmukh, R. Deshmukh, D. Patil, U. Chavan, Thin Solid Films, 616 (2016) 351-358.

[53] Y. Meftah, D. Bekker, B. Benhaoua, A. Rahal, A. Benhaoua, A. Hamzaoui, Digest Journal of Nanomaterials and Biostructures, 13 (2018) 465-474.

[54] E. Darezereshki, Materials Letters, 65 (2011) 642-645.

[55] A. Houas, H. Lachheb, M. Ksibi, E. Elaloui, C. Guillard, J.-M. Herrmann, Applied Catalysis B: Environmental, 31 (2001) 145-157.

CHAPTER IV :

SYNTHESIS, CHARACTERIZATIONS, AND ANTIBACTERIAL ACTIVITY OF COBALT DOPED HEMATITE THIN FILMS DEPOSITED BY SPRAY PYROLYSIS.

IV. 1. Introduction to antibacterial activity

The appearance of infectious disease generally creates a grave danger to human health, particularly with the presence of antibiotic-resistant bacterial damages. In general both Gram-positive and negative bacterial damages are considered to present a most important human health trouble. Over the years, antibiotics have been utilized to have power over infections ensuing from both the public and hospital environments [1–3]. Recent advances in the nanobiotechnology field, mainly the ability to arrange metal oxide NMs of specific size and shape, are expected to lead en route for the development of new antibacterial agents. The functional activities of nanoparticles are affected largely by the particle size. So, NPs have gained great attention because of their unique chemical, physical, and useful biological properties in different fields, counting medicine. The properties of nanoparticles are altered by decreasing or changing their size, particularly when the manipulations are done at the nanometer range [4–7]. Similarly, materials tailoring at the atomic plane in order to attain unique properties has been extensively reported. Taking in account these unique properties, nano dimensioned organic and inorganic particles are being engendered for eventual use in medical performs, such as IO. As an example, Seerangaraj Vasantharajet all. [8] demonstrate that IONPs showed higher antibacterial activity against *Escherichia coli, Klebsiella pneumoniae* and lesser antibacterial activity against *Staphylococcus aureus*. Bactericidal activity of such nanoparticles in part depends on (i) size, (ii) stability, and (iii) concentration in the medium of growth. Whilst growing in medium adjusted with NP, the bacterial population growth can be inhibited by specific NP interactions [7]. In general, bacterial cell size is in the micrometer range, while its external cellular membranes have pores in the nanometer scale. Since NPs can be smaller in form than bacterial pores, they will have a unique facility of entering the cell membrane. There lies a strong challenge in elaborating metal oxide NPs stable adequate to restrict bacterial growth notably while in nutrient medium.

Understanding the potential antimicrobial applications of metal oxide NPs, we designed experiments to synthesize α-Fe_2O_3 nanoparticles doped with Cobalt using spray pyrolysis method and subsequently tested their antibacterial activities against both Gram-positive Listeria innocua and Gram-negative: Escherichia Coli, ,Pseudo monas aeruginosa and SaLMonelleentérinant, bacterial strains. Furthermore, the antibacterial behavior of these nanoparticles was discused.

IV. 2. Experimental details

IV. 2. 1 Thin films preparation

Cobalt doped iron oxide NPs were prepared using SPMN method, which was explained in the previous chapter and represented in Fig.III.6. To obtain mother solution of 0.5M of Fe^{+3}, 1.622g of iron chloride ($FeCl_3$) was dissolved in 20mL of distilled water and ethanol mixture in volume ratio 1:1 and stirred vigorously until complete dissolution (red brownish solution). Then, different quantities of cobalt chloride $CoCl_2$ were added to this solution with keep stirring for 30 min to get a range of dopant concentration (2, 5, 10, and 20 wt %). The obtained blends were sprayed onto 500°C heated glass substrates (Ref 217102: having 7.5x2.5x0.13cm^3 as dimensions). The deposition time was 3min with spray rate of 5ml/min and kept distance nozzle-substrate of 5cm. Moving nozzle and high deposition temperature are used to preserve the stability of substrate and oxidation reaction temperatures. The prepared slides were annealed for two hours at 550°C

IV. 2. 2. Thin films characterization

The crystallographic structure of 0-20 wt. % Co-doped α-Fe_2O_3 thin films have been examined via a Philips X-ray diffractometer model PW-1710 operating with (λ = 1.5406 Å for Cu-Kα radiation). Optical properties such as transmittance and band gaps have been undergone through the optical transmittance spectrum using (UV–VIS spectrophotometer Shimadzu, Model 1800) working in 300-900nm wavelength range. Whereas FT-IR analysis was performed, in 400-4000cm^{-1}range, by use of Shimadzu IR-Infinity 1 apparatus. All the measurements were carried out at room temperature (rt).

IV. 2. 3. Antibacterial assay

The antibacterial activity of paper composites was determined by disk diffusion assay using:

* Gram-negative as: Escherichia Coli, ATCC25922: E.C),Pseudo monas aeruginosa,(ATCC 27853: P.S) and SaLMonelleentérinant, (CIP 81-3: SLM)

* Gram-positive as Listeria innocua, (CLIP 74915 : Lis)

Miller Hinton agar (MHA) was poured into a sterilized Petri dish and solidified within 10 min. E. C, Lis, P.S and SLM bacterial suspensions were uniformly inoculated on solidified agar gel. Sterile disks with 6mm in diameter were placed in different Co-hematite nanoparticles solutions which were obtained via grating the slides and dissolving the result powder in Dimethyl sulfoxide (DMSO) having the formula $(CH_3)_2SO$. The discs were then sited over the MHA plates and incubated for 24h at 37°C. The antibacterial activities were compared by the diameter of the inhibition zone around each paper disk.

IV. 3. Results and discussions

IV. 3. 1 Structural properties

The XRD patterns of 0-20 wt. % Co-doped hematite thin films are presented in Fig.IV.1. For non doped samples, the observed peaks at 2θ: 24.23°, 33.24°, 35.70°, 40.95°,49.54°,54.18°, 62.50°, and 64.17°correspond to lattice plane of (012), (104), (110), (113), (024), (116), (214) and (300), respectively confirm the formation of rhombohedral crystal structure of α-Fe_2O_3 and much well with its (JCPDS No: 01.073-2234, with space group R-3c number 167). For doped samples, all the observed peaks in the case of non doped samples persevere with approximately fixed slight shift to lower 2θ values for all Co dopant concentration. This shift may be due to the bigger radius of cobalt, comparedto iron one (R_{Co+2} = 0.72Å, and R_{Fe+3} = 0.64 Å) [9].

Fordoping at 2 wt.%, a new peak appears in the XRD spectrum related to (200) plane, intensity of which fails down at 10 wt.% of doping; this peak corresponds to cobalt monoxide (CoO) reported to (JCPDS No: 01.043-1004). For doping much than 5 %, additional peak referred to (311) plane is observed and intensifies with mounting of doping. This indicates the presence of Cobalt (II, III) oxide (Co_3O_4) and much well with (JCPDS No: 01.065-3103). This is in good agreement with what showed in literature [10] and ensure that the used Co doping concentration (more than 2 wt. % Co/Fe) affect the Fe_2O_3 crystallographic structure thin films.

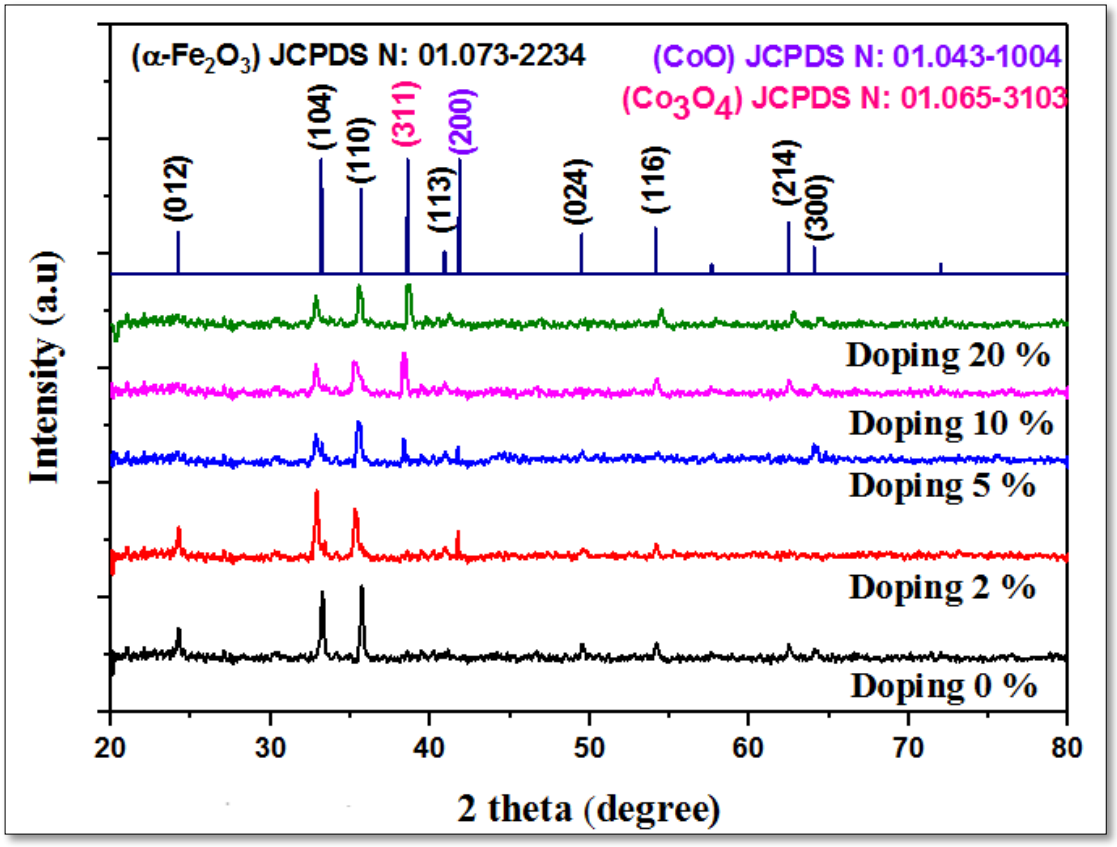

Fig.IV.1 X-ray diffraction patterns of sprayed hematite α-Fe_2O_3 of pure and Co-doped thin films.

lattice constants (a and c), for the rhombohedral phase structure, are determined by the relations (II.5) and (II.7). The values of lattice parameters 'a' and 'c' are listed in Table.IV.1. It is worth noting that the values (a = b = 5.02896Å, c = 13.7255Å) of the pure samples are close to the ones of the standard JCPDS data card, (a_0 =b_0 = 5.0325 Å and c_0 = 13.7404Å).

The increase in lattice parameters of Co doped hematite thin films compared with the non doped one is due to the substitution of larger ionic radii of Co^{2+} into the position of smaller ionic radii of Fe^{3+} in α-Fe_2O_3 lattice (the ionic radius of Co^{2+} is: 0.67 A °, and for Fe^{3+} is: 0.58A °) [11]. Those values are increased by very small amount up to 2wt.%, this confirms elongation of unit cell along c-direction hence Δc more than Δa, this result is in good agreement with literature [9].

Table.IV.1: 0-20wt.% Co doped thin films parameters: d_{hkl},, average grain size, lattice parameters, optical gap, and Urbach energy.

Co/α-Fe_2O_3	*hkl*	2θ(°)	$FWHM_\beta$(Rad)	D(nm)	d_{hkl}(Å)	Latticeparameters (Å)	Unit cell volume (Å^3)	Eu (eV)	Eg (eV)
0%	104	33.239	0.22367	37.08	d_{104}=2.6945	a=5.0272	300.212	0.217	.207
	110	35.709	0.21831	38.24	d_{110}=2.5136	c=13.717			
2%	104	32.920	0.17457	47.46	d_{104}=2. 7199	a=5.0769	309.079	0.194	2.09
	110	35.348	0.24193	34.49	d_{110}=2.5384	c=13.847			
	200	41.697	0.26024	32.67	d_{200}=2.1654	a=4.3308			
5%	104	33.920	0.19125	43.32	d_{104}=2.7199	a=5.0769	309.079	0.160	2.12
	110	35.348	0.31256	26.70	d_{110}=2.5384	c=13.847			
	200	41.796	0.28784	29.55	d_{200}=2.1605	a=4.3210			
	311	38.310	0.19135	43.97	d_{311}=2.3487	a=7.7898			
10%	104	32.920	0.22826	36.30	d_{104}=2.7199	a=5.0769	309.079	0.352	2.15
	110	35.348	0.40925	20.39	d_{110}=2.5384	c=13.847			
	311	38.310	0.39597	21.24	d_{311}=.23487	a=7.7998			
20%	104	32.920	0.28934	28.63	d_{104}=2.7199	a=5.0769	309.079	0.409	2.22
	110	35.348	0.35697	23.38	d_{110}=2.5384	c=13.847			
	311	38.300	0.46553	18.07	d_{311}=2.3493	a=7.7918			

The crystalline sizes of 0-20wt.% Co doped thin filmswere calculated for the more intense peaks using Scherrer'sformula (II.6). The Crystallite size variation shown in Fig.IV.2; it increases from 37.08nm for undoped hematite nanoparticles to 47.46nm for 2% doping. By increasing the dopant concentration to 5%, the crystallite size decreases to 43.32nm. For dopant concentration of 10%, crystallite size is reduced to 36.30nm, this value keeps decreasing to 28.63nm till 20% dopant concentration. Decrease in crystallite size at dopant concentration starting from 5% can be attributed to presence of cobalt ions which coincide with oxygen forming its own oxide (CoO and Co_3O_4), this can be defined as a crystal defects which well match with increasing in the Urbach energy. The reduction in crystallite size was observed as a result of cobalt oxide presence in the films, this result is compatible with literature [12].

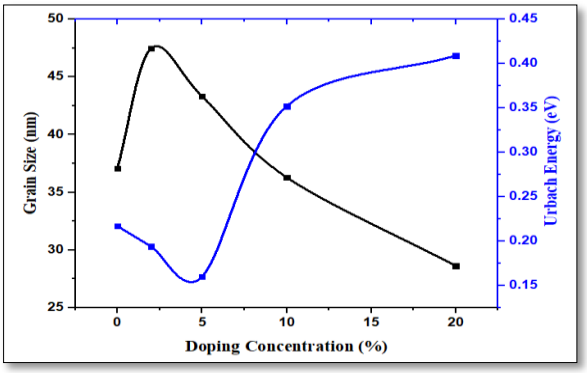

Fig.IV. 2 Variation of Grain size and Urbach energy 0-20wt% Co doped thin films.

IV. 3. 2 Surface morphology

The surface morphology of Co doped iron oxide thin films (Co-α-Fe2O3) are studied via SEM. Fig.IV.3(a,b,c, and d) shows the results with different doping concentration (2,5,10, and 20wt.%) respectively. The SEM images demonstrate that the grain size is homogeneous with some agglomerating sites. The average grain sizes are: 166,200,227, and 225 nm for 2,5,10, and 20wt.% respectively, those value are much higher than which were found in XRD, which confirm the fact that each grain is formed by aggregation of few numbers of nanocrystals.

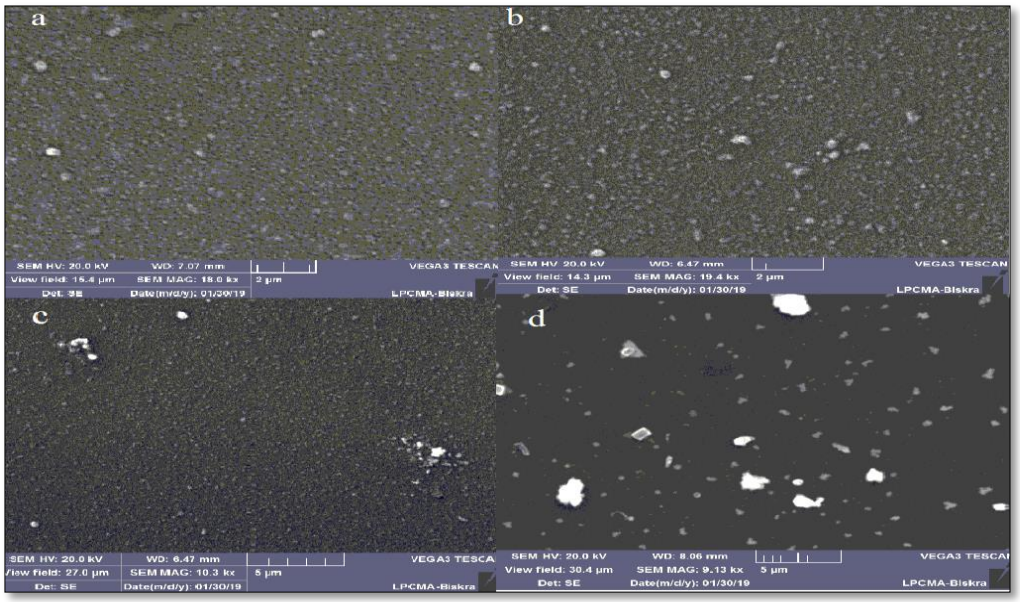

Fig.IV.3 SEM analysis of 0-20wt.% Co doped hematite thin films ((a):2wt.%,(b):5wt.%,(c):10wt.%, and (d): 20wt.%)

IV. 3. 3. Optical properties

Photos of elaborated thin films are presented in Fig.IV.4 which exhibits the change in color as a function of doping concentration.Fig.IV.5 shows the transmittance spectrum of 0-20wt.% Co doped thin films. For the undoped sample, the transmittance spectrum was foundto be about 65% beyond 550nm. For the doped ones this value decreases to reach 60% at dopant concentration 2%, then increases to exceed 80% for the 5 and 10% wt Co doped samples whereas for 20 % Co doped sample the value of transmittance becomes lower than 80%. Bellow 550nm, the transmittance spectrum display a drastic decrease due the fundamental absorption of the materials (*i.e* the band gap).

The band gap has been calculated using,Tauc's relation (II.14). The optical absorption data was used to plot $(\alpha h\nu)^2$vs$h\nu$, as shown in Fig.IV.6, the straight line extrapolation leads to the band gap energy values of 0-20 wt .% Co doped samples. An obvious increase (blue shift) in *Eg*for the Co doped hematite thin films compared to the non doped ones; *Eg* increases from 2.07 for pure α-Fe_2O_3 to 2.09, 2.12, 2.15, and 2.22eV in respect to the dopant concentration 2%, 5%, 10%, and 20 wt.%, respectively. It is worth noting that the first ionization energy of Cobalt (7.88eV) is less than that one of iron (7.90eV) leading to a localization 3d orbital of cobalt higher than 3d orbital of iron This can causes an active transitions engaging 3d levels in Co^{+2} ions and strong pd-d exchange interaction between itinerant pd α-Fe_2O_3 orbits and the restricted d of the dopant. As a result a narrowing in the conduction band E_C and the valence band E_V happens and causes a shift of E_C upwards and E_V downwards, which leads to proclaim that Co doping causes the band gap broadening. The same phenomena (blue shift) are carried out in the literatures [9,13, 14]

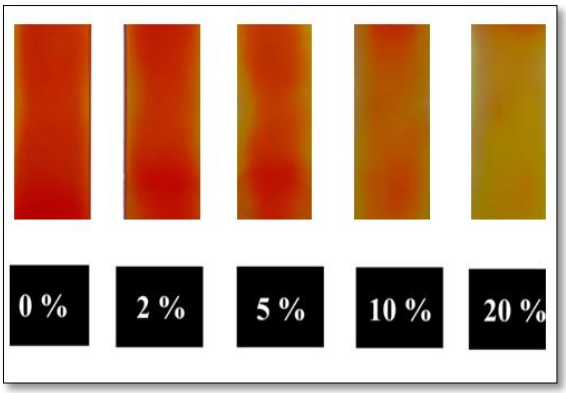

Fig.IV.4 *Photographs of elaborated samplesof 0-20% wt Co-doped α-Fe_2O_3 thin films*

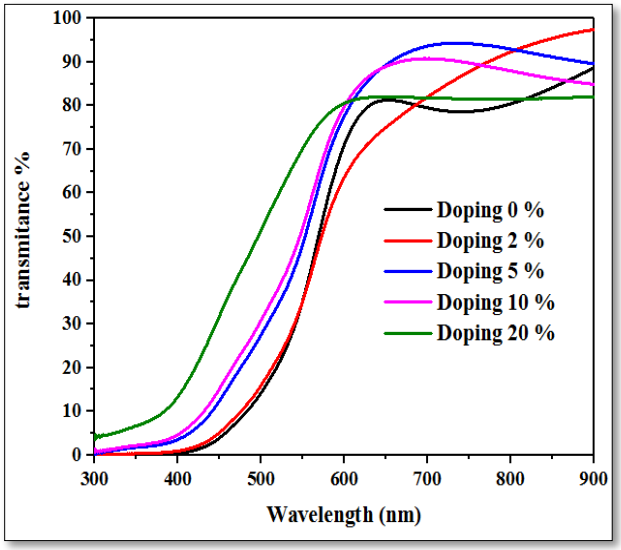

Fig. IV. 5 Transparency spectrum of (0-20wt. %) Co-doped α-Fe_2O_3 thin films.

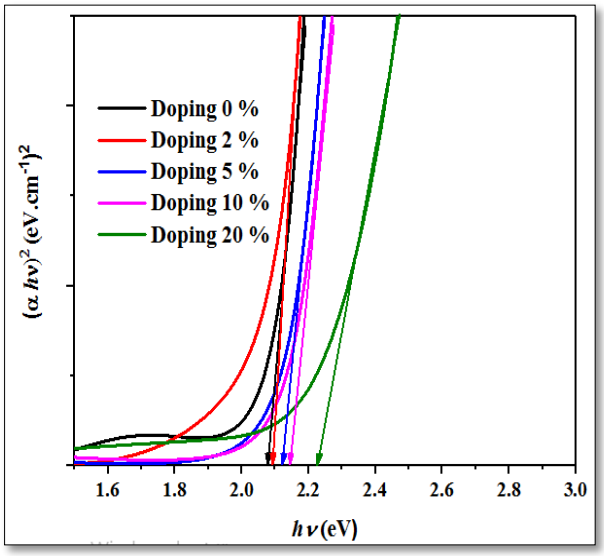

Fig. IV. 6 Estimated band gap (E_g) from Tauc's relation for 0-20%wt Co doped α-Fe_2O_3 thin films.

IV.3.4 Fourier transform infra‑red (FT‑IR) spectroscopy

Fig.IV.7 shows the FTIR spectra of the Co-doped α-Fe_2O_3 thin films upon different dopant concentration. The peaks in the range 460-563cm^{-1} were attributed to the Fe-O and Co-O stretching mode [9]. The peaks intensity and the area absorption increase directly with the dopant concentration specifically at 20 wt. % (see inset), which gives rise in the compound

formation of iron and cobalt oxides. The absorption peak centered at 1640 cm^{-1} indicates the presence of COO- stretch mode [15, 16]. While the absorption one at 2358 $cm^{-1}$is referred to the presence of CO_2 molecules, which may refer to the surrounding atmosphere during preparation.

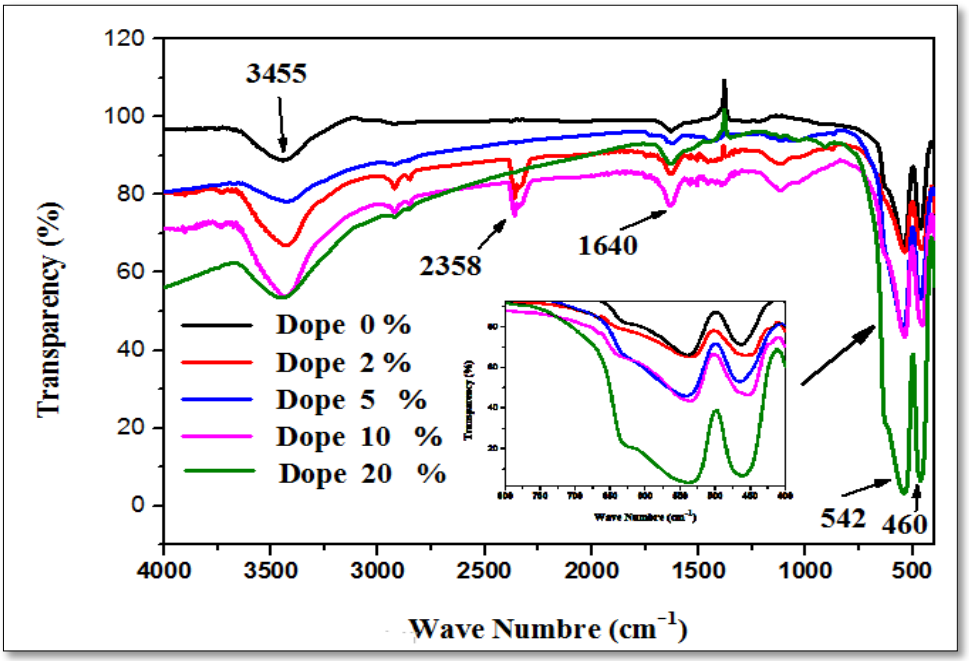

Fig.IV.7 FTIR spectrum of α-Fe_2O_3 of pure and Co-doped thin films.

IV. 3. 5. Antibacterial Activity

The antimicrobial activity of Co-hematite nanoparticles was given in Fig.IV.8. The nanoparticles correspond to 20% Co doping show an activity against E. coli and Lis. For 10% there are activity against P.a, SLM and Lis. For 5% of doping there are activity against E. coli and P. a. No activity was shown for 0% and 2%. From this study, it may be revealed that high doped Co-hematite nanoparticles exhibits good activity against both the gram positive and gram negative organisms. The bactericidal effect of iron oxide nanoparticles may be due to their smaller size. The inactivation of E. coli by iron oxide nanoparticles could be because of the penetration of the small particles (sizes ranging from 10 to 80 nm) into E. coli membranes, leading to oxidative stress and causes interruption of the cell membrane [17]. The significance of study showed that the saturation of the media with the iron nanoparticles results in loss of oxygen which may be due to the Fenton's reaction.

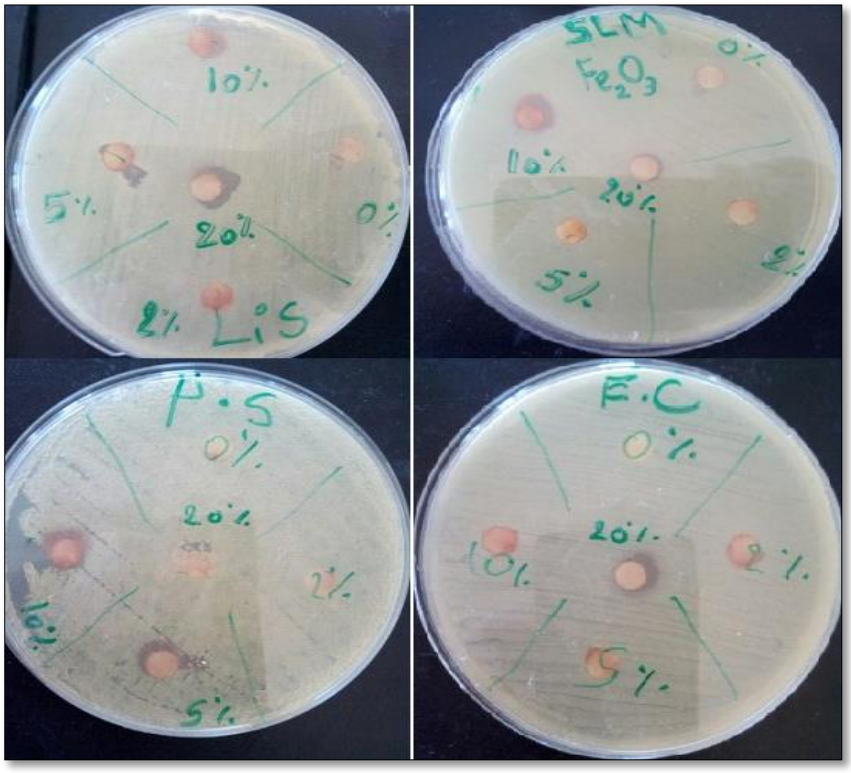

Fig.IV.8 Inhibitation Zone for different bacteriaas a function of doping concentrations.

IV. 4 Conclusions

Cobalt doped iron oxide (hematite) nanoparticles were prepared using spray pyrolysis method. The dopant concentration is varied at 2, 5, 10, and 20wt.%. Presence of diffraction peaks corresponding to plans (*012*), (*104*), (*110*), (*113*), (*024*), (*116*), (*214*), and (*300*) signified the hematite phase formation. As a result of doping, two added peaks were appeared much well to planes (*200*) and (*311*) which correspond to cobalt oxides CoO and Co_3O_4 respectively. The peaks positions corresponding to hematite marked a fixed slight shift to lower 2θ values for all Co dopant concentration. Crystallite size increases in the beginning of dopping than it take a successive reduce values in increase at dopant concentration. The optical transmittance and the band gap values increase with increasing the dopant concentration. FTIR study confirms the existence of both Iron and Cobalt oxides. As an application in the areas of the antibacterial test, the synthesized cobalt doped hematite NPs exhibit a good antibacterial activity against E. coli, Listeria innocua, Pseudo monasaeruginosa and Salmonella enteric beyond 5wt. % Co/Fe doping.

Reference

[1] Lowy, Franklin D. "Staphylococcus aureus infections." New England journal of medicine 339.8 (1998): 520-532.

[2] Komolafe, O. O. "Antibiotic resistance in bacteria-an emerging public health problem." Malawi medical journal 15.2 (2003): 63-67.

[3] Hawkey, P. M. "The growing burden of antimicrobial resistance." Journal of antimicrobial chemotherapy 62.suppl_1 (2008): i1-i9.

[4] Lewis, Kim, and Alexander M. Klibanov. "Surpassing nature: rational design of sterile-surface materials." TRENDS in Biotechnology 23.7 (2005): 343-348.

[5] Rosi, Nathaniel L., and Chad A. Mirkin. "Nanostructures in biodiagnostics." Chemical reviews 105.4 (2005): 1547-1562.

[6] Azam, Ameer, et al. "Size-dependent antimicrobial properties of CuO nanoparticles against Gram-positive and-negative bacterial strains." International journal of nanomedicine 7 (2012): 3527.

[7] Raghupathi, Krishna R., Ranjit T. Koodali, and Adhar C. Manna. "Size-dependent bacterial growth inhibition and mechanism of antibacterial activity of zinc oxide nanoparticles." Langmuir 27.7 (2011): 4020-4028.

[8] Vasantharaj, Seerangaraj, et al. "Biosynthesis of iron oxide nanoparticles using leaf extract of Ruellia tuberosa: antimicrobial properties and their applications in photocatalytic degradation." Journal of Photochemistry and Photobiology B: Biology 192 (2019): 74-82.

[9] R. Satheesh, K. Vignesh, A. Suganthi, M. Rajarajan, Visible light responsive photocatalytic applications of transition metal (M= Cu, Ni and Co) doped α-Fe2O3 nanoparticles, Journal of Environmental Chemical Engineering, 2 (2014) 1956-1968.

[10] S. Anjum, R. Tufail, K. Rashid, R. Zia, S. Riaz, Effect of cobalt doping on crystallinity, stability, magnetic and optical properties of magnetic iron oxide nano-particles, Journal of Magnetism and Magnetic Materials, 432 (2017) 198-207.

[11] Shannon, R. D. (1976). Revised effective ionic radii and systematic studies of interatomic distances in halides and chalcogenides. Acta crystallographica section A: crystal physics, diffraction, theoretical and general crystallography, 32(5), 751-767.

[12] vallejo, william, et al. "comparative study of zno thin films doped with transition metals (cu and co) for methylene blue photodegradation under visible irradiation." catalysts 10.5 (2020): 528

[13] B.K. Ozcelik, C. Ergun, Synthesis and characterization of iron oxide particles using spray pyrolysis technique, Ceramics International, 41 (2015) 1994-2005.

[14] S. Shinde, R. Bansode, C. Bhosale, K. Rajpure, Physical properties of hematite α-Fe2O3 thin films: application to photoelectrochemical solar cells, Journal of Semiconductors, 32 (2011) 013001.

[15] C. Zhang, Z. Yu, G. Zeng, B. Huang, H. Dong, J. Huang, Z. Yang, J. Wei, L. Hu, Q. Zhang, Phase transformation of crystalline iron oxides and their adsorption abilities for Pb and Cd, Chemical Engineering Journal, 284 (2016) 247-259.

[16] R. Todorovska, S. Groudeva-Zotova, D. Todorovsky, Spray pyrolysis deposition of α-Fe 2 O 3 thin films using iron (III) citric complexes, Materials Letters, 56 (2002) 770-774.

[17] C. Lee, J.Y. Kim, W.I. Lee, K.L. Nelson, J. Yoon, D.L. Sedlak, Bactericidal effect of zero-valent iron nanoparticles on Escherichia coli, Environmental science & technology, 42 (2008) 4927-4933.

GENERAL CONCLUSION

General conclusion

This thesis contains four chapters, the first chapter is an art of state about iron oxides and their applications, where general information about iron oxides and their properties in different sides have been illustrated then applications of iron oxide nanoparticles in environment have been discussed which includes the area of wastewater treatment and antibacterial test. The second is about elaboration and characterization methods used for elaborating hematite thin films. Characterization tools also have been discussed for investigating the structural, morphological, optical analysis.

As conclusion of the experimental chapters, it draws as follow:

The α-Fe_2O_3(hematite) thin filmswere successfully fabricated via spray pyrolysiswith moving nozzle at 500°C.Thestructure, morphology, and optical properties of the deposited Co-doped α-Fe_2O_3thin films have been investigated. The main focus of this investigation was:

- To observe the effect of doping on the properties of α-Fe_2O_3 thinfilms, including XRD analysis, surface morphology, transparency of the films, and gap energy;
- To study the Photocatalytic effect of Co-α-Fe_2O_3, low Co doped iron oxide was proceed (0.25-1.5 wt.%);
- To study the antibacterial test of Co-α-Fe_2O_3, high Co doped iron oxide have been proceed. (2-20 wt. %)

The XRD analyses of thelow doped Co-α-Fe_2O_3at:(0.25,0.5,1, and 1.5wt.%) confirm that the doping processdid not affect the main peaks in diffraction patterns, however, it show a change in their intensities, suggesting that Cobalt ions doping enhances the growth of the product. FTIR study confirms the existence of theα-Fe_2O_3,the hydroxyl radical enhanced by Cobalt doping on the surface of α-Fe_2O_3 which is considered as good result for photocatalytic application. Photocatalytic test indicated that the decolorization rate -under UV irradiation- of MB using 1.5wt.%Co-α-Fe_2O_3

thin films reached 45%, while it reached 85.45% under sunlight irradiation, so, this type of catalyst is a potential candidate for organic dye degradation in large-scale applications.

As a result of high dopedα-$Fe_2O_3$with rate of:(2, 5, 10, and 20wt.%), two added peaks were appeared in the XRD pattern much well to planes (*200*) and (*311*) corresponding to cobalt oxides CoO and Co_3O_4 respectively. This indicates a differencebehavior of Cobalt ions at high doping concentration. Crystallite size increases in the beginning of doping then it reduces successively(till 28.63 nm at 20wt.%), which is considered as a good result for the application of the Co-α-Fe_2O_3in antibacterial field. The synthesized cobalt doped hematite NPs exhibit a good antibacterial activity against E. coli, Listeria innocua, Pseudo monasaeruginosa and Salmonella enteric beyond 5wt. % Co/Fe doping.

There is much recent interest in the use of iron oxide nanoparticles as an important tool inwastewater and antibacterial treatment. In future study, a focus on effect of Co dopant concentrations will be taken in consideration under sunlight illumination, also co doping in enhancing phototcatalytic activity will be undergo.

APPENDIX

Postulated mechanism of MB dye drgradation

In the Co-α-Fe_2O_3 photocatalytic degradation process, oxidative degradation of MB occurs generally by the attack of •OH radicals, known as highly reactive electrophilic oxidants. Generally, the sites near the C–S+=C functional group and the central imino-group are the attack area in photocatalytic degradation process. The main identified intermediates resulting from MB degradation are sulfoxide, sulfone, sulfonic acid, and substituted aniline. Based on these, though intermediates forming in the photocatalytic degradation process of MB were not identified, the mechanism suggested by Houas et al. [1] was also postulated in our system (**svhema. 1**). The initial step of MB degradation can be ascribed to the cleavage of the bonds of the C–S+=C functional group in MB:

$$R - S^+ = R' + OH^\circ \rightarrow R - S(=O) - R' + H^+$$

The electrophilic attack of OH° concerned the free doublet of heteroatom S, making its oxidation degree pass from −2 to 0. However, the passage from C–S+=C to C–S(=O)–C requires the conservation of the double bond conjugation, which induces the opening of the central aromatic ring containing both heteroatoms, S and N. The origin of H atoms necessary to C–H and N–H bond formation can be proposed from the proton reduction by photogenerated electrons:

$$H^+ + e^- \rightarrow H^\circ$$

The sulfoxide group can undergo a second attack by an OH° radical producing the sulfone and causing the definitive dissociation of the two benzenic rings:

$$NH_2 - C_6H_3(R) - S(=O) - C_6H_4 - R + OH^\circ \rightarrow NH_2 - C_6H_3(R) - SO_2 + C_6H_5 - R$$

and/ or

$$NH_2 - C_6H_3(R) - S(=O) - C_6H_4 - R + OH^\circ \rightarrow NH_2 - C_6H_4 - R + SO_2 - C_6H_4 - R$$

The oxidation degree of sulfur has now increased from 0 to **+**5. Subsequently, the sulfone can be attacked itself by a third OH° radical for giving a sulfonic acid:

$$SO_2 - C_6H_4 - R + OH^\circ \rightarrow R - C_6H_4 - SO_3H$$

Presently, sulfur has reached its final, stable and maximum oxidation degree (**+**6) and the final release of $SO4^{2-}$ ions can be attributed to a fourth attack by OH°:

$$R - C_6H_4 - SO_3H + OH^\circ \rightarrow R - C_6H_4^\circ + {SO_4}^{2-} + 2H^+$$

Radical $R–C_6H_4^\circ$ can subsequently react either with OH° giving a phenolic compound or with a H° radical generated by reaction:

$$H^+ + e^- \rightarrow H^\circ$$

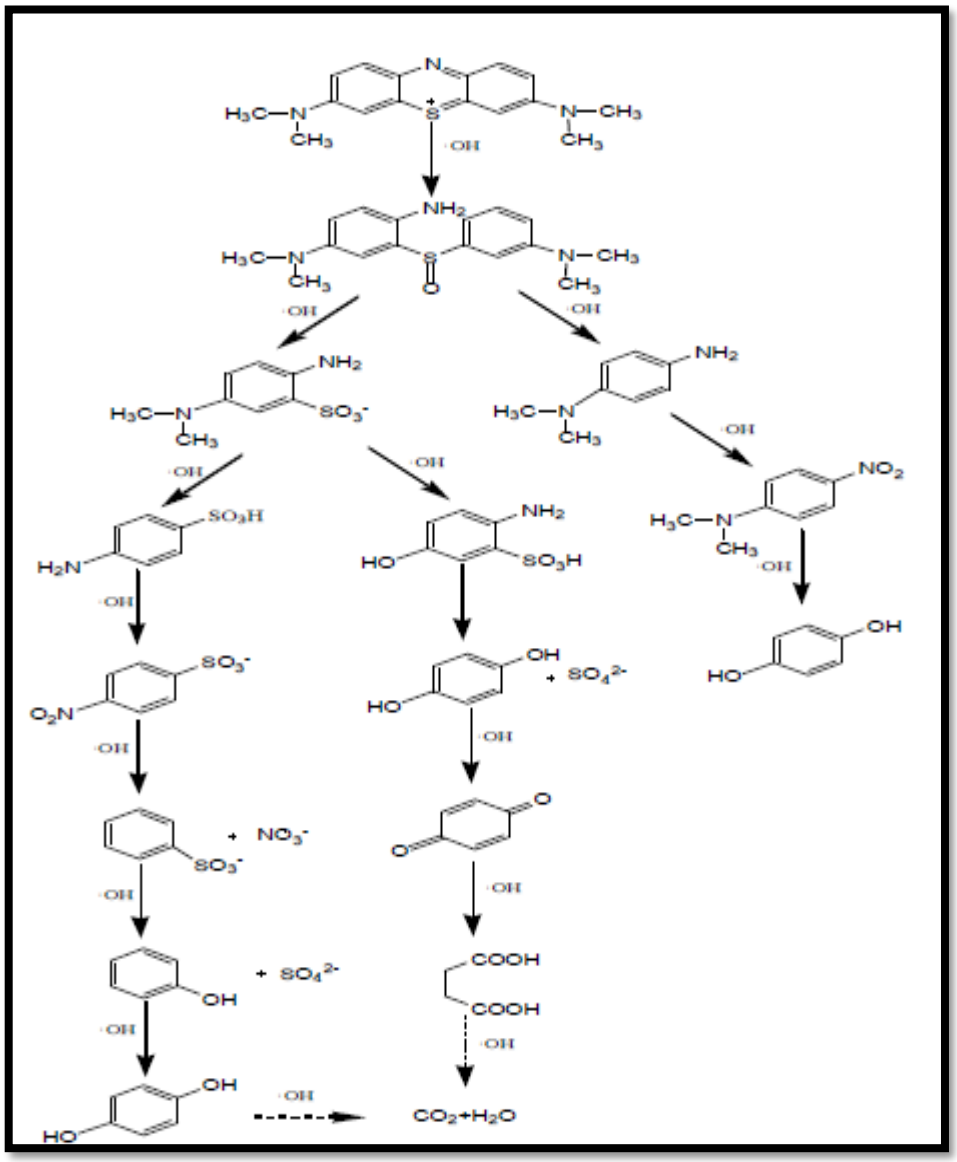

schema. 1 The degradation pathways of methylene blue reacting with Photocatalytic oxidation[1].

Concerning the mineralization of the three nitrogen-containing groups in MB molecule, two cases have to be examined. First, the central imino-group undergoes a N=C double bond cleavage induced by the cleavage of the double bond of the –S+= group in para position in the central aromatic ring. The saturation of the two amino bonds is obtained by H° radicals mentioned above, yielding a substituted aniline. As previously observed, the amino group can be substituted by an OH° radical forming the corresponding phenol and releasing a $NH_2{}^{\circ}$ radical which generates ammonia and ammonium ions, estimated to be primary products as mentioned above.

$$R - C_6H_4 - NH_2 + OH^{\circ}$$
$$\rightarrow \; R - C_6H_4 - OH + NH_2{}^{\circ}$$
$$NH_2{}^{\circ} + H^{\circ} \rightarrow NH_3$$
$$NH_3 + H^{+} \rightarrow NH_4{}^{+}$$

The other two symmetrical dimethyl-phenyl-amino groups undergo a progressive degrading oxidation of one methyl group by an attack by OH° radical producing an alcohol, then an aldehyde, which is spontaneously oxidized into acid, which decarboxylates into CO_2 by photo-Kolbe reaction.

$$R - C_6H_4 - N(CH_3)_2 + OH^{\circ} \rightarrow R - C_6H_4 - N(CH_3) - CH_2^{\circ} + H_2O$$

$$R - C_6H_4 - N(CH_3) - CH_2^{\circ} + OH^{\circ} \rightarrow R - C_6H_4 - N(CH_3) - CH_2OH$$

$$R - C_6H_4 - N(CH_3) - CH_2OH + OH^{\circ} \rightarrow R - C_6H_4 - N(CH_3) - CH^{\circ} - OH + H_2O$$

$$R - C_6H_4 - N(CH_3) - CH^{\circ} - OH + OH^{\circ} \rightarrow R - C_6H_4 - N(CH_3) - CH(OH)_2 \rightarrow R - C_6H_4 - N(CH_3) - CHO + H_2O$$

$$R - C_6H_4 - N(CH_3) - CHO + OH^{\circ} \rightarrow R - C_6H_4 - N(CH_3) - C^{\circ} = O + H_2O$$

$$R - C_6H_4 - N(CH_3) - C^{\circ} = O + OH^{\circ} \rightarrow R - C_6H_4 - N(CH_3) - COOH$$

$$R - C_6H_4 - N(CH_3) - COOH + h^{+} \rightarrow R - C_6H_4 - N^{\circ} - CH_3 + H^{+}$$

Subsequently, the phenyl-methyl-amine radical is degraded, probably by successive attacks by OH° radicals. The aromatic ring will undergo hydroxylations producing phenolic metabolites whose degradation has already been studied, hydroxyhydroquinone being the last aromatic compound detected before the ring opening. The amino group can form ammonium ions as developed above, which are slowly oxidized into nitrate or can be directly oxidized into hydroxylamine leading also to nitrate [1].

Reference

[1] Houas, Ammar, et al. "Photocatalytic degradation pathway of methylene blue in water." Applied Catalysis B: Environmental 31.2 (2001): 145-157.

Abstract

In this work, firstly structural, optical, and morphological properties of Cobalt doped alpha phase iron oxide (hematite: Co-α-Fe_2O_3) thin films has been carried out. Secondly, Co-α-Fe_2O_3 and their applications in the area of wastewater treatment and antibacterial were tested. 0.25-1.5 and 2-20wt. % Co-α-Fe_2O_3 thin films have been deposited on 500°C heated glass via spray pyrolysis with moving nozzle (SPMN). For all 0.25-1.5wt. % Co-α-Fe_2O_3 thin films XRD analysis exhibit the presence of diffraction peaks corresponding to (*012*), (*104*), and (*110*), planes of α-Fe_2O_3 phase. The average grain size changes with doping concentration, it reaches **38.81**nm for 1.5 wt. % Co doping. FTIR study confirms the existence of Fe-O bonds of α-Fe_2O_3, with enhanced hydroxyl radical OH on the surface of Fe_2O_3. Such hydroxyl radical OH is a good result for Photocatalytic application. Photocatalytic activities of 0.25-1.5wt. % Co-α-Fe_2O_3 samples were studied based on the degradation of methylene blue (MB). This activity increases with cobalt doping concentration, and it is better under sunlight irradiation. For antibacterial test, the doping concentration was varied from 2 to 20wt. %. Analyzing XRD pattern indicated the presence of diffraction peaks corresponding to plans (*012*), (*104*), (110), (*113*), (*024*), (*116*), (214), and (300) which signified the hematite phase formation. As a result of doping, two added peaks were appeared and much well with (*200*) and (*311*) planes, of Cobalt oxides CoO and Co_3O_4, respectively. The peak positions correspond to hematite marked a fixed slight shift to lower 2θ values. Crystalline size increases in the beginning of doping then decreases with doping concentration. SEM images demonstrate that the clusters of grain size are homogeneous with some agglomerating sites. The average grain sizes clusters are: 166, 200, 227, and 225 nm for 2, 5, 10, and 20wt. %, respectively. The synthesized cobalt doped hematite nanoparticles exhibit an antibacterial activity against E. coli, Listeria innocua, Pseudo mona saeruginosa and Salmonella enteric beyond 5wt. % Co/Fe doping.

Key words: α-Fe_2O_3; thin films; doping; Photocatalytic activity; antibacterial test.

ملخص

في بداية هذا العمل، تم تحديد الخصائص التركيبية والضوئية والمورفولوجية للشرائح الرقيقة للطور الفا لأكسيد الحديد (الهيماتيت) المطعم بالكوبالت: Co-α-Fe_2O_3، ومن ثم اختبار العينات المطعمة في مجال معالجة المياه الملوثة وكمضادات للبكتيريا. تم ترسيب شرائح رقيقة من أكسيد الحديد المطعم بالكوبالت بالنسب الوزنية (0.25-1.5٪) و(2-20٪) على شرائح زجاجية عبر تقنية الرش بالانحلال الحراري بفوهة متحركة (SPMN) تحت درجة حرارة 500 درجة مئوية. يُظهر تحليل طيف الاشعة السينية -بالنسبة لجميع الشرائح المطعمة بالنسب 0.25-1.5٪-وجود قمم حيود موافقة للمستويات البلورية (*012*) ، (*104*) ، (*110*) ، مما يؤكد تبلور أكسيد الحديد طور ألفا α-Fe_2O_3. يتغير متوسط الحجم الحبيبي مع تركيز نسب التطعيم، ويقدر بـ: **38.81** نانومتر من أجل الشرائح المطعمة بنسبة 1.5٪. تؤكد دراسة مطيافية الاشعة تحت الحمراء وجود الروابط Fe-O للمركب α- Fe_2O_3 ، كما أن التطعيم يعزز وجود مركبات الهيدروكسيل على سطح الشرائح والتي تعد نتيجة جيدة من أجل نشاطية التحفيز الضوئي. تمت دراسة فعالية التحفيز الضوئي للعينات بناءً على تحلل أزرق الميثيلين، حيث أظهرت النتائج أن النشاطية تزداد مع تركيز نسبة التطعيم، ويكون أفضل تحت إشعاع أشعة الشمس. بالنسبة لاختبار أكسيد الحديد كمضاد للبكتيريا، تم تطعيم العينات بالنسب الوزنية: 2 - 20٪. أشار تحليل طيف الاشعة السينية إلى وجود قمم حيود مقابلة للمستويات (*012*) و (*104*) و (*110*) و (*113*) و (*024*) و (*116*) و (*214*) و (*300*) والتي تشير إلى تكون طور الهيماتيت، كما ظهرت قمتان تابعتان للمستويات (*200*) و (*311*) نتيجة للتطعيم، والتي تقابل أكاسيد الكوبالت CoO و Co_3O_4 على التوالي. يزداد الحجم الحبيبي في بداية التطعيم ثم يتناقص تباعا مع زيادة نسبة التطعيم ليصل الى 28.63 نانومتر. توضح صور المسح الالكتروني (SEM) أن حجم الحبيبات متجانسة مع وجود بعض المواقع للتجمعات. متوسط الحجم الحبيبي قدر بـ : 166 ، 200 ، 227 ، 225 نانومتر للنسب الوزنية 2 ، 5 ، 10 ، و 20 ٪ على التوالي. أُظهرت جزيئات الهيماتيت النانوية المطعمة بالكوبالت نشاطًا مضادًا للبكتيريا ضد E. coli و Listeria innocua و Pseudo monasaeruginosa و Salmonella enteric وذلك من أجل نسب تطعيم تتجاوز 5٪ .

الكلمات المفتاحية

α-Fe_2O_3، التطعيم، الاغشية الرقيقة ، نشاطية التحفيز الضوئي ، اختبار مضادات البكتيريا.